

https://dspace.org/

The effect of dark matter in the Epoch of Reionization

Kgoadi, Mpho

2021
https://hdl.handle.net/10539/33161

Downloaded from a DSpace repository. https://dspace.org/

University of the Witwatersrand

Johannesburg



WITS
UNIVERSITY

School of Physics

A dissertation submitted to the Department of Physics, University of the Witwatersrand in fulfilment of the requirements for the degree of Master of Science.

The Effect of Dark Matter in the Epoch of Reionization

Author: Mpho Kgoadi

Date: 2021-09-13

Supervisors: Dr Geoff Beck

Abstract

The problem of dark matter has been of great importance in modern physics since its inception. Many theories have been proposed about the nature of dark matter but perhaps the most studied is the WIMP (Weakly Interacting Massive Particle). This particle has been favoured because it has the properties of dark matter that have been measured experimentally, so far. In this work we present an argument for studying the properties of dark matter in the Epoch of Reionization (EoR) using the redshifted 21 cm background. The 21 cm line of hydrogen provides great potential in studying the Universe at an early stage. This could provide rich information about the thermal and ionization history of the Universe as well as understanding the physics behind the formation of the first stars and galaxies. This will allow us to have a full picture of the global 21 cm background including the effects of WIMPs, if there are any. We also will demonstrate the potential power of HERA and the SKA to probe the high redshift Universe, being able to produce constraints that are quite optimistic against current benchmark models of indirect detection of dark matter.

Declaration

I, MPHO ARTHUR KGOADI , declare that this dissertation and the work presented in it are my own. I Confirm that:

- The research reported in this dissertation, except where otherwise indicated, is my original research
- This work has not been submitted to any other institution or for any other degree.
- Where I have quoted from the work of others, the source is always given. With the exception of such quotations, this research proposal is entirely my own work.
- I have acknowledged all main sources used and have cited these in the reference section.

Signed: 

Date: 2021-09-13

Dedication

For my late grandmother

Acknowledgements

I would like to express my gratitude to my supervisor Dr Geoff Beck, thank you for your continuous support, your patience and understanding. I could not have asked for a better advisor. Special acknowledgement goes to Andrew Sam and the whole staff at the DRU, I would not be here if it weren't for them. I would also like to thank my best friends in the whole wide world for their everlasting support and for being there for me through the highs and the lows. In addition, the financial assistance provided by my supervisor, the NRF Thuthuka grant no. 117969 is hereby acknowledged. Finally, I would like to thank my mother, Zintle, Shimi and the rest of my family for being there for me, and for their patience and love.

Contents

List of Figures iv

1 Introduction 1

2 What is Dark Matter ? 5

2.1 Dark Matter Observations . . . 5

2.1.1 Dynamics of stars and galaxies . . . 5

2.1.2 Gravitational lensing . . . 6

2.1.3 Cosmic Microwave Background . . . 7

2.1.4 Big Bang Nucleosynthesis . . . 8

2.1.5 Structure formation and other sources . . . 8

2.2 Dark Matter Particles . . . 9

2.2.1 Weakly interacting massive particle . . . 10

2.2.2 Dark matter halos . . . 11

2.3 Dark matter detection . . . 13

2.3.1 Direct detection . . . 13

2.3.2 Collider experiments . . . 15

2.3.3 Indirect detection . . . 16

3 Reionization and the 21 cm Hydrogen Line 22

3.1 Epoch of Reionization . . . 23

3.2 21 cm line of hydrogen . . . 25

3.2.1 Determining the spin temperature . . . 28

3.2.1.1 Collisional coupling . . . 29

3.2.1.2 Wouthuysen-Field effect . . . 30
3.2.2 Thermal evolution of the IGM . . . 33
3.2.2.1 Compton Heating . . . 34
3.2.2.2 Lyman-α heating . . . 34
3.2.2.3 X-ray heating . . . 35
3.2.3 Ionization History . . . 36
3.2.4 Global 21 cm signal . . . 37
3.3 Exotic energy injection and dark matter . . . 40
3.3.1 DarkHistory . . . 43
3.3.1.1 Thermal and ionization histories . . . 44
3.3.1.2 Calculating $f_c(z)$ . . . 46
3.3.1.3 Code structure . . . 49
3.4 Observing the 21 cm signal . . . 54
3.4.1 EDGES . . . 54
3.4.2 Can interferometers be used to measure the global 21 cm signal ? . . . 55
3.4.3 SKA and HERA sensitivity . . . 56
4 The Effect of Dark Matter in the Epoch of Reionization 58
4.1 $b\bar{b}$ annihilation channel . . . 59
4.1.1 Global 21 cm signal . . . 59
4.1.2 HERA vs SKA constraints . . . 64
4.2 $\tau^+\tau^-$ annihilation channel . . . 67
4.2.1 Global 21 cm signal . . . 67
4.2.2 HERA vs SKA constraints . . . 71
4.3 Discussion . . . 73
5 Conclusion 75
5.1 Challenges and future work . . . 76

Bibliography **77**

List of Figures

2.1 *left panel*: Image of the Bullet Cluster obtained with gravitational lensing. The X-ray observations of the gas component is shown in pink and the lensing map is shown in blue. The image is taken from [1][2]. *Right Panel:* Mass density contours (green) of the Bullet Cluster and the distribution of baryonic matter. Taken from [3] 7

2.2 A diagram showing annual modulation and directionality 15

2.3 Mediator mass reach of CMS searches for a selection of results targeting electroweak SUSY production. Adapted from [4] 16

2.4 The upper limits of the dSph observations by VERITAS (black solid line) to the DM annihilation cross section into $b\bar{b}$ (**left**) and $\tau^+\tau^-$ (**right**) pairs. See legends for details of the comparison 21

3.1 A schematic diagram of the history of the Universe from the big bang to now. After the big bang the Universe undergoes recombination when the photons get decoupled from the gas and the relic radiation is observed as the CMB at redshift = 1000. After the recombination epoch, the Universe is neutral in the period known as the Dark Ages. About 500 million years after the big bang, the first stars and galaxies form and heat up the Universe and starting the Epoch of Reionization. The Universe is fully ionized around 1 billion years after the big bang, at redshift ≈ 6. This image is credited to NAOJ [5]. 24

3.2 The Wouthuysen-Field effect energy levels. The forbidden transitions are in lines and the dotted lines are the allowed transition but do not contribute to spin flips. Image taken from Ref. [6] 31

3.3 The solid lines represent ionizing photons redshifting into Lyman-n resonance, which then cascade down via multiple possible decay channels. Some decay channels lead to lyman-α emissions contributing to the Lyman-α background. This figure shows decay chains for Lyman-β and Lyman-γ. Dashed lines represents Lyman-n transitions and red-dashed line is the Lyman-α transition. The forbidden transitions are depicted by the dotted lines. Figure taken from [7] 33

3.4 The evolution of the global 21 cm signal. The signal transitions from the early phases of collisional coupling. There is no signal when the gas temperature couples to the background CMB temperature. Fluctuations in the later stages are dominated by various heating mechanisms such as Lyman-α, X-ray, and ionizing radiation background. Relevant redshifts accompany the subsequent radiation backgrounds. Image taken from [7] 38

3.5 Constraints of WIMP annihilation cross-section to reionization for annihilation channels $\chi\chi \to e^+e^-$ (left) and $\chi\chi \to \gamma\gamma$. The hatched regions represents the parameter space ruled out by the optical depth constraints (orange) and the CMB power spectrum constraints measured by Planck (red). The contribution to the free electron fraction x_e is depicted by the colour density plot with the black, dashed contours shown for a contribution to x_e at $z = 6$. image taken from [8]. . 42

3.6 The effects of decaying and annihilation WMD and LDM models on the 21 cm brightness temperature. The solid line shows δT_b for a baseline model without any inclusion of DM effects. The dotted line as well as the long dashed and the short dashed lines represent δT_b with 10 MeV annihilating DM, 25 keV decaying WDM and the 10 MeV decaying WDM, respectively. Image taken from [9] . . . 43

3.7 Flowchart showing the calculation of ionization and thermal histories in *DarkHistory*. 51

3.8 Matter temperature (left) and hydrogen ionization history (right) against redshift solved in the presence of dark matter annihilation into $b\bar{b}$ pairs using *DarkHistory* [10]. The blue line shows the histories with energy injection but no backreaction. The orange line shows dark matter annihilation with backreaction and the black, dashed line shows the baseline without any injection. 53

4.1 The global 21 cm brightness temperature for the baseline (black) case compared to the 100 GeV DM with $\langle\sigma v\rangle = 3 \times 10^{-26}$ cm^3 s^{-1} (orange) 59

4.2 Spin temperature and the matter temperature plot from ref.[11] (Top) and the same plots for our *Darkhistory* case (bottom). The orange plot is the matter temperature, blue is the spin temperature and the black one is the CMB. 60

4.3 Coupling coefficients from ref.[11] compared to the *Darkhistory* ones. The solid orange and blue are the collisional coupling (yc) and the Lyman-α coupling (ya) for ref.[11] respectively and the dashed green and red are the collisional coupling and the Lyman-α coupling for *Darkhistory*. 60

4.4 Brightness temperature for the 100 GeV DM case (blue) sensitivity against the EDGES noise (orange) with 6 hour integration time from ref.[12]. 61

4.5 The global 21 cm brightness temperature for the baseline (black) case compared to the 100 GeV DM with $\langle\sigma v\rangle = 4 \times 10^{-26}$ cm^3 s^{-1} (orange) with HERA noise (blue) 62

4.6 The global 21 cm brightness temperature for the baseline (black) case compared to the 100 GeV DM with $\langle\sigma v\rangle = 9 \times 10^{-27}$ cm^3 s^{-1} (orange) with SKA noise (blue) 63

4.7 Sensitivity constraints on the DM annihilation cross section for DM annihilating into $b\bar{b}$ final state for 1σ c.l with HERA and SKA after 1000 hours of integration time. The blue line represents the HERA constraints and the red line represents the SKA constraints. 64

4.8 Sensitivity constraints on the DM annihilation cross section for DM annihilating into $b\bar{b}$ final state for 2σ c.l with HERA and SKA after 1000 hours of integration time. The blue line represents the HERA constraints and the red line represents the SKA constraints. 64

4.9 Sensitivity constraints on DM annihilation cross section for DM annihilating into $b\bar{b}$ final state for 2σ c.l with HERA and SKA after 1000 hours of integration time compared to the constraint on the DM annihilation cross section for $b\bar{b}$ final states from Ref.[13]. The blue line represents the HERA constraints and the red line represents the SKA constraints. The black dotted lines represents the constraints of DM annihialtion cross section corresponding to the current optical depth measurements of $\Delta\tau = 0.012$. 66

4.10 Sensitivity constraints on DM annihilation cross section for DM annihilating into $b\bar{b}$ final state with HERA and SKA for 1000 hours of integration time compared to the upper limits on the DM annihilation cross section from Ref.[14] (solid black line) and Ref.[15] (solid red line) for $b\bar{b}$ channel at 95% confidence interval. 66

4.11 The computed matter temperature T_m and hydrogen ionization fraction $x_{H_{II}}$ (right) in the presence of 100 GeV WIMP DM particle annihilation into $\tau^+\tau^-$ with cross section of 3 $\times 10^{-26}$ cm^3 s^{-1}. 67

4.12 The global 21 cm brightness temperature for the baseline (black) case compared to the 100 GeV DM with $\langle\sigma v\rangle = 3 \times 10^{-26}$ cm^3 s^{-1} (orange). 68

4.13 The global 21 cm brightness temperature for the baseline (black) case compared to the 100 GeV DM with $\langle\sigma v\rangle = 1 \times 10^{-25}$ cm^3 s^{-1} (orange) with HERA noise (blue). 69

4.14 The global 21 cm brightness temperature for the baseline (black) case compared to the 100 GeV DM with $\langle\sigma v\rangle = 1 \times 10^{-26}$ cm^3 s^{-1} (orange) with SKA noise (blue). 70

4.15 Sensitivity constraints on the DM annihilation cross section for DM annihilating into $\tau^+\tau^-$ final state for 1σ c.l with HERA and SKA after 1000 hours of integration time. The blue line represents the HERA constraints and the red line represents the SKA constraints. 71

4.16 Sensitivity constraints on the DM annihilation cross section for DM annihilating into $\tau^+\tau^-$ final state for 2σ c.l with HERA and SKA after 1000 hours of integration time. The blue line represents the HERA constraints and the red line represents the SKA constraints. 71

4.17 Sensitivity constraints on DM annihilation cross section for DM annihilating into $b\bar{b}$ final state for 2σ c.l with HERA and SKA after 1000 hours of integration time compared to the constraint on the DM annihilation cross section for $\tau^+\tau^-$ final states from Ref.[13]. The blue line represents the HERA constraints and the red line represents the SKA constraints. The black dotted lines represents the constraints on the annihilation cross section corresponding to the current optical depth measurements of $\Delta\tau = 0.012$. 72

4.18 Sensitivity constraints on DM annihilation cross section for DM annihilating into $b\bar{b}$ final state with HERA and SKA for 1000 hours of integration time compared to the upper limits on the DM annihilation cross section from Ref.[14] (solid black line) and Ref.[15] (solid red line) for $b\bar{b}$ channel at 95% confidence interval. 72

Chapter 1

Introduction

The problem of dark matter (DM) has become one of the most exciting endeavours in modern physics. The discovery of dark matter forced phyisicists to examine the current understanding of cosmology. Dark matter forms a fundamental part of the current standard model of the universe known as the Λ-Cold Dark Matter (ΛCDM). This is a model that describes the expanding universe with three major fluid components: a cosmological constant Λ which behaves like a fluid with negative pressure and therefore constitutes a form of so-called "dark energy", the non-relativistic (cold) dark matter and finally baryonic matter. Fritz Zwicky originally hypothesised the idea of dark matter in an attempt to explain the orbital velocity of galaxy clusters [16], since then there has been a hunt for this elusive matter. Although there has been lack of evidence of the nature of dark matter, there are numerous observational experiments indicating its presence. Some of these observations include the fluctuations in the Cosmic Microwave Background [17], structure formation [18], gravitational lensing measurements [19], Big Bang nucleosynthesis [20] and galaxy rotation curves [21]. All these experiments have confirmed that dark matter might be of particle nature, however most of these experiments are indirect and mostly rely on gravitational effects of dark matter. This does not allow us to learn about the exact nature of dark matter and its behaviour, in fact, some scholars have challenged the idea of dark matter and instead hypothesize the idea of Modified Newtonian Dynamics (MOND) to explain the missing mass problem [22].

Since the evidence from observations pointed towards dark matter being of particle nature, it is important to examine which standard model or beyond standard model particles fit the description. Some of these particles include weakly interacting massive particles (WIMPs), axions, sterile neutrino and supersymetric particles (SUSY). WIMPs are thought to be one of the most promising candidates for DM for a number of reasons. The first one being that they arise naturally in a number of theoretically well-motivated models [23, 24, 25, 26]. Secondly, for reasonable ranges of WIMP mass and annihilation cross section the relic abundance of DM can be obtained through mechanisms of thermal freeze-out as well as other production mechanisms [27, 28]. Lastly, WIMPs present a promising target for direct detection experiments of DM because a large fraction of their typical detection rates are within reach for current and future detectors, making them testable. This is why WIMPs are the main focus of this work.

WIMPs interact with standard model fields only via the weak nuclear force, they are non-baryonic and electrically neutral. They are are stable on cosmological timescales, this means that they carry some sort of conserved quantum number [23]. An example includes the Kaluza-Klein particle [29], for which the lightest member of a matter sector is charged under some discrete symmetry. These WIMPs are members of the $SU(2)_L$ multiplets, if there are no other symmetries which might force their masses down, they should naturally acquire masses m_χ within a few orders of magnitude of the $SU(2)_L \times U(1)_Y$ electroweak symmetry-breaking scale (i.e GeV or TeV). Furthermore, this makes WIMPs sufficiently heavy to constitute cold dark matter even if they have been produced thermally in the early Universe. Some popular example of WIMPs include the neutralino, which is the lightest particle from the minimal supersymmetric extension of the standard model (MSSM) [30].

WIMPs can annihilate/decay into Standard Model (SM) particles, particularly in regions of high DM density. Some of these secondary particles include gamma rays, neutrinos, electron-positron pairs and proton-antiproton pairs. Each annihilation process produces a distinctive signature such as gamma-rays from the center of galaxies such as the Milky Way, or neutrinos from the Sun. Notably, WIMPs will produce gamma-rays almost every time through various channels, i.e through pion production for hadronic channels or through inverse Compton and bremsstrahlung for leptonic channels. This could be measured through indirect detection and could potentially provide strong constraints on the dark matter mass and annihilation cross

section or life-time for decays. Recent indirect astrophysical detections have provided strong limits on possible WIMP models through studies of the CMB [17], gamma-ray studies of galaxies with the Fermi-LAT [15, 31] as well as some studies of positron fractions from PAMELA and AMS-02 [32, 33]. The galactic center excess observations from the Fermi-LAT data remain the most intriguing hints of DM detection from the past few years [14]. There have been several claims from the galactic excess center observations that favour a WIMP of mass $\geq$ 30 GeV and cross section of $\langle \sigma v \rangle \sim 3 \times 10^{-26}$. However, there have been competing arguments that explain the galactic center excess without the presence of dark matter [34, 35, 36]. This work will focus on detecting dark matter through radio observation of the 21 cm spectrum from the Epoch of Reionization using future telescopes, namely, the Hydrogen Epoch of Reionization Array (HERA) and the Square Kilometer Array (SKA).

The Epoch of Reionization (EoR) is a period in the evolution of the Universe which occurred between z $\sim$ 6-13, where intergalactic hydrogen changes from being completely neutral to being completely ionized. The EoR represents the moment in cosmic history when structure formation has progressed far enough to impact the global state of the Universe. The measurements of the conditions during EoR promises a wealth of information about structure evolution, as such it could form a bridge between fundamental physics and cosmology and the complex astrophysics associated with galaxy formation [37, 38]. In principle, the EoR can be probed in many different ways. In this work, the focus is on the observations based on the redshifted 21 cm line of neutral hydrogen. The 21 cm line is the hyperfine spin-flip transition of neutral hydrogen caused by the interaction between the electron and proton magnetic moments [7]. This technique provides a promising way to study the high redshift Universe, However, observing the EoR is still a considerable challenge since there is still an issue extracting and identifying cosmological signals from data and interpreting it correctly. The reason is that the detectable signal in the relevant frequency from the EoR is tainted by a number of components - ionospheric distortions, instrument noise and response as well as extragalactic and galactic foreground [39].

We begin with Chapter 2, providing a brief introduction to the problem of DM, including a detailed review of the observational evidence that proves the particle nature of DM, specifically a non-baryonic nature of DM. A description of particle solution of DM is given and an overview of direct and indirect methods of searching for WIMP DM. Chapter 3 details the EoR and the full description of 21 cm physics. This leads to a full global 21 cm cosmology picture which details the complicated astrophysics involved in the analysis. Chapter 3 also contains a brief overview of the influence exotic energy injection and dark matter as well as evidence from previous work. It ends with a section on *DarkHistory*, a code package for calculating the evolution of thermal and ionization histories with DM injection included. Chapter 4 is the results section, where detailed findings of our work has been provided. The section begins with an analysis of temperature and ionization histories for two annihilation channels, $b\bar{b}$ and $\tau\tau$, this provides a framework for the subsequent calculations. The brightness temperature is then plotted for the baseline and dark matter cases to see the effect that dark matter has on the global 21 cm signal. The constraints for DM masses and annihilation cross sections are then derived for HERA and SKA cases. Finally the constraints are compared against previous work. Chapter 5 provides the concluding summary.

Chapter 2

What is Dark Matter ?

This chapter contains an introduction to the problem of dark matter. The particle solutions to the problem are outlined and furthermore, a detailed review of the detection strategies of dark matter is provided, especially focusing on the indirect detection method. Then section 2.1 provides a brief outline of the observational evidence of dark matter, indicating a particle solution to the problem. This is followed by section 2.2, by a detailed discussion of DM particles, with particular emphasis on Weakly Interacting Massive Paricles (WIMPs). This chapter closes with section 2.3 which focuses on detection methods of dark matter, including direct, collider and indirect detection.

2.1 Dark Matter Observations

2.1.1 Dynamics of stars and galaxies

The problem of dark matter began in the early 20th century with astronomer Fritz Zwicky [16]. He was studying the velocity dispersion of galaxies within clusters when he noticed that the outer members of the Coma Cluster were moving faster than anticipated, with some exceeding 2000 km/s. Although the velocity dispersion of the Coma clusters were observed by scientists before him, Zwicky was the first one to use the well studied virial theorem to further investigate this problem. He noticed that the only way to account for the observed orbital velocities of the outer members of the cluster with the virial theorem was to propose that Coma cluster

contained a non-luminous, very large mass component. He would later coin this missing mass the term "dark matter".

The idea of the missing mass in galaxy clusters was met with skepticism up until 1970 when Rubin and Ford [40] studied a similar effect for galaxies. Similar to galaxies in the outskirts of a cluster, stars in the outer regions of galaxies orbit faster than expected. They found that the rotation curves of galaxies are flat rather than dropping off at long distances from the centre of the galaxy. This flat behaviour was another hint that there was missing matter in galaxies that was holding the stars in orbit and the mass distribution spans much larger distances. The work by Rubin et al was enough to convince the scientific community that a large amount of unseen mass is present in the universe and throughout the years there have been numerous observations at all cosmological scales that support the existence of DM.

2.1.2 Gravitational lensing

In Einstein's theory of General Relativity (GR) [41], gravity is not a force but the curvature of space-time as a result of the density distribution of various matter-energy components. GR predicts the deflection of light around massive bodies because light follows a geodesic in space-time. This produces a distorted (weak lensing) [3] or multiple (strong lensing) [42] images of the light source for the observer, This is refered to as gravitational lensing. This phenomenon provides a way to measure the mass and the matter distribution of the foreground object from the angles of deflection since the amount of lensing is sensitive to the strength of the gravitational field generated by the massive object [43]. This method can be used to calculate DM mass in the foreground object by comparing it to the visible mass since the angle of lensing is affected by the total mass distribution, not only the visible mass.

Observations of the well-known Bullet cluster [1, 19], a collision of two galaxy clusters, provides the best evidence of DM using gravitational lensing, shown in the left panel of Figure 2.1. Not only does the lensing map (in blue) exhibit large amounts of DM not evident in the X-ray gas map (in pink), but the distribution of the two components provides crucial insight into the properties of dark matter. The interstellar gas of the two clusters, seen in X-ray, lags behind

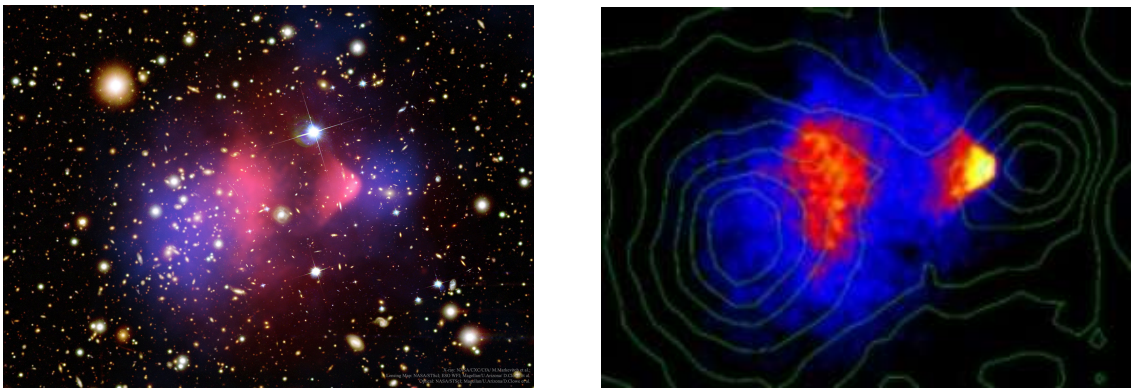


Figure 2.1: *left panel*: Image of the Bullet Cluster obtained with gravitational lensing. The X-ray observations of the gas component is shown in pink and the lensing map is shown in blue. The image is taken from [1][2]. *Right Panel:* Mass density contours (green) of the Bullet Cluster and the distribution of baryonic matter. Taken from [3]

because it interacts electromagnetically. Gravitational lensing observations show that the center of mass of both clusters is in the region near the visible mass, this is seen from the contour map in the right panel Figure 2.1 , indicating that there is a large amount of additional mass in both clusters that is appears undisturbed after the collision, a weakly interacting massive component which is a property of DM.

2.1.3 Cosmic Microwave Background

The Cosmic Microwave Background (CMB) plays a further role in determining the DM abundance in the universe. The CMB is radiation emitted in the early universe during a period called recombination, when the temperature had become low enough for neutral hydrogen to form so that photons could escape. Observations from the Wilkinson Microwave Anisotropy Probe (WMAP) [44] and the Planck telescope [17] show the universe to be anisotropic in the early universe to a level of about 1 in 10^5. There are fluctuations on small scales coming from from the pressure waves in the early universe plasma that were "frozen in" in the CMB. These fluctuations are thought to be originating from the fluctuations of a quantum field responsible for inflation and are relevant since they are the initial gravity wells around which the matter in the universe formed structures we see today. The sizes of the fluctuations give a precise measurement of the amount of DM in the universe. The CMB power spectrum reveal that the first peak indicates that the geometry of the Universe is flat, the remaining peaks implies that the matter component is dominated by DM with ordinary baryonic matter contributing to about

5% while DM is about 26%. The remaining dominant matter-energy contribution comes from *dark energy* with about 69%. to this day, the CMB provides the most precise measurement of the amount of DM in the Universe.

2.1.4 Big Bang Nucleosynthesis

The early universe contained an abundance of light elements produced via the Big Bang Nucleosynthesis (BBN), this is another important evidence for DM. After a few minutes after the Big Bang, when the universe sufficiently cooled to about a temperature of ten billion degrees, neutrons and protons were able to combine to form stable deuterium in the following process: $\mathbf{p} + \mathbf{n} \rightarrow \mathbf{D} + \gamma$. Subsequently, helium and lithium began to form as well [45]. Elements heavier than helium had to wait much longer, for star formation to take place in order to appear. BBN theory predicts that roughly 25% of the baryonic mass in the universe is made of Helium-4, 0.01% deuterium and even smaller quantity of Li-7; about 10^{-10} [46]. These predictions are in agreement with data as long as baryonic matter can only account for about 5% of the total energy density of the universe, or $\Omega_b \sim 0.05$ [47].

2.1.5 Structure formation and other sources

More evidence for dark matter is derived from a number of sources. These include the cosmic evolution and the growth of structure; as discussed in subsection 2.1.3 the early universe produced overdense regions, they were dominated by dark matter. The overdensities acted as gravitational seeds that would ultimately be responsible for the formation of stars and galaxies. Without DM in the early universe, structures would start to grow at a much later stage [48] but this is in disagreement with observation [49, 50]. Large-scale 'N-body' simulations support this claim and demonstrates that large scale structures observed today could have only formed in the presence of a large amount of cold and non-dissipative dark matter. Measurements from the type 1A supernaovae also favours the argument for dark matter. This is the process of standard candles with known luminosity. The geometry of the universe, which is dependent on the energy content of the universe can be determined by fitting observed luminosities as a function of redshift. This analysis shows that the matter content (dark and baryonic matter) of the universe is $\Omega_m \lesssim 0.3$ [51]. The luminosity distance-redshift relation in combination with

the BBN arguments gives a strong indication that the matter content in the universe is mostly non-baryonic.

With observational evidence from primordial BBN and the CMB anisotropy data to the evolution of structures and the dynamics of galaxies, it has become clear that the universe contains a large amount of non-baryonic matter component. All these sources agree that this matter component is weakly interacting and makes up a large amount of all the matter content in the universe. It is most likely an exotic particle not found in the standard model [52].

2.2 Dark Matter Particles

Various models have been proposed in search of a solution to the missing mass problem. The issue is that the information from the observations in section 2.1 gave no clue to the exact nature of DM but it does suggest that it should be a new and exotic particle. This idea grew successively since the 1970s when the main alternatives were slowly ruled out as the experiments became more sensitive and powerful. These alternatives featured astrophysical objects known as the Massive Astrophysical Compact Halo Objects (MACHOs). A MACHO is any astrophysical body that emits little to no light and occupied the outer halos of galaxies. These objects were thought to be white and brown dwarfs, black holes and planets. MACHOs can be detected via gravitational lensing as they pass in front of stars or galaxies. There have been several measurements of MACHOs, particularly Ref.[53] claimed to have found microlensing to predict the existence of MACHOS, enough to make up 20% of the DM in the galaxy. However, searches after that have ruled out the possibility of MACHOs making up a considerable amount of DM. since then, MACHOs were quickly ruled out since they were baryonic matter, violating the non-baryonic requirement.

The requirements for a good dark matter candidate include a particle that is massive, it should carry no electric and colour charge, it should interact only weakly with ordinary matter and be long-lived (stable) or at least have a lifetime that exceeds the age of the universe. a few standard model particles meet this requirement, so the distinguishing factor is the velocity of

the particles. Good DM candidates should be non-relativistic or "cold" according to the density fluctuations in the CMB that are responsible for structure formation. Particles with velocities that are ultra-relativistic or "hot" during the time of decoupling due to the large mean free path were unable to form structures. There are still popular "hot" dark matter candidates [54, 55], which emerges from the Pecci-Quinn solution to the strong CP problem that are still considered viable candidates. However, despite all of this, one candidate still seem to fit the available evidence most satisfactorily; the Weakly Interacting Massive Particle (WIMP), which is the main focus of this work.

2.2.1 Weakly interacting massive particle

WIMPs are strongly favoured as candidates for dark matter because they meet most of the requirements from section 2.1 and for the the fact that they arise naturally in supersymmetry (SUSY) and Kaluza-Klein (KK) theories. They can interact with other nucleons and with themselves. The scattering cross section is used to measure the probability of WIMPs interacting with other nucleons and the annihilation cross section is used to calculate the rate at which they self-annihilate. WIMPs are produced in the early hot universe, when the DM particles were in thermal equilibrium with standard model particles in a hot plasma, with DM particles and anti-particles annihilations balancing each other out. The rate at which the DM particles self-annihilate decreases as the universe expands because the number density of the particles also decreases. This is given by the Boltzmann equation with number density n for a dark matter particle [23]:

$$\frac{dn}{dt} + 3Hn = -\langle\sigma v\rangle(n^2 - {n_{eq}}^2) \tag{2.1}$$

where n_{eq} and n are the equilibrium and actual number densities of the species, $H \equiv \dot{a}/a$ is the hubble expansion with a being the scale factor and $\langle\sigma v\rangle$ is the velocity-averaged annihilation cross-section. The DM particles stop annihilating once $H \sim \langle\sigma v\rangle n$. Equation 2.1 can be solved

numerically to obtain relic density of different DM particle species. [23, 56] gives the relic density for WIMPs as

$$\Omega_\chi h^2 = \frac{m_\chi n_\chi}{\rho_c} \approx \frac{3 \times 10^{-27} \mathrm{cm}^3 \mathrm{s}^{-1}}{\langle \sigma v \rangle} \tag{2.2}$$

where h is the reduced hubble constant and ρ_c is the critical density. Equation 2.2 shows that the relic density has an inverse relation to its annihilation cross-section. This means that specific DM particles freeze out later if the annihilation cross-section is longer and this exhibits a lower relic density. The current accepted limit for the annihilation cross-section is $\langle \sigma v \rangle = 3 \times 10^{-26} \mathrm{cm}^3 \mathrm{s}^{-1}$.

If there is an assumption that a new DM particle that interacts weakly exists, then its annihilation cross-section can be estimated by $\langle \sigma v \rangle \approx \alpha^2 / E_{weak}^2$ where $\alpha = 10^{-2}$ and E_{weak} is the electroweak scale given by $E_{weak} \approx 100$ GeV and this results to $\langle \sigma v \rangle \approx 10^{-8} \mathrm{GeV} = 10^{-25} \mathrm{cm}^3 \mathrm{s}^{-1}$. By assuming that DM is a stable weakly-interacting particle, the relic density is found to be within one order of magnitude from the calculated value. This is known as the "WIMP miracle" and gives a strong possibility that WIMPs might be the solution to the DM problem.

2.2.2 Dark matter halos

WIMPs are massive, this can lead to formation of dense viralized clumps of DM bound together by gravity, known as "halos". These provide gravitational potential wells to which structures such as galaxies form. Detailed large-scale N-body simulations of structure formation can provide valuable information about the density profiles of DM which can be combined with benchmark models of particle physics to give a meaningful way to indirectly detect WIMPs. This is still a work in progress since even after years of Monte Carlo simulations and a number of different experiments, the scientific community has yet to reach a consensus of which is the most accurate DM density profile. Stellar velocity measurements and more advanced simulations of cold DM and baryonic physics continue to change the current understanding of halo profiles. Studying the properties of DM halos is important since the highly dense halo regions in galaxies or galaxy clusters have an increased chance of WIMP pair annihilation which increase a chance

of its detectablity. These DM halos are the missing mass that was mentioned in section 2.1.

The shapes for density profiles can be inferred from observations of the path stars take in the gravitational potential well of the halo and from N-body simulations. The most favoured profile is a cusped ($\rho \approx r^{-1}$) profile but some mini-galactic sized objects are described better with a cored (central density is constant) profile. The most commonly used profile is the Navarro-Frenk-White (NFW) [57] profile which provides a good fit for a wide range of halo masses and it is given by the equation:

$$\rho_{NFW}(r) = \frac{\rho_0}{(r/r_s)(1 + r/r_s)^2} \tag{2.3}$$

where r is the distance from the center of the halo, r_s is the scale radius and ρ_0 is the scale density which can be written as a ratio of the scale virial radius R_{vir} to r_s and is defined as the concentration parameter c or $c_{vir} = \frac{R_{vir}}{r_s}$. The virial mass can be shown to be:

$$M = 4\pi\rho_0 r_s^3 \left[\ln(1 + c) - \frac{c}{1 + c} \right] \tag{2.4}$$

[58, 59, 60] have employed this method on various situations including modelling the dwarf Spheroidal (dSph) satellite of the Milky Way which shows that the fit is less concentrated than expected, means that there needs to be some profiles that can explain small sized dwarf galaxies.

Another profile that is a good fit as the NFW, and might be even better at galactic-size is the Einasto profile [61]. It is given by the following equation:

$$\rho_{einasto}(r) = \rho_0 e^{-2n[(r/r_s)^{1/n} - 1]} \tag{2.5}$$

where $n = 1/\alpha$ is a parameter that describes the degree of curvature of the distribution. The Einasto profile has a logarithmic slope that vary with radius and can be written as:

$$\frac{dln\rho}{dlnr} = -2\left(\frac{r}{r_{-2}}\right)^{1/n} \tag{2.6}$$

where r_{-2} is the radius from which the slope is -2. The Einasto and the NFW profiles are both "cusped" profiles because of the steep slope around r=0. a more commonly used "cored" profile is called the Burkert profile [62]

$$\rho_{Burkert} = \frac{\rho_0}{(1 + r/r_s)(1 + r/rs)^2} \tag{2.7}$$

As mentioned above, the Burkert profile best fits rotation curves of smaller dwarf sized galaxies. Detection of stellar population of dSph provide mass estimates at different radii that are in agreement with the cored profiles and are incompatible with cusped profiles [63, 64].

2.3 Dark matter detection

This section will cover how WIMPs can be detected using three different methods. The first one being direct detection, this involves searching for the recoil of WIMPs scattering on nuclei using very sensitive detectors. This is followed by collider searches which is an attempt to create WIMPs directly by smashing standard model particles together in accelerators like the Large Hadron Collider (LHC). Lastly, indirect detection where one searches for annihilation products or decays of WIMPs in astrophysical environments of high dark matter density like halos. Indirect detection is the main focus of this work thus it will be covered in detail in this chapter.

2.3.1 Direct detection

Goodman and Witten [65] came up with an idea of detecting WIMPs directly by looking for nuclear recoils in target materials of large volumes on Earth. WIMPs interact with standard

model particles weakly, in most cases they will not interact with electrons but elastically scatter off the nucleus. When this happens, they will transfer some of their energy to the particles they are interacting with, this momentum transfer will lead to a recoil which could be detected by the experiment. The detection processes include ionisation of target atoms, scintillation, and phonon production generated in crystals. A WIMP with mass 10 GeV to 1 TeV that has undergone elastic scattering would produce nuclear recoil energy of 1 to 100 keV [66]. This energy is really small, the measurements need to be very sensitive and precise, the advantage of direct detection is its ability to differentiate between galactic signal and Earth based background signals. The expected rate of WIMPs scattering off a nucleus is given by the differential recoil spectrum

$$\frac{dR}{dE}(E,t) = \frac{\rho_0}{m_\chi m_n} \int v f(\mathbf{v},t) \frac{d\sigma}{dE}(E,v) d^3v \tag{2.8}$$

where E is the nuclear recoil energy, ρ_0 is the local dark matter density, m_χ is the mass of the WIMP, the target nucleon mass is given by m_n. $\frac{d\sigma}{dE}$ is the differential cross-section and the function $f(\mathbf{v},t)$ is the normalized WIMP velocity distribution. The velocity is defined in the reference frame of the detector.

The minimum velocity needed for a WIMP to induce a recoil is

$$v_{min} = \sqrt{\frac{E m_n}{2} \frac{(m_n + m_\chi)^2}{(m_n m_\chi)}} = \sqrt{\frac{E m_n}{2} \frac{1}{\mu^2}} \tag{2.9}$$

where μ is the reduced mass of the system. WIMPs that have a velocity exceeding that of the escape velocity will not be bound by the Milky Way's gravitational potential and will not be detected. Directionality and annual modulation play a key role in direct detection. The Sun revolves around the center of the galaxy, this motion around the DM halo creates a DM wind. The motion of the Earth around the Sun adds up as a factor to create the annual modulation of the WIMP wind velocity which leads to the recoil rate as mentioned in Equation 2.8 as seen in the figure below.

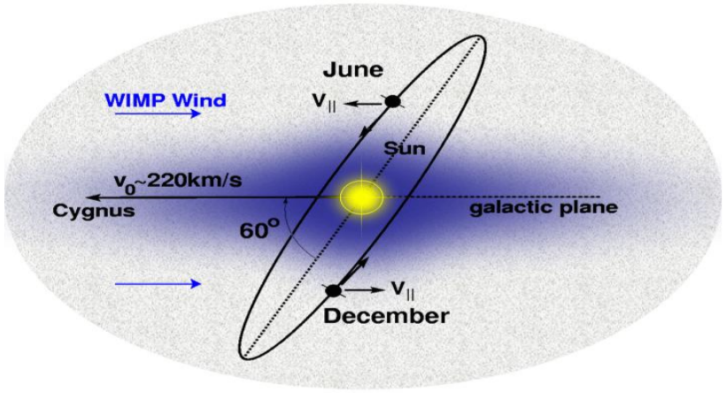


Figure 2.2: A diagram showing annual modulation and directionality

This shows that the velocity distribution of the WIMP should peak in June and be at its minimum in December when Earth is moving in the opposite direction of the galactic disk.

There are numerous direct detection experiments that are currently ongoing in search of WIMPs. These include the Dark Matter Large Sodium Iodide Bulk for RAre processes (DAMA/LIBRA) [67], the Coherent Germanium Neutrino Technology (CoGeNT) [68] and the XENON1T which has the strongest limits placed on the spin-independent cross-section at about $4.1 \times 10^{-47}\text{cm}^2$ for a WIMP mass of 50 GeV at 90% confidence level [69].

2.3.2 Collider experiments

Collider searches is the use of particle accelerators to smash protons with a center of mass energy of 13 TeV together in hope of finding signals of dark matter particles in the collision. One possible way of detecting WIMP signal would be to find the missing transverse energy (missing E_T), which refers to the undetected energy expected in collisions due to the conservation of energy and momentum. WIMPs can go through the detector without being detected because they interact weakly with standard model particles, this is the missing energy. This method of searching for missing energy in collisions has been interpreted in roughly three classes of models at the Large Hadron Collider (LHC) - complete models, such as the MSSM; effective field theories, where new high mass particles are not included but their effect is encoded in low-energy constants; and simplified models, which are a compromise of the former two, not complete particle physics models but also not effective models as they include new particles [45, 46].

ATLAS and CMS have been participating in experiments looking for SUSY particles. Searches have produced strong constraints on SUSY particles with neutralino masses of about 2 TeV [70]. Direct production of SUSY particles that are weakly coupled have a smaller production rate and the constraints on them are weak. Third generation squarks are constrained to be a few hundred GeV for neutralinos with a similar mass as seen in Figure 2.3.

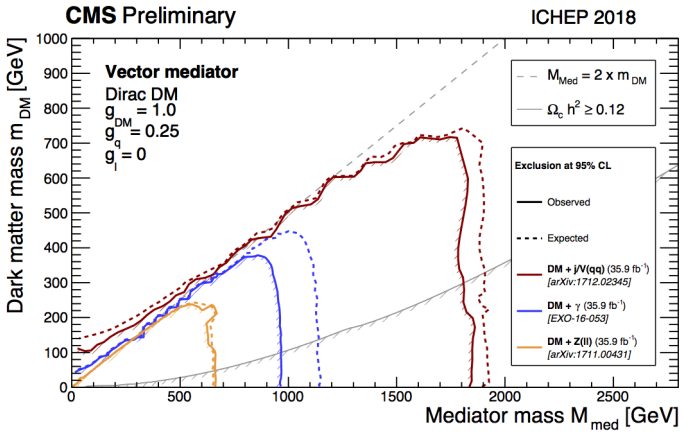


Figure 2.3: Mediator mass reach of CMS searches for a selection of results targeting electroweak SUSY production. Adapted from [4]

Colliders will help most in identifying and characterising the theory to which the dark matter particles belong whilst direct and indirect searches will provide information about how stable the particle are and their cosmological abundance.

2.3.3 Indirect detection

Indirect detection refers to observation of dark matter annihilation/decay products in a given astrophysical environment such as the Sun [71] or galactic dark matter halos [15] mentioned in subsection 2.2.1 . These annihilation products come in the form of photons, neutrinos, electron positron pairs, proton antiproton pairs and even antideuterium. Various annihilation channels could produce specific signatures, an example includes detection of high energy neutrinos coming from the Sun or gamma-rays coming from the centers of galaxies. It is important to note that nearly all annihilation channels will produce gamma-rays at some point, for hadronic channels it could be through pion production and for leptonic channels it could be via inverse Compton or bremsstrahlung [72]. This method is very complicated because backgrounds from ordinary astrophysical processes make it difficult to estimate where the sources originate from. Dwarf spheroidal galaxies become a good option since they are mostly dominated by DM which

leads to very low background but they also have low predicted fluxes which could be concerning [73].

Notable observations of cosmic rays and gamma-rays fluxes have provided possible signals of annihilation or decay products of dark matter particles. Some of the observations include WMAP and Fermi satellites revealing the excess of gamma-rays and microwaves in the galaxy [74]. The 511-keV line emission detected by the SPI spectrometer using the INTEGRAL satellite on the bulge of the galaxy [75]. PAMELA and AMS-02 observed a rise in the positron fraction above 10 GeV spectral line [33, 32]. Perhaps the toughest constraints for WIMPs come from the observations of dwarf spheroidal galaxies for masses just below 100 GeV provided by the Fermi-LAT and MAGIC experiments [76]. It is worth noting that given the limited statistics of the fermi line or the astrophysical backgrounds or large systems of the 511-keV emmision and positron fraction, a dark matter interpretation from these signals is not clear.

A *boost factor* is required to explain the excess flux predicted for the most generic and conservative models such as the steepening of the halo profile. In fact, a number of important theoretical studies have suggested a need for a boost to associate the above mentioned signals with dark matter e.g since the fluxes from DM annihilations depend on the square of the density, some processes could change the inner profile of the galactic center, so strong boosts near the center of galaxies are possible. Another boost could result if the annihilation cross section today is larger than it was at decoupling, especially if there is a strong dependence on relative velocity between DM particles. A p-wave velocity dependent cross section of $\sigma v \approx bv^2$ could explain the 511 keV emission since it is well known that DM particles that were initially moving at relativistic speeds at decoupling are now moving at slower speeds and that could result in the relic density for a light MeV DM particle that annihilates into non-relativistic electron-positron pairs with $\sigma v \approx 10^{-5}$ [77, 78]. Similarly, a significant boost is required to explain the positron excess. AMS-02 data suggests that the thermal cross section falls short by two orders of magnitude but this can be reconciled if the annihilation follows $\sigma v \approx 1/v$. This is the *Sommerfeld enhancement* and it comes from the exchange of new light particles and it explains the rising positron fraction at high energies [79, 80, 81].

In order to determine the photon flux coming from DM annihilation or decay, one needs to take into account both contribution from particle physics for the relevant cross-section or decay rates and for astrophysics for dark matter density distribution. This flux resulting from annihilation of a WIMP with mass m_χ to gamma-rays or neutrinos is defined as

$$\frac{d\phi}{dE} = PJ \tag{2.10}$$

where P is the particle physics term and J is the astrophysical term. Let the volume in which WIMPs annihilate be $dV = l^2 dl d\Omega$ where l is the line-of-sight distance and $d\Omega$ is solid angle. We can define the thermally averaged cross-section for the annihilation channel i as $\langle \sigma_i v \rangle$ such that the annihilation rate per particle is written as

$$\sum_i^{\text{channels}} \frac{\rho(r)}{M_\chi} \langle \sigma_i v \rangle \tag{2.11}$$

The sum with the index i is taken over all annihilation channels. We can get the total annihilation in a volume dV by multiplying the annihilation rate per particle with the number of particle pairs in dV since there are two particles that participate in every reaction thus

$$\left(\sum_i^{\text{channels}} \frac{\rho(r)}{M_\chi} \langle \sigma_i v \rangle \right) \left(\frac{\rho(r) dV}{2M_\chi} \right) \tag{2.12}$$

.

let $dN_{\gamma,i}/dE$ be the differential annihilation spectrum, the differential flux coming from a volume element $dV = l^2 dl d\Omega$ at a distance l is then

$$\frac{1}{4\pi l^2} \sum_i^{\text{channels}} \frac{dN_{\gamma,i}}{dE} \frac{\rho(r)^2 \langle \sigma_i v \rangle}{2M_\chi^2} l^2 dl d\Omega \tag{2.13}$$

Taking an integral over the whole volume in the cone we get the differential photon flux from annihilating dark matter that is expected to be measurable:

$$\frac{d\phi}{dE} = \int_{\Delta\Omega} d\Omega \int_{l.o.s} dl \sum_{i}^{\text{channels}} \frac{dN_{\gamma,i}}{dE} \frac{\rho(r)^2 \langle \sigma_i v \rangle}{8\pi M_\chi^2} \tag{2.14}$$

$$= \frac{1}{8\pi} \sum_{i}^{\text{channels}} \frac{dN_{\gamma,i}}{dE} \frac{\langle \sigma_i v \rangle}{M_\chi^2} \times \int_{\Delta\Omega} d\Omega \int_{l.o.s} dl \rho(r)^2 \tag{2.15}$$

from this we can see that the particle physics term is

$$P = \sum_{i}^{\text{channels}} \frac{dN_{\gamma,i}}{dE} \frac{\langle \sigma_i v \rangle}{M_\chi^2} \tag{2.16}$$

and the astrophysical term is

$$J = \int_{\Delta\Omega} d\Omega \int_{l.o.s} dl \rho(r)^2 \tag{2.17}$$

In a similar fashion, the flux from decaying dark matter can be derived as

$$\frac{d\phi}{dE} = \frac{1}{4\pi} \sum_{i}^{\text{channels}} \frac{\Gamma_i}{M_\chi} \frac{dN_{\gamma,i}}{dE} \times \int_{\Delta\Omega} d\Omega \int_{l.o.s} dl \rho(r) \tag{2.18}$$

where Γ_i is the decay width of channel i. For dark matter decay, the signal is proportional to the sight integral of the density, unlike annihilation which is proportional to the square of the density, this gives slightly less sensitivity to the detailed halo model. To get the full picture, it is necessary to understand the full *phase-space density* which includes not only the density profile but the velocity distribution in order to derive a self-consistent halo model that includes dynamical measurements such as the stellar velocities and rotation curves. the phase-space density of DM is defined as:

$$dN = f(\mathbf{x}, \mathbf{v}, t) d^3\mathbf{x} d^3\mathbf{v} \tag{2.19}$$

where dN is the number of particles within a phase-space element $d^3\mathbf{x}d^3\mathbf{v}$ in coordinates (**x,v**).

Assuming that the phase-space is separable such that it can be written as $f(\mathbf{x},\mathbf{v}) = n(\mathbf{x})f_v(\mathbf{v})$, and DM is self-annihilating, then the rate of annihilation of DM in a halo is

$$\Gamma = \langle \sigma_A v_{rel} \rangle \int d^3\mathbf{x} n^2\mathbf{x} \tag{2.20}$$

the velocity-averaged annihilation cross section $\langle \sigma_A v_{rel} \rangle$ is taken over relative velocities of particles interating with each other. We assume a velocity independent s-wave annihilation cross section, however, in some cases where the phase-space density is not separable and have a p-wave cross sections like the simulated halos defined in subsection 2.2.1 then it is not possible to simplify the above expression and one must calculate the collision term in the Boltzmann equation [82].

The annihilation to charged particles situation is slightly different because the diffusion and energy loss also affect the observed signal [83, 84]. One needs to convolve the source function for annihilation with the Green's function for cosmic-ray propagation including diffusion and energy loss mechanisms such as inverse-Compton and synchrotron radiation for electrons. Both of these mechanisms have a dependency on energy and it can combined to give

$$\frac{dE}{dt} = -bE^2 \tag{2.21}$$

If we include the diffusion constant κ, the transport equation can be solved to give the Green's function which will gives the intensity of positrons and electrons at position x, time t and energy E due to an impulse at position t and energy E_0

$$G(x,t,E) = (4\pi\kappa t)^{-3/2}(1-bEt)^2 exp\left(-\frac{x^2}{4\kappa t} - t/\tau\right)\delta\left(E_0 - \frac{E}{-1-bEt}\right) \tag{2.22}$$

where τ is the lifetime of the WIMP and δ is the Dirac-delta function. This equation shows that for a emitting source at a distance x, that admits a power-law spectrum, there will be a

sharp steep in the spectrum beyond $E \geq \frac{4\kappa}{br^2}$. If we combine this with the source function we can get the annihilation rate

$$Q(E,x) = 4\pi \frac{dN_{e^+}}{dEd^3xdt} = \sum_i^{channels} \frac{\langle \sigma_i v \rangle}{M_\chi^2} \frac{dN_{e^+,i}}{dE} \times \rho(r)^2 \tag{2.23}$$

and we can get the observed, nearly isotropic, electron spectrum by integrating over time and over the distribution of DM:

$$\frac{dN_{e^+}}{dE_{e^+}} = \int dt \int d^3x \int dE' G(x,t,E,E') Q(E',x) \tag{2.24}$$

This can be solved numerically with codes such as the GALPROP [25].

Some current limits from indirect detection are included in Figure 2.4 taken from [85]. This shows the limits obtained by the VERITAS of DM annihilation cross-section into $b\bar{b}$ and $\tau^+\tau^-$ pairs compared with other gamma-ray instruments of the dSph observations. The 95% confidence level upper limits to the channel $b\bar{b}$ is shown on the left of the figure and the $\tau^+\tau^-$ limit on the right. For $b\bar{b}$ the constraints reach $< \sigma v > \approx 10^{-23} cm^3 s^{-1}$ at $m_\chi \approx 1$ TeV and the $\tau^+\tau^-$ limits are $< \sigma v > \approx 3 \times 10^{-24} cm^3 s^{-1}$ at $m_\chi \approx 300$ GeV

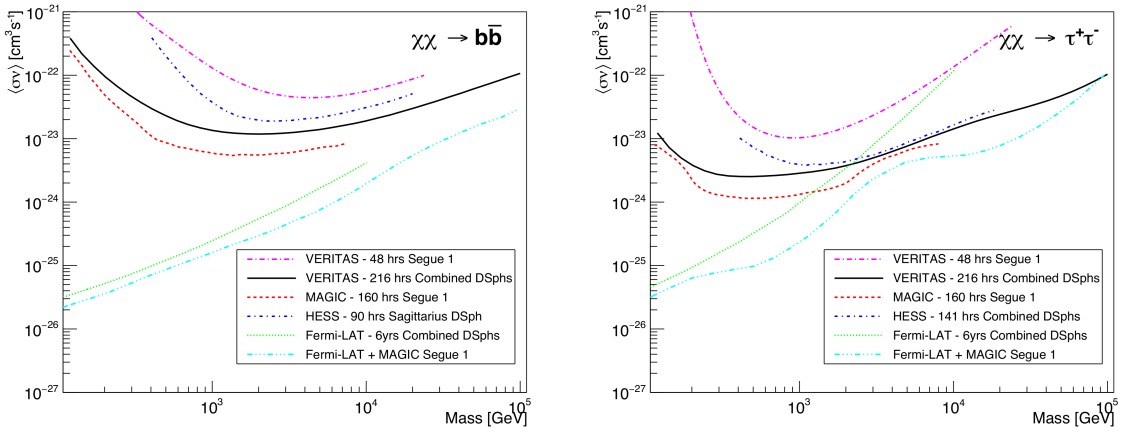


Figure 2.4: The upper limits of the dSph observations by VERITAS (black solid line) to the DM annihilation cross section into $b\bar{b}$ (**left**) and $\tau^+\tau^-$ (**right**) pairs. See legends for details of the comparison

Chapter 3

Reionization and the 21 cm Hydrogen Line

This chapter will review the Epoch of Reionization and how it can be detected with the method of the redshifted 21-cm line of hydrogen. This chapter will briefly explain the physics behind the 21-cm hydrogen hyperfine line and its detectability. An overview of how dark matter can alter the reionization history will be provided in section 3.3 as well as how it affects the 21-cm spectrum. Then subsection 3.3.1 will discuss a code package called *DarkHistory* by Ref.[10] which will be used as a method of acquiring results in the following chapter. We then proceed to give a brief outline of how we calculate the sensitivity of the Square Kilometer array (SKA) and Hydrogen Epoch Of Reonization Array (HERA).

3.1 Epoch of Reionization

The Epoch of Reionization (EoR) is one of the most exciting problems in modern physical cosmology. The possibility of observing the events that lead to EoR promises rich information about the complicated astrophysics that is responsible for galaxy formation and it could shape our current understanding of fundamental physics. Scientists have been able to use the CMB as a means to explain how complex and non-linear structures formed from the observed initial perturbations that are inhomogeneous in 1 part in 100 000. This paradigm has been very successful explaining the early Universe, however, the events after that: the *Cosmic Dark Ages* and the *Cosmic Dawn* have been untested by observation. These periods will provide a better understanding of the phase transition of a neutral Universe to a completely ionized one.

About 380 000 years after the big bang, the Universe sufficiently cooled for protons and electrons to combine to form neutral hydrogen, this is the epoch of recombination. During this time, photons decoupled from the gas and this relic radiation can be observed today in the microwave spectrum and it is what we refer to as the CMB. This is followed by the cosmic dark ages where the universe was filled with neutral hydrogen and had no luminous sources. It is during this time that larger non-linear structures begin to form and collapse to form sheets, filaments and halos. These eventually form stars and galaxies which then emit photons ending the dark ages, bringing about the cosmic dawn at a redshift of about $z \approx 30$. The first stars heated the surrounding intergalactic medium (IGM) forming near-infrared and non-ionizing ultra-violet (UV) and X-ray backgrounds which raised the temperature of the gas in the Universe and started the reionization process where the ionization radiation escapes the galaxies and ionizes their surrounding IGM. This is called the Epoch of Reionization [7, 37, 39]. A brief history of the Universe is shown in the Figure 3.1. The main contributors of the reionization process are considered to be the young, star-forming galaxies but some theories suggests that dark matter annihilation/decay may have played a role in this [86, 87, 88], we try to investigate this claim in this research.

Observing the EoR has been a considerable challenge, to this day, the majority of EoR related observations provide weak and model dependent constraints on reionization. Some observations cannot agree as to when the reionization process was completed. This includes the absorption spectra of high redshift quasars suggesting that the universe was neutral by redshift $z \approx 6$ [89, 90]

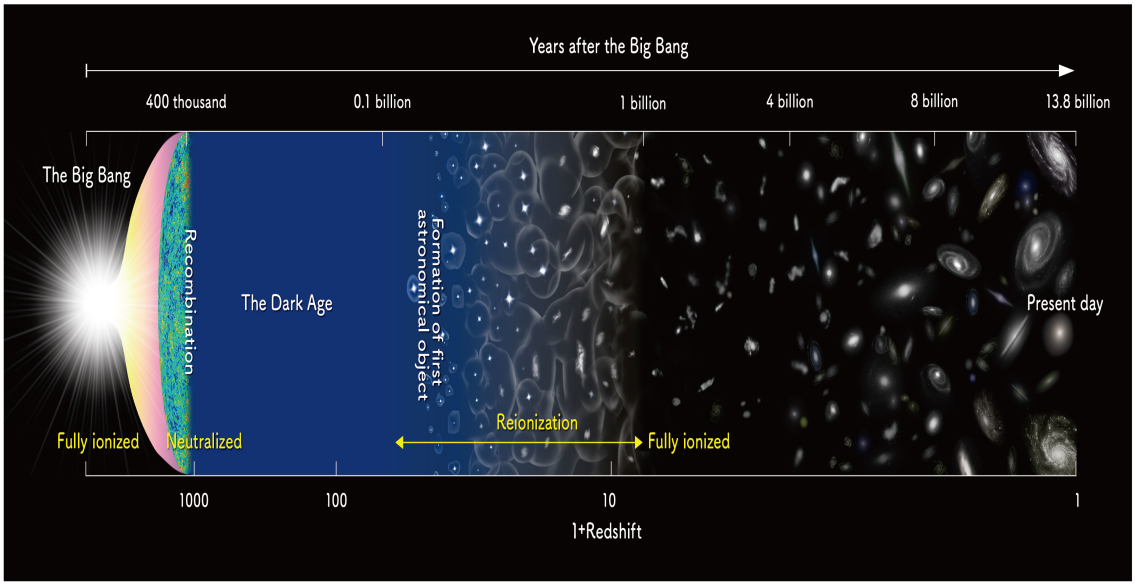


Figure 3.1: A schematic diagram of the history of the Universe from the big bang to now. After the big bang the Universe undergoes recombination when the photons get decoupled from the gas and the relic radiation is observed as the CMB at redshift = 1000. After the recombination epoch, the Universe is neutral in the period known as the Dark Ages. About 500 million years after the big bang, the first stars and galaxies form and heat up the Universe and starting the Epoch of Reionization. The Universe is fully ionized around 1 billion years after the big bang, at redshift ≈ 6. This image is credited to NAOJ [5].

whereas the CMB radiation obtained by the Planck satellite suggesting that reionization ended at z $\approx 8.8 \pm 1.1$ [17], It is important to note that this is model dependent. This means that most of the information that is available comes from theory and simulations, however, there are now up and running telescopes that try to rectify this issue. Out of the many probes and techniques the most promising one and the focus of this dissertation is the measurement of the redshifted 21 cm line of hydrogen. There are a number of efforts dedicated to detecting the EoR by mapping the 21 cm line with radio instruments such as the Precision Array to Probe the Epoch of Reionization (PAPER) [91], Low Frequency Array (LOFAR) [92], Murchison Widefield Array (MWA) [93] as well as the Hydrogen Epoch of Reionization Array (HERA) [94] and the Square Kilometer Array (SKA) [37]. The last two instruments will be used in this work to constrain some results. Since the universe is mostly filled with hydrogen, this technique will prove to be useful and the aim is to measure the 21 cm intensity from the intergalactic neutral hydrogen with the CMB being a background source at redshifts of about $z \leqslant 12$ but the SKA will take this a step further by going beyond reionization and making detailed intensity maps to a redshift of z = 30 while HERA will also be able to probe EoR to z $\sim$ 18. The results of

this could provide great insight about the evolution of the EoR, the sources that ionized the gas as well as the sizes of the ionized regions.

3.2 21 cm line of hydrogen

The 21 cm line is a hyperfine transition line of neutral hydrogen between two states caused by the interaction of the magnetic moments of the electron and the proton. The lower singlet state arises when the spins are antiparallel and the excited triplet state when the spins are parallel. The difference in energy between the two states is $\Delta E_{10} = 5.9 \times 10^{-6}$ eV, this is a frequency of 1420 MHz, corresponding to a wavelength of $\lambda = 21.1061$ cm [95]. The 21 cm line is forbidden by selection rules of quantum mechanics, meaning that the probability for a spontaneous $1 \rightarrow 0$ transition is given by the value $A_{10} = 2.85 \times 10^{-15}\text{sec}^{-1}$, known as the Einstein's coefficient. This very low spontaneous emission rate corresponds to a half-life of

$$\tau_{1/2} = A_{10}^{-1} = 3.5 \times 10^{14}\text{s} \approx 11\text{Myrs} \tag{3.1}$$

Despite this, the 21 cm transition line still remains one of the most important astrophysical probes because of three main reasons. The first being that neutral hydrogen is ubiquitous in the early universe, some fraction of it will be in the triplet state so the spontaneous emissions are not rare. Secondly, The optical depth of HI gas is very small at relevant 21 cm frequencies, so transmission rates are larger. Lastly, the population of the triplet states are established by the efficiency of collisions and Lyman-α pumping.

The brightness temperature T_b is the fundamental observable for telescopes in detecting the redshifted 21 cm line. The brightness temperature can be associated with the temperature of a blackbody emitting at an observed Intensity at appropriate frequencies derived from the Rayleigh-Jeans limit such that:

$$I_\nu = B_\nu(T_b) = \frac{2\nu^2 k_b T_b}{c^2} \tag{3.2}$$

where k_b is the Boltzmann's constant and c is the speed of light. The radiative transfer equation normally written as $I_\nu = \frac{dI}{d\nu}$ can be used to derive the brightness temperature. For thermally emitting material at a temperature T, the transfer equation can be written in terms of the optical depth for absorption as,

$$\frac{dI_\nu}{d\tau_\nu} = -I_\nu + B_\nu(T) \tag{3.3}$$

τ_ν is the optical depth through a cloud at a specific frequency and B_ν is the Planck function. Using the relations of Intensity and brightness temperature in Equation 3.2, brightness temperature can be expressed as

$$\frac{dT_b}{d\tau_\nu} = -T_b + T_{CMB} \tag{3.4}$$

T_{CMB} represents the background CMB temperature. The differential equation above can be solved to find the temperature of the radiation at frequency ν [38]

$$T_b(\nu) = T_s(1 - e^{-\tau_\nu}) + T_{CMB}(\nu)e^{-\tau_\nu} \tag{3.5}$$

This equation provides information about specific conditions that influence the brightness temperature signal. The transmission probability is given by the background radiation factor exp($-\tau_\nu$) and the emission probability is given by the factor 1-exp($-\tau_\nu$). The brightness temperature depends on two factors, namely the spin temperature and the optical depth. The spin temperature T_s is the ratio between the occupation of the two hyperfine levels expressed as,

$$\frac{n_1}{n_0} = \frac{g_1}{g_0} e^{-T_\star/T_s} \tag{3.6}$$

where n_0 and n_1 are the number densities of electrons in the singlet and triplet states respectively. The statistical weights of the energy levels are given by $g_1 = 3$ and $g_0 = 1$. $T_\star = 0.0681$K is the temperature associated with the 21 cm wavelength.

The optical depth can be derived using the fact that the 21 cm line is an ideal transition that can be described by the Einstein's coefficients and their relations. The Einstein Coeffiecient B_{01} corresponding to absorption and the emission coefficient B_{10} can be produced by the 21 cm radiation incident on an atom. Their probabilities are given by Ref [96],

$$I_\nu B_{01} = \frac{g_1}{g_0} B_{10} I_\nu \tag{3.7}$$

and

$$I_\nu B_{10} = A_{10} \frac{\lambda^2 I_\nu}{2h\nu_{10}} \tag{3.8}$$

The absorption cross section of the 21 cm line is

$$\sigma_\nu = \sigma_{01}\phi(\nu) = \frac{3c^2 A_{10}}{8\pi\nu^2}\phi(_\nu) \tag{3.9}$$

$\phi(\nu)$ is known as the line profile and is normalised such that $\int d\nu\phi(\nu) = 1$. The optical depth of a cloud of hydrogen is then

$$\tau_\nu = \int ds(1 - e^{-E_{10}/k_B T_s})\sigma_0\phi(\nu)n_0 \tag{3.10}$$

Using the fact that the optical depth is small at required frequencies, the observed 21 cm brightness temperature is

$$\delta T_b = \frac{T_s - T_{CMB}}{1+z}(1 - e^{-\tau_\nu}) \tag{3.11}$$

$$\approx \frac{T_s - T_{CMB}}{1+z}\tau \tag{3.12}$$

$$\approx 27 x_{HI}(1+\delta_b)\left(\frac{\Omega_b h^2}{0.023}\right)\left(\frac{0.15}{\Omega_m h^2}\frac{1+z}{10}\right)^{1/2}\left(\frac{T_s - T_{CMB}}{T_s}\right)\left[\frac{\partial_r v_r}{(1+z)H(z)}\right] mK, \tag{3.13}$$

x_{HI} is the neutral fraction of hydrogen, δ_b is the fractional overdensity in baryons and $\partial_r v_r$ is the velocity gradient along the line of sight [39]. This result shows that in order for a brightness temperature signal to be observed, the spin temperature needs to deviate from the CMB. The physics that governs the spin temperature is thus important in understanding the signal. The ionization history of hydrogen also plays a vital role, which makes this the ideal probe for reionization.

3.2.1 Determining the spin temperature

The following mechanisms are responsible for determining the spin temperature: a) Absorption of background radiation and stimulated emission; b) collisions with other particle species such as HI atoms, protons and free electrons; and c) lyman-α scattering that involve intermediate excited states. The equation that describes the spin temperature is given by [7]

$$T_s^{-1} = \frac{T_\gamma^{-1} + x_c T_k^{-1} + x_\alpha T_c^{-1}}{1 + x_c + x_\alpha} \tag{3.14}$$

x_c is the collisional coupling coefficient and x_α is the Lyman-α coefficient. T_γ is the background temperature, in this case the CMB and T_k is the gas temperature. T_c is the colour temperature of the Lyman-α radiation. The coupling coefficients determine whether collisions or Lyman-α photons affect the signal and provides information about how strongly coupled is the spin temperature to the gas temperature. The full evolution of the spin temperature can be established once the five parameters in Equation 3.14 can be calculated. The underlying physics leading to the contributing factors is explored below.

3.2.1.1 Collisional coupling

Collisions between particles induce a spin-flips in a hydrogen atom and can affect the spin temperature in the early Universe when the particle densities were high. There are three collision channels available: collisions between H-H atoms [97], H-e [98] and H-p [99]. The collisional coupling for a species i can be written as

$$x_c^i \equiv \frac{C_{10}}{A_{10}}\frac{T_\star}{T_\gamma} = \frac{n_i \kappa_{10}^i}{A_{10}}\frac{T_\star}{T_\gamma} \tag{3.15}$$

where κ_{10}^i is the specific rate coefficient for spin deexcitation by collisions with species i and C_{10} is the collisional excitation rate. The total coupling coefficient can be written to include the three channels,

$$x_c = x_c^{HH} + x_c^{eH} + x_c^{pH} \tag{3.16}$$

$$x_c = \frac{T_\star}{A_{10}}\left(n_H \kappa_{10}^{HH} + n_e \kappa_{10}^{eH} + n_p \kappa_{10}^{pH}\right) \tag{3.17}$$

where κ_{10}^{HH} represents the scattering rate for hydrogen atoms, κ_{10}^{eH} is for electrons and hydrogen and lastly κ_{10}^{HH} is between protons and hydrogen atoms. The collision rates (with units of $\mathrm{cm}^3 s^{-1}$) are obtained through quantum mechanical calculations for relevant particle interaction and the values are tabulated in Ref. [97, 98, 99, 100]. The general form of the scattering rate for the three collision channels is

$$\kappa_{10}^i = \sqrt{\frac{8 k_B T_k}{\pi M_i}}\,\bar{\sigma}_i \tag{3.18}$$

where the average spin transition cross section is

$$\bar{\sigma}_i = \frac{1}{(k_B T_k)^2}\int dE \bar{\sigma}_i(E) E e^{\frac{E}{k_B T_k}}$$

This can be interpreted as the average collision velocity for each channel. Collisional coupling is the most prominent coupling during the cosmic dark ages and the details of the process become important. The calculations above, for example, assumes that the collisional cross-sections do not depend on velocity since the velocity dependency leads to a non-thermal distribution for the hyperfine occupation [7]. This can cause a suppression of the 21 cm signal by at least 5 %, which is important in the context of making use of the 21 cm signal for precision cosmology [98].

3.2.1.2 Wouthuysen-Field effect

The Wouthuysen-Field effect becomes more important during the formation of the first stars in the Cosmic Dawn. It describes the coupling of the spin temperature to the Lyman-α photons i.e UV photons. This process is illustrated in Figure 3.2 and it shows the hyperfine structure of the hydrogen 1S and 2P levels. If hydrogen is initially in the singlet state then the absorption of Lyman-α photons will excite the atom to the 2P state and follows the dipole selection rules which only allows for transitions when $\Delta F = 0 \pm 1$ and no F $= 0 \rightarrow 0$ which makes the other levels inaccessible. The only accessible states are the $2_1P_{1/2}$ or the $2_1P_{3/2}$ and from there the atom can deexcite down to the $1_1S_{1/2}$ state. The rest of the transitions are illustrated in Figure 3.2.

The coupling can be written as

$$x_\alpha = \frac{4P_\alpha}{21A_{10}}\frac{T_\star}{T_\gamma} \tag{3.19}$$

P_α is known as the scattering rate of Lyman-α photons. The relation $P_{01} = 4P_\alpha/27$ was used [101]. The total rate per atom at which Lyman-α photons scatter is given by

$$P_\alpha = 4\pi\chi_\alpha \int d\nu J_\nu(\nu)\phi_\alpha(\nu) \tag{3.20}$$

where $\sigma_\nu = \chi_\alpha \phi_\alpha(\nu)$ is the local absorption cross section, the oscillation strength of the Lyman-α transition is given by $\chi_\alpha \equiv \pi e^2 f_\alpha / m_e c$, ϕ_α is the Lyman-α absorption profile and $\mathrm{J}_\nu(\nu)$ is the angle-averaged specific intensity of the background radiation field by number.

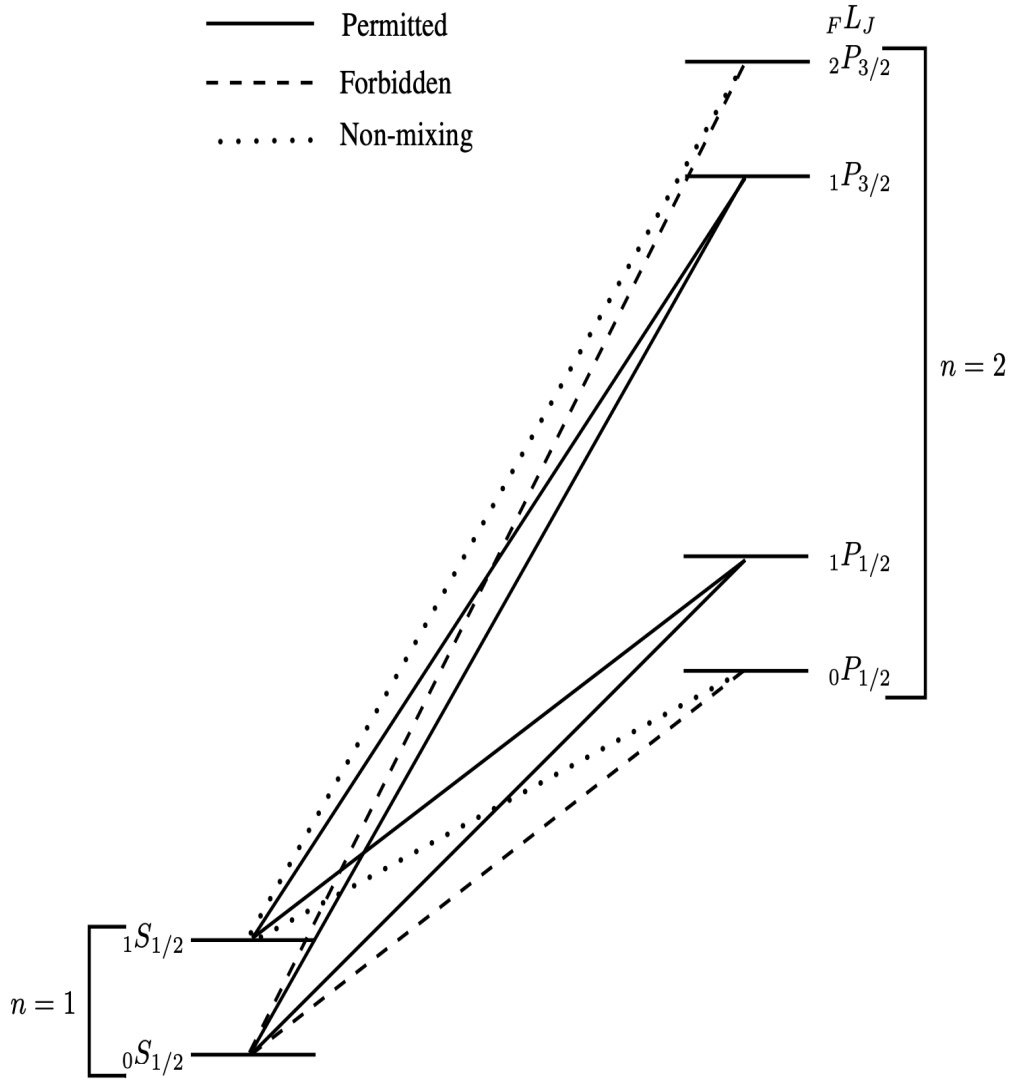


Figure 3.2: The Wouthuysen-Field effect energy levels. The forbidden transitions are in lines and the dotted lines are the allowed transition but do not contribute to spin flips. Image taken from Ref. [6]

Combining Equation 3.19 and Equation 3.20, an expression for the coupling can be described as

$$x_\alpha = \frac{16\pi^2 T_\star e^2 f_\alpha}{27 A_{10} T_\gamma m_e c} S_\alpha J_\alpha = S_\alpha \frac{J_\alpha}{J_\alpha^C} \tag{3.21}$$

The suppression factor which describes the photon distribution close to the Lyman-α resonance is,

$$S_\alpha = \int dx \phi_\alpha(x) J(x) \tag{3.22}$$

The specific flux J_α can be evaluated at the Lyman-α frequency. Equation 3.21 can be used to calculate the critical flux needed to produce $x_\alpha = S_\alpha$ where $J_\alpha^C = 1.165 \times 10^{10}[(1+z)/20] cm^{-2} s^{-1} Hz^{-1} sr^{-1}$. The critical flux in terms of the number of Lyman-α photons per hydrogen atom can be expressed as $J_\alpha^C / n_H = 0.0767[(1+z)/20]^{-2}$.

The physics described above describing the Wouthuysen-Field effect couples the spin temperature to the colour temperature of the UV radiation field. T_c is a measure of the shape of the radiation field as a function of frequency and is defined by

$$\frac{h}{k_B T_c} = -\frac{d log n_\nu}{d\nu} \tag{3.23}$$

where $n_\nu = c^2 J_\nu / 2\nu^2$ is the photon occupation number. The shape of the Lyman-α profile will be similar to that of a black body at the gas temperature T_k for an optically thick medium since the Lyman-α photons scatter at a higher rate. Therefore $T_c \approx T_k$ for frequencies of interest. This means that in astrophysics, the primary interest lies with photons that redshift into the Lyman-α resonance from frequencies below the Lyman-β resonance. Figure 3.3 shows the Lyman-α photons that can be produced by atomic cascades from photons redshifting into higher Lyman-n series resonances. The probability of converting a Lyman-n into a Lyman-α photon is given by the atomic rate coefficients in the table found in [102]. About 30% of conversion is typical for large n which changes the contribution of photons that are injected to the Lyman-α line to the Wouthuysen-Field coupling.

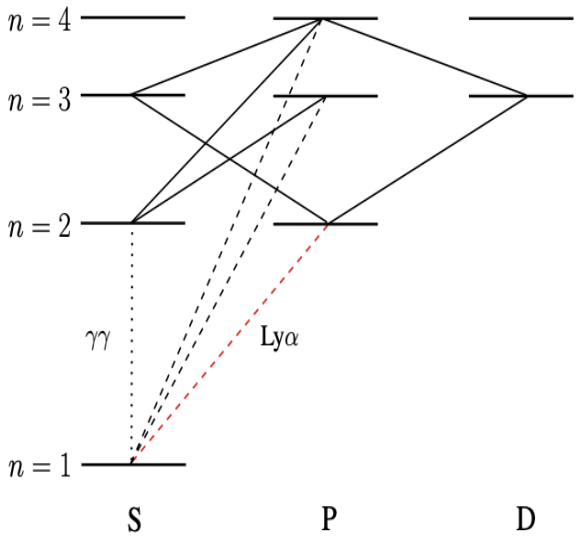


Figure 3.3: The solid lines represent ionizing photons redshifting into Lyman-n resonance, which then cascade down via multiple possible decay channels. Some decay channels lead to lyman-α emissions contributing to the Lyman-α background. This figure shows decay chains for Lyman-β and Lyman-γ. Dashed lines represents Lyman-n transitions and red-dashed line is the Lyman-α transition. The forbidden transitions are depicted by the dotted lines. Figure taken from [7]

3.2.2 Thermal evolution of the IGM

The next important ingredient of the spin temperature is the thermal evolution of the IGM parametrized by the gas temperature T_k and free electron fraction x_e. The evolution of the gas temperature T_k can be modelled as

$$\frac{dT_k}{dt} = \frac{2T_k}{3n}\frac{dn}{dt} + \frac{2}{3k_B}\sum_i \frac{\epsilon_i}{n} \tag{3.24}$$

Where n is the number density of neutral gas particles, k_B is the Boltzmann's constant. The first term is a cooling term due to the Hubble expansion, the second term describes the heating of the IGM determined by the factor ϵ_i which is the heating rate per unit volume taken over processes i. To solve the above equation, specific heating mechanisms that play a role at different times in the history of the Universe need to be dissected.

3.2.2.1 Compton Heating

Before star formation, the dominant mechanism is the heating of the gas from Compton scattering between the CMB photons and the residual free electron fraction. The energy of the electrons increases during the scattering process which can transfer the excess energy from the CMB to other particles in the gas. The heating rate per particle due to Compton scattering is calculated in [103, 104]

$$\frac{2}{3}\frac{\epsilon_{compton}}{k_B n} = \frac{x_e}{1+f_{He}+x_e}\left(\frac{T_\gamma - T_k}{T_\gamma}\right)\frac{\mu_\gamma}{\bar{\mu_\gamma}}(1+z)^4 \tag{3.25}$$

where μ_γ is the energy density of the CMB, f_{He} is the helium fraction (by number) and we define the Compton cooling time as

$$t_\gamma \equiv \frac{3m_e c}{8\sigma_T \mu_\gamma} \tag{3.26}$$

where $\sigma_T = 6.65 \times 10^{-25} cm^2$ is the Thomson cross section. At high redshifts when astrophysical sources are not yet prevalent, Compton heating couples the gas temperature to the CMB such that the IGM cools at the same rate as the CMB i.e $T_k \propto (1+z)$. At a later stage, the IGM decouples from the gas and cools adiabatically with the expansion thereafter.

3.2.2.2 Lyman-α heating

Lyman-α plays a secondary heating mechanism after X-ray heating which is thought to be the largest contributing mechanism. Lyman-α requires large fluxes of Lyman-α photons so it is most important at later stages of the evolution and may be insufficient to the gas to the CMB temperature alone. X-ray heating leads to the suppression of the Lyman-α background. The energy loss in the radiation background therefore goes into heating the IGM. The heating rate can be found in [105]

$$\frac{2}{3}\frac{\epsilon_\alpha}{k_B n_H H(z) T_k} \approx \frac{0.8}{T_k^{3/4}}\frac{x_\alpha}{S_\alpha}\left(\frac{10}{1+z}\right) \tag{3.27}$$

3.2.2.3 X-ray heating

X-ray heating of the gas is the most important mechanism contributing to the gas temperature. As star formation takes place, high intensity X-ray sources such as population III stars, black holes and quasars fill the Universe [38, 106, 39]. X-ray photons emitted by these sources are able to heat the IGM far from the source since they have a long mean free path, this ensures homogeneous heating of the gas. The comoving mean free path of an X-ray photon is given by [98]

$$\lambda_x = 4.9\bar{x}_{H_I}^{1/3}\left(\frac{1+x}{15}\right)^{-2}\left(\frac{E}{300eV}\right)^{3} Mpc \tag{3.28}$$

The Universe will be optically thick for photons below the energy

$$E = 2\left[\frac{(1+z)}{15}\right]^{1/2}\bar{x}^{1/3} keV \tag{3.29}$$

The E^{-3} dependence means that soft X-rays which fluctuate at small scales dominates the heating while there is an existing uniform harder X-rays also contributing to the heating. The relationship between star formation rate, SFR, and X-ray luminosity, Lx, can be extrapolated at high redshift as [98]

$$L_x = 3.4\times10^{40} f_x\left(\frac{SFR}{1M_{\odot}yr^{-1}}\right) \tag{3.30}$$

where f_x is some renormalization factor. Understanding the high redshift X-ray sources is crucial in determining f_x. The high energy X-ray photons ionize HI and HeI, this creates the energetic free electrons which heat the IGM through three main channels. the first being collisional ionization which produce secondary electrons, the second is collisional excitation of hydrogen and helium, this produces photons capable of ionizing HI and Lyman-α background. Lastly, Coulomb collisions with free electrons. The fraction of the X-ray energies going into

heating, ionization and excitation are determined by their relative cross sections and are related by

$$f_{x,h} \sim \frac{1 + 2\bar{x}_i}{3} \tag{3.31}$$

$$f_{x,ion} \sim f_{x,coll} \sim \frac{1 - \bar{x}_i}{3} \tag{3.32}$$

The X-ray energy input to the gas can be determined by assuming SFR is proportional to the rate of the gas collapse into virialized halos [98],

$$\frac{2}{3}\frac{\epsilon_x}{kBnH(z)} = 10^3 K f_x \left(\frac{f_\star}{0.1}\frac{f_{x,h}}{0.2}\frac{df_{coll}/dz}{0.01}\frac{1+z}{10}\right) \tag{3.33}$$

where $f_\star$ is the star formation efficiency. This equation only takes star formation rate into account, the other sources such as quasars need to be studied in greater detail in order to increase the accuracy of X-ray heating. There is also heating closer to the halo from gravitational collapse and a contribution from the UV photoionization, however this is subdominant in the IGM.

3.2.3 Ionization History

The ionization history is the next important step towards a full understanding of the spin temperature and the brightness temperature. The mechanisms mentioned above as well as the collisional coupling mostly depend on the ionization state of the the Universe. The production rate of ionizing photons is assumed to be coupled to the star formation rate, with an average ionizing efficiency defined as [107]

$$\bar{x}_i = \frac{\zeta f_{coll}}{1 + \bar{n}_{rec}} \tag{3.34}$$

where $\bar{n}_{rec}$ is the average number of recombinations per ionized hydrogen atom and ζ is the ionization efficiency given by

$$\zeta = A_{He} f_{\star} f_{esc} N_{ion} \tag{3.35}$$

where N_{ion} is the number of ionizing photons produced per stellar baryons, A_{He} is a correction factor for the presence of Helium and f_{esc} is the fraction of ionizing photons that escape the halos. At the late stages of ionization, recombination rates become important, ionized bubbles create dense clumps that act as sinks of ionizing photons which slows down the expansion of the bubble. this term that opposes ionization is defined to be

$$\left(\frac{d\bar{x}_i}{dt}_{rec}\right) = -\alpha C(z, \bar{x}_i)\bar{x}_i(z) n_e(z) \tag{3.36}$$

with α denoting the recombination coefficient and $C \equiv \langle n_e^2 \rangle / \langle n_e \rangle^2$ being the clumping factor and n_e is the mean electron density in ionized regions. The overall neutral fraction is given by

$$\frac{d\bar{x}_i}{dt} = \zeta(z)\frac{df_{coll}}{dt} - \alpha C(z, \bar{x}_i)\bar{x}_i(z) n_e(z) \tag{3.37}$$

The full analysis of the above equation depends on parameters which are poorly constrained by observation and are detailed in Ref. [7, 98]

3.2.4 Global 21 cm signal

We have described the physics that determines the evolution of the spin temperature, gas temperature, ionization history and the overall brightness temperature in the previous section, now we are ready to provide a general prediction of the global evolution of the 21 cm signal. The 21 cm signal can be summarized in Figure 3.4 below. The important regimes are described below.

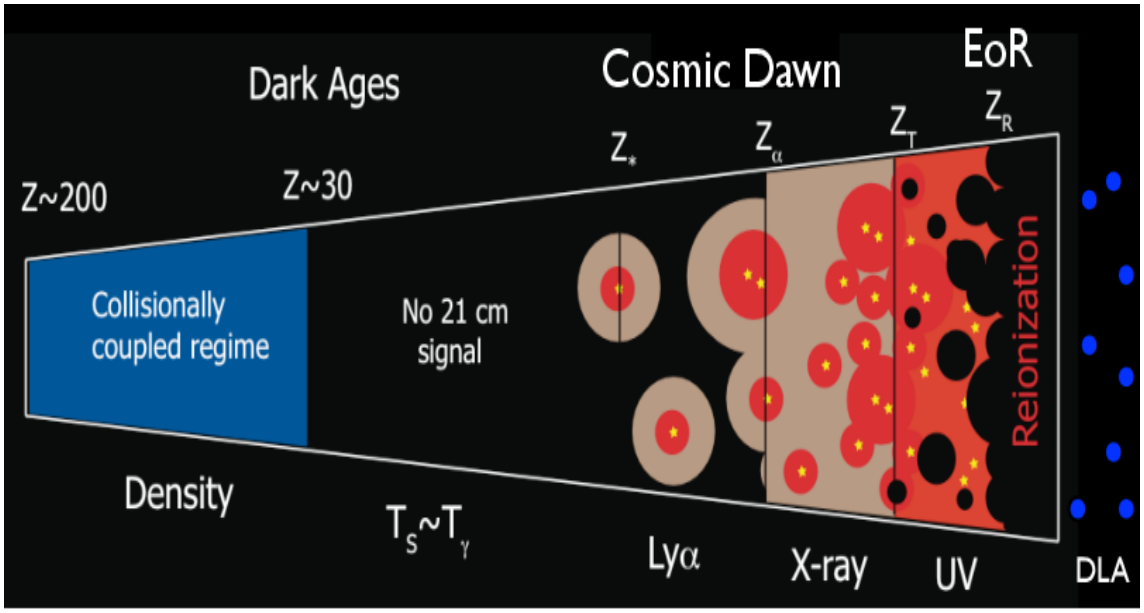


Figure 3.4: The evolution of the global 21 cm signal. The signal transitions from the early phases of collisional coupling. There is no signal when the gas temperature couples to the background CMB temperature. Fluctuations in the later stages are dominated by various heating mechanisms such as Lyman-α, X-ray, and ionizing radiation background. Relevant redshifts accompany the subsequent radiation backgrounds. Image taken from [7]

- $1100 \geq z \geq 200$: after recombination, high gas densities collisionally couple the spin and gas temperature to the CMB, $T_s = T_k = T_{CMB} \propto (1+z)$ and no 21 cm signal is expected, $\bar{T}_b = 0$.

- $200 \geq z \geq 40$: In this regime, the gas decouples from the CMB since the Compton scattering rate falls below the expansion rate. This leads to adiabatic cooling of the gas, $T_k \propto (1+z)^2$ leading to $\bar{T}_b < 0$ and an early absorption signal.

- $40 \geq z \geq z_\star$: As the Universe continues to expand, the gas density decreases, making collisional coupling ineffective. The spin temperature couples to the CMB again, $T_s = T_{CMB}$ and the brightness temperature approaches 0 and there is no 21 cm signal that can be detected.

- $z_\star \geq z \geq z_\alpha$: The process of star formation starts at $z_\star$, These first sources emit both Lyman-α and X-rays, heating the gas significantly. The Wouthuysen-Field effect couples the spin temperature back to the gas such that $T_s \sim T_k < T_{CMB}$ and absorption signals can be detected.

- $z_\alpha \geq z \geq z_h$: As more stars form, Lyman-α coupling saturates, when $x_\alpha >> 1$. Fluctuations in the Lyman-α flux no longer affects the 21 cm signal. At this point, brightness temperature fluctuations are sourced by gas temperature fluctuations. Absorption is seen while the gas temperature remains below the CMB temperature, but hotter regions may begin to be seen in emission as the gas temperature approaches the CMB temperature.

- $z_h \geq z \geq z_T$: 21 cm signal can be seen in emission after the gas is heated above the CMB temperature, $T_k > T_{CMB}$. By this time, the ionization fraction has likely risen to the 1% level. The signal is sourced by a mixture of fluctuations in the ionization fraction, density and gas temperature.

- $z_T \geq z \geq z_r$: As more sources turn on, heating continues and drives the gas temperature well above the CMB temperature, $T_k >> T_{CMB}$. At a redshift z_T the temperature fluctuations become unimportant, $T_s \sim Tk >> T_{CMB}$ and the dependence on the spin temperature in Equation 3.13 can be ignored. Fluctuations in the ionized fraction become dominant at this point.

- $z_r \geq z \geq z$: After reionization, the remaining 21 cm signal would have to originate from collapsed islands of neutral hydrogen

It is important to note that most of these epochs are not well defined and there may be overlaps between them. The exact value of the redshifts stated above are model dependent. This dependency lies in the physics of the first stars, which is still insufficiently understood. The measurement of the global 21 cm signal could therefore constrain a large set of parameters.

3.3 Exotic energy injection and dark matter

The discussion of the 21 cm global signal provides a clear picture of the reionization process. Early stars and quasars play a central role in reionization but their energy contribution is still a matter of debate in the research space. A number of studies have considered beyond standard model physics approach to make predictions for exotic heating of the IGM. Potential candidate sources of energy have been explored and a few present a compelling solution.

Among these candidates, the most promising is dark matter. It is thought that DM annihilation in the early Universe can act as a source of X-rays which lead to ionization, heating and other processes [8]. DM annihilation rate scales as the square of the density, n_{DM}^2, this indicates that it rises with the onset of structure formation and that the collapse of DM into halos can have a significant energy injection in the process of reionization. Annihilation and decay products have the potential to alter the levels of ionization, can heat up neutral gas and increase the production of Lyman-α photons. Figure 3.5 shows the potential WIMP annihilation cross-section constraints coming from CMB limits on the ionized fraction x_e at z $\sim$ 6 for the scenarios of $\chi\chi \to e^+e^-$ and $\chi\chi \to \gamma\gamma$ [8]. It is important to note that these constraints are stronger than those from the Planck experiment [17] and they go beyond the two annihilation presented above. We can understand the effects of DM decays/annihilations on the thermal and ionization evolution of the IGM, which in turn can make us understand how DM affects the 21 cm background signal. The evolution of the ionized fraction x_e is given by the equation from Ref.[108]

$$-\frac{dx_e}{dz} = \frac{1}{H(z)(1+z)}[R_s(z) - I_s(z) - I_x(z)] \tag{3.38}$$

where $I_x = \dot{E}_x/E_0$ represents the ionization rate due to dark matter. I_s and R_s are the standard ionization and recombination rates per baryons. Ref.[9] shows that we can have

$$I_x = \chi_i(z)\frac{\dot{E}_x}{E_0} = f_{abs}(z)\chi_i(z)\Gamma_x f_x \frac{m_p c^2}{E_0} \tag{3.39}$$

for DM decays, and

$$I_x = \chi_i(z)\frac{\dot{E}_x}{E_0} = f_{abs}(z)\chi_i(z)f_x\frac{m_pc^2}{E_0}n_{DM,0}N_b(z)\langle\sigma v\rangle \tag{3.40}$$

for DM annihilation. Where $f_{abs}(z)$ is the energy absorbed fraction, which is the fraction of the DM particle rest mass that is absorbed by the gas at any redshift. $E_0 = 13.6$ eV is the hydrogen ionization energy, m_p is the mass of the proton, χ_i is the fraction of the energy absorbed by the IGM from dark matter decay/annihilation that goes into ionization. $\Gamma_x = 1/\tau_{DM}$ where τ_{DM} is the lifetime of DM particles and finally $n_{DM,0}$ is the current number of DM particles per baryon. The equation that govern the evolution of the IGM temperature can be written as

$$(1+z)\frac{dT_k}{dz} = 2T_k + \frac{I_\gamma x_e}{H(z)(1+f_{He}+x_e)}(T_k - T_{CMB}) - \frac{2\chi_h\dot{E}_x}{3k_bH(z)(1+f_{He}+x_e)} \tag{3.41}$$

where χ_h is the fraction of the absorbed dark matter energy deposited into the IGM as heating [109]. $I_\gamma = (8\sigma_T a_R T_{CMB}^4)/(3m_c c)$ and f_{He} is the helium fraction by mass. One last equation needed for completion is the Lyman-α background intensity J_α written as

$$J_\alpha(z) = \frac{N_H^2 hc}{4\pi H(z)}\left[x_e x_p \alpha_{2^2p}^{eff} + x_e x_{HI}\gamma_{eH} + \frac{\chi_\alpha \dot{E_x}(z)}{N_H h\nu_\alpha}\right] \tag{3.42}$$

where the first and the second term are contributions from recombination and collisional excitations, while the third term is the dark matter contribution. N_H is the number density of HI atoms, $\alpha_{2^2p}^{eff}$ represents the effective recombination coefficient to the 2^2P level. Lastly, γ_{eH} is the collisional excitation rate of hydrogen atoms. This formalism allows us to obtain the 21 cm radiation intensity in the presence of DM.

In this work, exotic energy sources such as WIMPs will be injected in our model universe. We are going to be looking at two different annihilation channels, specifically $b\bar{b}$ and $\tau\tau$. This will allow us to observe how the global 21 cm signal gets altered in the presence of WIMPs of varying masses and annihilation cross sections. An example of DM effects on heating and reionization of neutral gas can be traced via the 21 cm brightness temperature spectrum as shown in Figure 3.6

[9]. This shows the fiducial δT_b without any DM annihilation or decay in solid lines compared to the 25-keV decaying warm dark matter (WDM) (long dash) and 10 MeV decaying light dark matter (LDM) (short dashed) and 10 MeV annihilating LDM (dotted lines). The figure demonstrates that light DM is very effective at influencing the brightness temperature while the WDM is less effective. This means that measurements of the 21-cm background will be able to effectively constrain many models of decaying and annihilating dark matter.

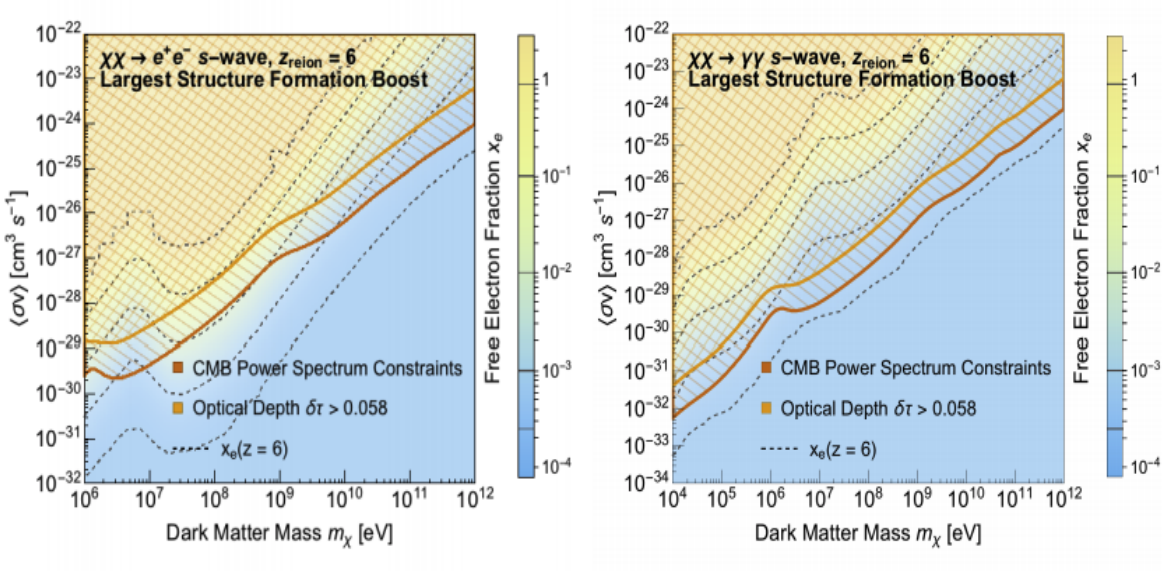


Figure 3.5: Constraints of WIMP annihilation cross-section to reionization for annihilation channels $\chi\chi \to e^+e^-$ (left) and $\chi\chi \to \gamma\gamma$. The hatched regions represents the parameter space ruled out by the optical depth constraints (orange) and the CMB power spectrum constraints measured by Planck (red). The contribution to the free electron fraction x_e is depicted by the colour density plot with the black, dashed contours shown for a contribution to x_e at $z = 6$. image taken from [8].

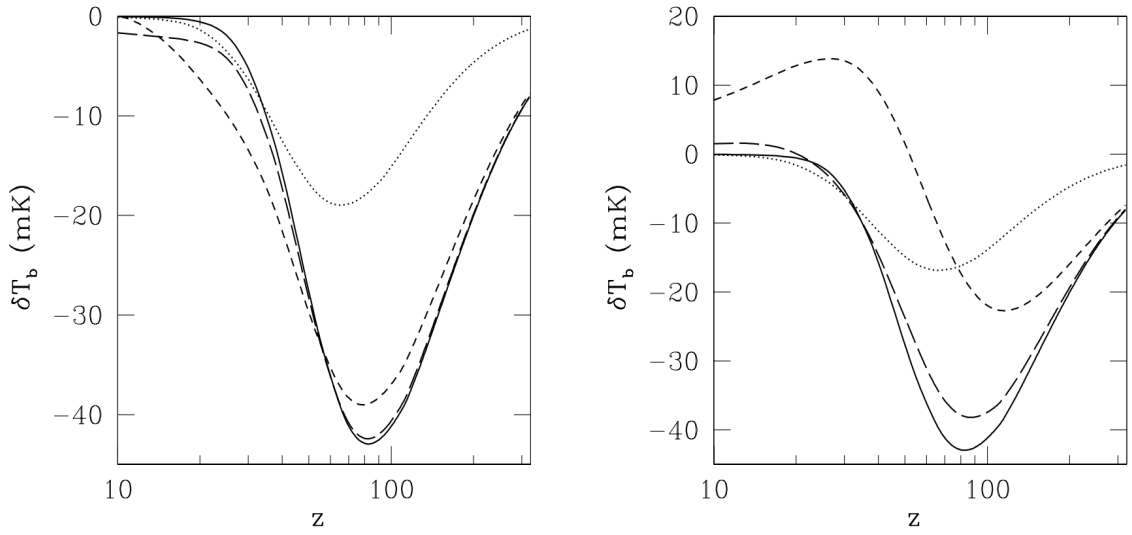


Figure 3.6: The effects of decaying and annihilation WMD and LDM models on the 21 cm brightness temperature. The solid line shows δT_b for a baseline model without any inclusion of DM effects. The dotted line as well as the long dashed and the short dashed lines represent δT_b with 10 MeV annihilating DM, 25 keV decaying WDM and the 10 MeV decaying WDM, respectively. Image taken from [9]

3.3.1 DarkHistory

This section will cover a package called *DarkHistory* by [10] as a method to calculate the exotic energy injection as well as ionization histories to effectively constrain annihilating WIMPs and see how much they affect reionization. *DarkHistory* is a public code package that allows fast and accurate computation of the effects of exotic energy injection on astrophysical and cosmological observables. This work will focus on the interactions that allow DM to annihilate to electromagnetically interacting SM particles. *DarkHistory* allows users to adjust inputs to the calculations such as changing reionization models or the DM annihilation or decay spectrums. The most striking features of the package include:

- The first fully self-consistent treatment of exotic energy injection. The evolution of the IGM temperature T_{IGM} and free electron fraction x_e can be modified by exotic energy injections and previously, this modification was assumed to be perturbative and that the backreaction effects were due to these modifications were negligible. Backreaction is the modification to the ionized /temperature history which in turn modify the energy-loss processes for injected particles. This assumption breaks down before the cosmic dawn [8].

DarkHistory can simultaneously solve for the evolution of the temperature and ionization as well as cooling of the injected particles.

- A self-consistent treatment of astrophysical sources of heating and reionization, this allows for the flexibility of switching between ordinary sources of energy and exotic sources of energy.
- Allows for a significant increase in calculations since there is a pre-computation of relevant transfer functions of particle energy, redshift and ionization levels.
- treatment of helium ionization and recombination of helium
- A novel approach for treatment of inverse Compton scattering (ICS) for high speed electrons.

These improvements allow *DarkHistory* to rapidly scan over a number of different prescriptions for reionization in the form of photoheating or photoionization rates, or a hard-coded background evolution for the free electron fraction x_e. In the subsections below, we will outline the theoretical calculations needed to get the results as well as demonstrate as an example how to use the package.

3.3.1.1 Thermal and ionization histories

DarkHistory can calculate the evolution of the temperature and ionization parameters with exotic energy injections included such as DM using an updated three-level atom (TLA) model for HI and He from **RECFAST** [104, 110]. Without exotic energy injections, the differential equations that describes the matter temperature and ionization fraction can be modelled as

$$\dot{T}_m^{(0)} = -2HT_m + \Gamma_C(T_{CMB} - T_m) \tag{3.43}$$

$$\dot{x}_{HII}^{(0)} = -\mathbf{C}\left[n_H x_e x_{HII}\alpha_H - 4(1 - x_{HII})\beta_H e^{E_{21}/T_{CMB}}\right] \tag{3.44}$$

where H is the Hubble parameter, n_H is the total number density of both neutral and ionized hydrogen. $n_{HII} \equiv n_{HII}/n_H$ where n_H is the number density of free protons. x_e is the free electron fraction and E_{21} is the Lyman-α transition energy. α_H and β_H are case-B recombination and photoionization coefficients for hydrogen respectively. The Peebles-C factor **C** is defined as the probability of a hydrogen atom decaying from a n=2 state to the ground state before photoionization occurs. The Compton scattering rate Γ_C is given by [111]

$$\Gamma_C = \frac{x_e}{1 + F_{He} + x_e} \frac{8\sigma_T a_r T_{CMB}^4}{3m_e} \tag{3.45}$$

where a_r is the radiation constant, σ_T is the Thompson cross-section, m_e is the electron mass and F_{He} is the relative abundance of helium nuclei by number. Exotic sources may inject energy on top of the baseline temperature and ionization histories, $\dot{T}_m^{(0)}$ and $\dot{x}_{HII}^{(0)}$ which can alter the thermal and ionization evolution in the Universe. The rate at which energy is injected from DM annihilating with a velocity averaged cross-section $\langle\sigma v\rangle$ or decaying with some lifetime τ much longer than the age of the Universe is given by

$$\left(\frac{dE}{dVdt}\right)^{inj} = \begin{cases} \rho_{\chi,0}^2 (1+z)^6 \langle\sigma v\rangle / m_\chi, & \text{annihilation} \\ \rho_{\chi,0}(1+z)^3/\tau, & \text{decay} \end{cases} \tag{3.46}$$

where $\rho_{\chi,0}$ is the mass density of DM today. It is important to note that this injected energy does not manifest itself instantaneously as ionization, excitation or heating of the gas. Instead, the primary particles injected into the Universe cools over timescales much larger than the the Hubble time, producing secondary photons that may redshift significantly before depositing their energy into the gas. The energy deposited into a channel c (hydrogen ionization, excitation or heating) can be parametrized once the cooling of injected primary particles can be determined, and it is given by

$$\left(\frac{dE}{dVdt}\right)_c^{dep} = f_c(x, \mathbf{x}) \left(\frac{dE}{dVdt}\right)^{inj} \tag{3.47}$$

The energy deposition also depends on the ionization fraction and the redshift of all the appropriate species in the gas, which can be denoted as $\mathbf{x} \equiv (x_{HII}, x_{HeII}, x_{HeIII})$. For simplification,

helium is ignored, which makes the ionization dependence of these $f_c(z, \mathbf{x})$ only depend on hydrogen, $x_{HII} = x_e$. With additional source terms included, the results of the injected energy on the ionization and thermal histories can be written as

$$\dot{T}_m^{inj} = \frac{2f_{heat}(z, \mathbf{x})}{3(1 + f_{He} + x_e)n_H} \left(\frac{dE}{dVdt}\right)^{inj} \tag{3.48}$$

$$\dot{x}_{HII}^{inj} = \left[\frac{f_{H_{ion}}(z, \mathbf{x})}{R_{n_H}} + \frac{(1 - C)f_{exc}(z, \mathbf{x})}{0.75R_{n_H}}\right] \left(\frac{dE}{dVdt}\right)^{inj} \tag{3.49}$$

where R = 13.6 eV is the ionization potential of hydrogen. $f_c(z, \mathbf{x})$ has been previously calculated with the assumption that the standard ionization history was computed by recombination codes, $\mathbf{x}_{std}(z)$, making redshift the only independent function of f_c. Therefore, these calculations are applicable as long as the purtabations to the assumed ionization history are significantly small. This assumption holds true on the onset of recombination where the ionization history is well constrained by CMB measurements and large perturbations to the free electron fraction are not highly favoured. There is an exception for redshift below 100 where the ionized levels exceed the standard value of $x_e \sim 2 \times 10^{-4}$ by quite a large margin [8]. During the reionization process, star formation causes the ionization and heating processes to happen at an accelerated rate, this makes the thermal and ionization history to separate from the baseline. This in turn decreases a portion of the injected energy that falls into ionizing these species while an increase in x_e increases the number of charged particles available for low-energy electrons to heat the IGM, increasing the energy fraction that goes into heating. Calculating the full $\mathbf{x}$-dependence of $f_c(z, \mathbf{x})$ allows for consistent calculation of temperature and ionization histories with both exotic energy injection processes and reionization.

3.3.1.2 Calculating $f_c(z)$

Energy from low-energy photons and low-energy electrons can be transferred into the excitation and ionization of atoms, it can also go into the heating of the IGM, as well as the addition of free-streaming photons to the CMB continuum. *DarkHistory* has the capability to monitor the amount of energy that low-energy photons and electrons deposit into a channel c $\in$ $(H_{ion}, He_{ion}, exc, heat, cont)$, which represent hydrogen ionization, helium ionization, hydrogen

excitation, heating of the IGM and sub-10.2 eV continuum photons respectively. The function f_c for each channel is found by normalizing the total energy deposited into channel c within a redshift step by the total injected energy according to Equation 3.47. We summarize the important results from [10] for each channel below.

The total amount of energy deposited per unit time and volume is

$$\left(\frac{dE}{dVdt}\right)^{dep} = \left(\frac{dE}{dVdt}\right)^{dep}_{low} + \left(\frac{dE}{dVdt}\right)^{dep}_{high} \tag{3.50}$$

where the energy deposited for a low-energy photon and electron spectra $\mathbf{N}^{\gamma}_{low}[E_i]$ is given by

$$\left(\frac{dE}{dVdt}\right)^{dep}_{low} = \frac{1}{G(z)} \sum_{\alpha} \sum_{i} E'_i \mathbf{N}^{\alpha}_{low}[E_i] \tag{3.51}$$

and for the high energy photons and electrons:

$$\left(\frac{dE}{dVdt}\right)^{dep}_{high} = \frac{1}{G(z)} \sum_{c} E_c^{high} \tag{3.52}$$

where G(z) is the conversion factor between the spectra containing the number number of particles produced per unit time and volume and is written as

$$G(z) \equiv \frac{\Delta log(1+z)}{n_B(z)H(z)} \tag{3.53}$$

This provides glimpses into the splitting of the deposited energy into separate channels.

For *photons*, f_c is computed for low-energy, starting with energy deposition into continuum photons. The photons carry an energy that is $\leq$ 10.2 eV and they cannot efficiently transfer their energy into free electrons or atoms so they just stream freely. Their energy deposition is

$$\left(\frac{dE^{\gamma}}{dVdt}\right)_{cont}^{dep} = \frac{1}{G(z)} \sum_{E_i=0}^{3R/4} E_i \mathbf{N}_{low}^{\gamma}[E_i] \tag{3.54}$$

The amount of energy deposited into hydrogen excitation, assuming that all photons with energies between 3R/4 = 10.2 eV and R = 13.6 eV deposit their energy instantaneously into hydron Lyman-α according to [31]:

$$\left(\frac{dE^{\gamma}}{dVdt}\right)_{exc}^{dep} = \frac{1}{G(z)} \sum_{E_i=3R/4}^{R} E_i \mathbf{N}_{low}^{\gamma}[E_i] \tag{3.55}$$

for ionization, photons above the ionization potential **R** in the above equation have the ability to photoionize one of the species HI, HeI and HeII. The depostion energy for hydrogen ionization is given by

$$\left(\frac{dE^{\gamma}}{dVdt}\right)_{H_{ion}}^{dep} = \frac{R}{G(z)} \sum_{E_i>R} q_H^{\gamma}[E_i] \mathbf{N}_{low}^{\gamma}[E_i] \tag{3.56}$$

and for helium ionization:

$$\left(\frac{dE^{\gamma}}{dVdt}\right)_{He_{ion}}^{dep} = \frac{R_{He}}{G(z)} \sum_{E_i>R_{He}} q_{He}^{\gamma}[E_i] \mathbf{N}_{low}^{\gamma}[E_i] \tag{3.57}$$

For *electrons* the results obtained from the MEDEA code [112] are used to track high-energy electrons as they are injected into the IGM and a similar treatment as in Ref [113] was used. The energy deposition from electrons is given by

$$\left(\frac{dE^{e}}{dVdt}\right)_{c}^{dep} = \frac{1}{G(z)} \sum_{i} p_c(E_i, x_e) E_i \mathbf{N}_{low}^{e}[E_i] \tag{3.58}$$

It is important to note that $\mathbf{N}^e_{ion}$ has already been added to $\mathbf{N}^e_{low}$. The energy of 14eV is used where collisional excitations of hydrogen are possible but not ionization. Below 10.2 eV, electrons can only deposit their energy through Coulomb heating.
Finally, for *high-energy deposition*, a component of the total energy deposited is given by

$$\left(\frac{dE^{high}}{dVdt}\right)^{dep}_c = \frac{1}{G(z)} E^{high}_c \tag{3.59}$$

where the channel c $\in$ [ion, exc, heat]. The high-energy excitation and ionization component is added to the Lyman-α excitation and hydrogen ionization is added for simplicity. Future versions of *DarkHistory* will have a more accurate computation of all the atomic species as well as a more consistent treatment of heium ionization.

The deposition rate with both low-energy photons and low-energy electrons computed becomes

$$\left(\frac{dE}{dVdt}\right)^{dep}_c = \sum_\alpha \left(\frac{dE^\alpha}{dVdt}\right)^{dep}_c \tag{3.60}$$

where $\alpha \in [\gamma, e, high]$

3.3.1.3 Code structure

This section describes the structure and the physics of the *DarkHistory* package. The overall goal of the code is to take in some injected spectrum of electron/positron pair and photons at a particular redshift and partition the energy into several categories over a small z. A flowchart that depicts the overall structure of *DarkHistory* is shown in Figure 3.7.

- *High-energy deposition*: Describes the total energy deposited into excitation, ionization and heating by any high-energy electron that is created from any cooling process;
- *Low-energy electrons*: These are electrons with kinetic energy $\leq$ 3 keV, where atomic cooling processes dominate over Inverse-Compton scattering after recombination.
- *Low-energy photons*: These are photons with energies below 3 keV that either photoionize within the redshift step or below 13.6 eV. These photons can lose all their energy in that

step or cool only through redshifting. This means they can be treated in a simplified manner.

- *Propagating photons*: These are photons that are available at the end of the redshift step, they are not part of the low-energy photons category.

It is worth noting that the positrons are included in the word "electrons" as it encompasses both electrons and positrons. This is valid since the ICS cross-section of electrons and positrons are identical even though they behave differently with how they interact with the gas. The evolution of the temperature and ionization histories at each redshift step are computed using the outputs of the first three categories before the code loops. The looping step can be briefly described as follows:

- *Input*: The user specifies certain conditions before running the code including DM energy injection model as well as photon and electron/positron spectra produced per energy injection event. *DarkHistory* defaults at an initial redshift of 1 + z = 3000, this ensures the accuracy of the spectra of particles during and after recombination. The relevant modules are given in Ref [10].

- *Injected electron cooling*: A combination of atomic processes and ICS are responsible for the cooling of injected electrons and positrons. Transfer functions that map these injected electrons to high-energy deposition, secondary photons from ICS and positron annihilation are computed and applied to the injected electrons.

The sum of the secondary photons produced by the cooling of electrons, photons injected on the redshift step and propagating photons from the last redshift step are used as inputs to the photon cooling transfer functions which are described as follows:

- *Photon propagation and energy deposition*: At this point, a spectrum of photons can undergo a range of cooling processes to lose their energy over this time step. The cooling processes can affect the photon spectrum and reduce it to three transfer functions described in section IIIE in the paper. These transfer functions determine how photons in the current redshift step turn into propagating photons that continue on to the next redshift step. These computations are found in the **main** module in *DarkHistory*.

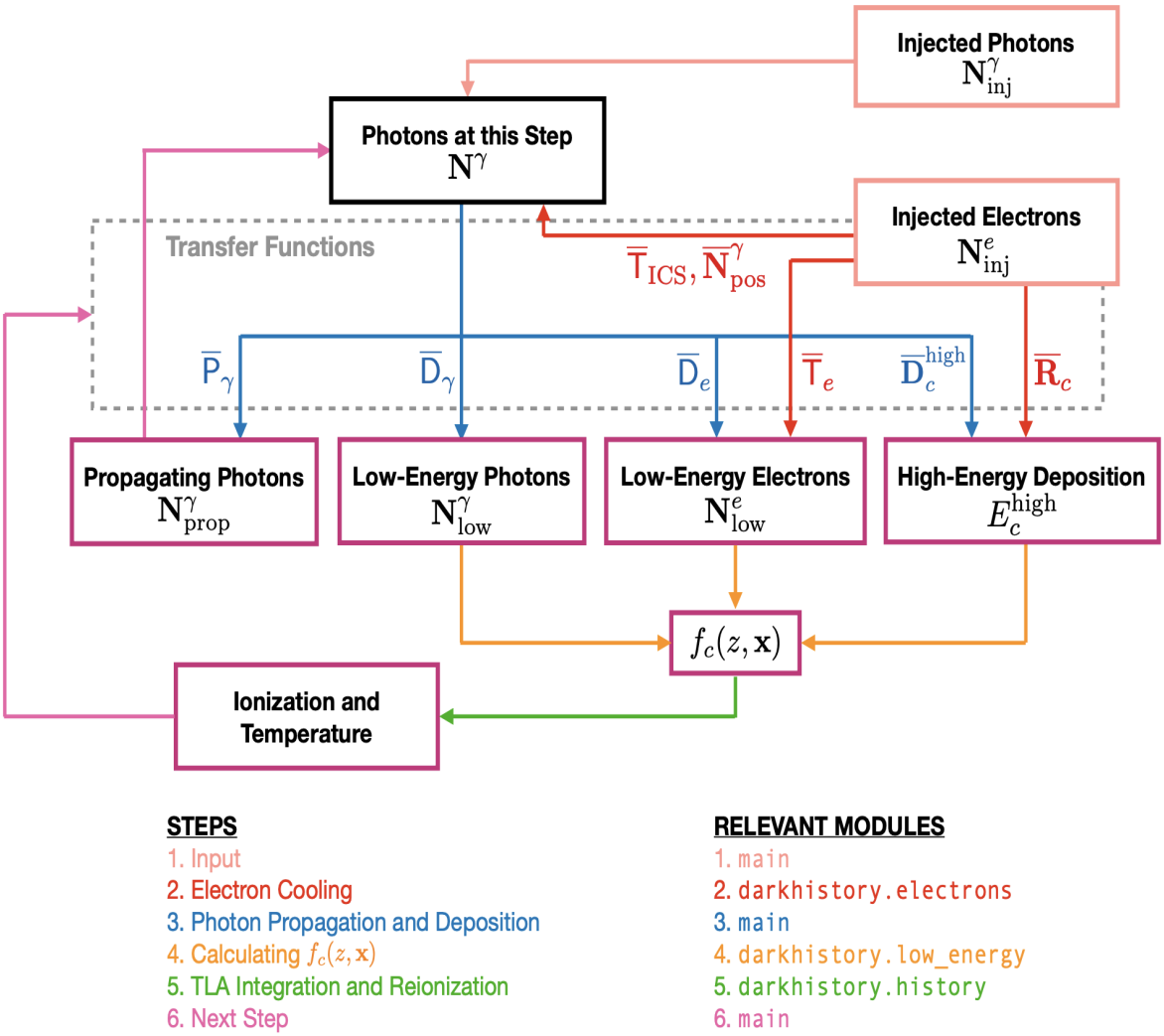


Figure 3.7: Flowchart showing the calculation of ionization and thermal histories in *DarkHistory*.

- *Calculating f_c*: The computations of these ionization fraction has been produced above. They can be found in the **low energy** module.
- *TLA integration and reionization*: With $f_c(z, \mathbf{x})$ available at this time step, the TLA can be integrated. The package is also capable of including reionization calculations and track helium ionization, both of which add extra terms to the TLA. These calculations are found in the **history** module; and
- *Next step*: The $\mathbf{x}$ and T_m values were found in the above calculations and are passed to the next redshift step so that all transfer functions are computed at the appropriate ionization level. The propagating photons found above are also passed on to the next step and the loop repeats.

As an example, Figure 3.8 is obtained using the code demonstrated above. This shows two plots of Temperature and ionzation histories of a simple annihilation model. A 50 GeV Majorana fermion particle that undergoes s-wave annihilation to a pair of $b\bar{b}$ quarks, with an annihilation cross section of $\langle \sigma v \rangle = 2 \times 10^{-26} cm^3 s^{-1}$. Backreaction is included for completeness, in this example the effect of backreaction is small but some examples have a significantly large effect on the matter temperature. A boost to the annihilation rate from structure formation is included and it is described as

$$1 + \beta(z) \equiv \frac{\langle \rho_\chi^2 \rangle}{\langle \rho_\chi \rangle^2} \tag{3.61}$$

For DM masses of ≥ 10 GeV, values of annihilation cross sections required for thermal freeze out are not constrained by the CMB power spectrum energy injection constraints. This means that the ionization fraction which have a $\approx 25\%$ change at high redshifts, does not significantly alter the power spectrum. There is a sudden increase in ionization and temperature at z $\sim$ 30, this is due to the increase in the boost factor.

DarkHistory can also handle calculations that include reionization and helium recombination. It is capable of self-consistently calculate the effects of conventional astrophysical sources of ionization and heating and that of exotic sources. The ICS effects can also be calculated independently to that of the rest of the code, which makes for an efficient and accurate ICS

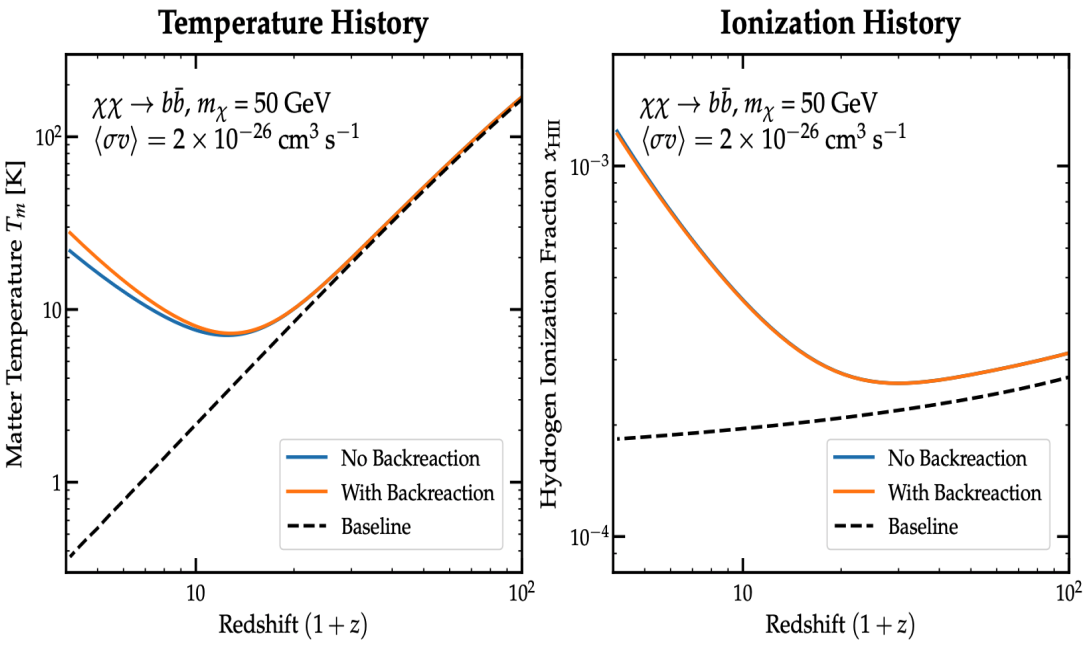


Figure 3.8: Matter temperature (left) and hydrogen ionization history (right) against redshift solved in the presence of dark matter annihilation into $b\bar{b}$ pairs using *DarkHistory* [10]. The blue line shows the histories with energy injection but no backreaction. The orange line shows dark matter annihilation with backreaction and the black, dashed line shows the baseline without any injection.

calculator across a wide variety of electron and photon energies. It is also capable of calculating the effects of dark matter in the global 21 cm measurements which is essential for this work. The results obtained are outlined and discussed in the next chapter.

3.4 Observing the 21 cm signal

We now move on to the observation of the 21 cm signal. The redshifted 21 cm line is observed at a radio frequency of $\nu_{21}(z) = \nu_{21,0}/(1+z)$, where $\nu_{21,0} = 1420$ MHz. Measuring the 21 cm line comes with its own considerable challenges however, these include the effects of instrument noise, galactic foregrounds and contamination from the radio signals from human activity as well as those from the ionosphere. There are two main methods to study the EoR at radio frequencies. The first one is to detect the EoR through statistical means, such as the redshifted 21 cm power spectrum using interferometers like LOFAR, HERA and the SKA to name a few. The second method aims to detect the 21 cm global signal through the full sky observations, usually from dipole experiments such as the Experiment to Detect the Global EoR Signature (EDGES) [114]. This section will briefly cover recent work by EDGES and further investigate whether there is a possibility of measuring the global 21 cm signal using interferometers such as the ones mentioned above, particularly HERA and SKA. This is motivated by the work from Ref.[115, 116, 117, 118].

3.4.1 EDGES

The Experiment to Detect the Global EoR Signature (EDGES) is situated at the Murchison Radio-astronomy Observatory in Western Australia. The experiment has two low-band instruments, each instrument has a calibrated radio receiver that is connected to a single dipole, this is to minimise the frequency-dependent effects. In 2018, the EDGES collaboration detected a strong 21 cm absorption signal at frequency of 78 MHz ($z \sim 17$) with a trough of amplitude 0.5 K [114]. With an absorption signal that is more than a factor of two greater than conventional model predictions, there could potentially be significant implications around this detection. These results could mean one of two things, the first being that the gas between the early stars and galaxies was much colder than what was initially thought or the second case being the background temperature was hotter than expected. There are a number of possible explanations for this dip that have been proposed, one of them is the evidence for dark matter-baryon interaction which would lead to the cooling of the IGM and requires enhanced star formation rates at high redshifts [119, 120]. The other reason is the result of possible astrophysical sources that are capable of producing intense radio synchrotron background in the early Universe [121].

Although the EDGES detection is exciting in terms of opening doors for new phyics, confirmation of the detection from other similar experiments and a thorough analysis of the systematics are required. One of the ways to verify this would be to explore the power of interferometers in their ability to detect the global 21 cm signal.

3.4.2 Can interferometers be used to measure the global 21 cm signal ?

There have been a number of experiments dedicated to measuring the global 21 cm signal, most of them have been single-element experiments. However, the detection of this signal has been a considerable challenge for several reasons, in-spite of the recent work by EDGES. The global EoR signal has been shown to have a maximum amplitude of mK scale, this requires specialized techniques to distinguish it from the radio-loud foregrounds. In particular, The design of a spectral radiometer has a challenging aspect of modeling the receiver noise with the accuracy required for mK measurements as well as the calibration of the instrument as a function of frequency [115]. The issue of foreground radiation becomes even more apparent when these measurements extends to higher redshifts ($z \geq 27$) which is a frequency range of about $\nu \leq 50$ MHz, at these low frequencies the issue of the earth's ionosphere makes the detection even more difficult [116]. Motivated by these challenges, a few methods have been proposed including using interferometers to measure the global signal. One of the main reasons for the use of interferometers is that they are not affected by receiver noise and noise coming from Ohmic losses and passive components in the signal path [122]. There are, however, reasons why one might doubt using interferometers to detect the global signal because of the assumption that interferometers are only sensitive to spatially fluctuating signals on the sky and not the global signal. However, an externally imposed spatial dependence can provide enough spatial structure for an interferometer to be able to detect the global signal [118]. A number of approaches have been employed to take advantage of this fact, for example ref.[118] is using LOFAR in an attempt to observe the global signal from the Moon using lunar occultations technique to introduce the necessary spatial dependence. This approach has provided a high signal-to-noise characterization, this is one example that shows interferometers can deal with noise better than single-element experiments. Ref.[123] used the Large-aperture Experiment to detect the Dark Ages (LEDA), a single dipole experiment, to detect the global signal, however, they use interferometer cross-correlation to help with the calibration. Other references such

as [124, 125, 126] explores a variety of configurations that may make interferometers useful in terms of measuring the global 21 cm signal. In this work, we assume that HERA and SKA will at some point be used to measure the global 21 cm signal and if that's the case then we will try to constrain various DM models in the EoR.

3.4.3 SKA and HERA sensitivity

The Square Kilometer Array (SKA) and the Hydrogen Epoch of Reionization Array (HERA) are the next generation radio telescopes dedicated to observing large scale structure prior and during the epoch of reionization. For this particular research, we will be testing out the sensitivity for *HERA* and *SKA* to compare the results from different DM models [94]. Probing the EoR is a considerable challenge with land-based telescopes because of the terrestial interference, ionospheric refraction and other astrophysical sources [37]. The polarized Galactic synchrotron foreground provides the most challenge since it has $T_{sky} \sim 180(\nu/180MHz)^{-2.6}K$ which is at least four orders of magnitude larger than the signal. It is well understood that the noise level for a single-element telescope can be written as [37]

$$\sigma_S = \frac{T_{sys}/K_a}{\sqrt{\Delta\nu t_{int}}} \tag{3.62}$$

where K_a is the effective collecting area of the telescope, T_{sys} is the system temperature, $\Delta\nu$ is the observed bandwidth and t_{int} is the integration time. The mean global 21 cm signal is about 10 mK, so single-dish telescopes can reach the required sensitivity to detect the 21 cm background. The challenge comes from separating the slowly varying cosmological signals from the foreground and this is where interferometers come in. For an interferometer, the noise per resolution element (with an angular diameter $\Delta\theta$ and spanning a bandwidth $\Delta\nu$) is then [94]

$$\Delta T_{noise} \sim 2mK \left(\frac{10^5 m^2}{A_{eff}}\right)\left(\frac{10'}{\Delta\theta}\right)\left(\frac{1+z}{10}\right)^{4.6}\left(\frac{MHz}{\Delta\nu}\frac{100hr}{t_{int}}\right)^{1/2} \tag{3.63}$$

where A_{eff} is the effective collecting area and t_{int} is the integration time. These angular and frequency scales correspond to $\sim$ 30 Mpc. The relevant data for both HERA and SKA are provided in Ref [94] and [37]. Due to the fact that only large scales are accessible to imaging,

even with a large telescope, the current HERA program emphasizes statistical measurements with interferometers. However, we have pointed out that this could also be used for the global 21 cm measurements when appropriate techniques are applied to the interferometer. We need to note however, that the sensitivity may be reduced by the method of observation using an interferometer thus our limits may be optimistic.

Chapter 4

The Effect of Dark Matter in the Epoch of Reionization

This chapter outlines the results obtained in this work. This will be separated into two different annihilation channels, $b\bar{b}$ and $\tau^+\tau^-$. The analysis begins with the evolution of the global 21 cm signal with and without DM so as to build up intuition as to how the inclusion of WIMPs affects the ionization and thermal history of the Universe. This will also allow us to understand which parameters are most important as they are varied. We will begin with a 100 GeV WIMP with annihilation cross section of $\langle \sigma v \rangle = 3 \times 10^{-26}$ cm$^3 s^{-1}$ and compare it with the case without DM, we will call this the *baseline* case from now on. The *baseline* is the default signal without DM, as stated, and the Puchwein reionization [127] model is used with helium included in the evolution history calculations. The derived global signal will then be compared with the noise from EDGES to see whether it can be detected by the experiment. We will then proceed with comparing the results of DM models with the sensitivity of HERA and the SKA. The idea is to find the smallest annihilation cross section $\langle \sigma v \rangle$ for each WIMP mass that produce results larger than the total noise in the redshift range. Lastly, we will wrap it up by checking how our results compare to the existing literature.

4.1 $b\bar{b}$ annihilation channel

4.1.1 Global 21 cm signal

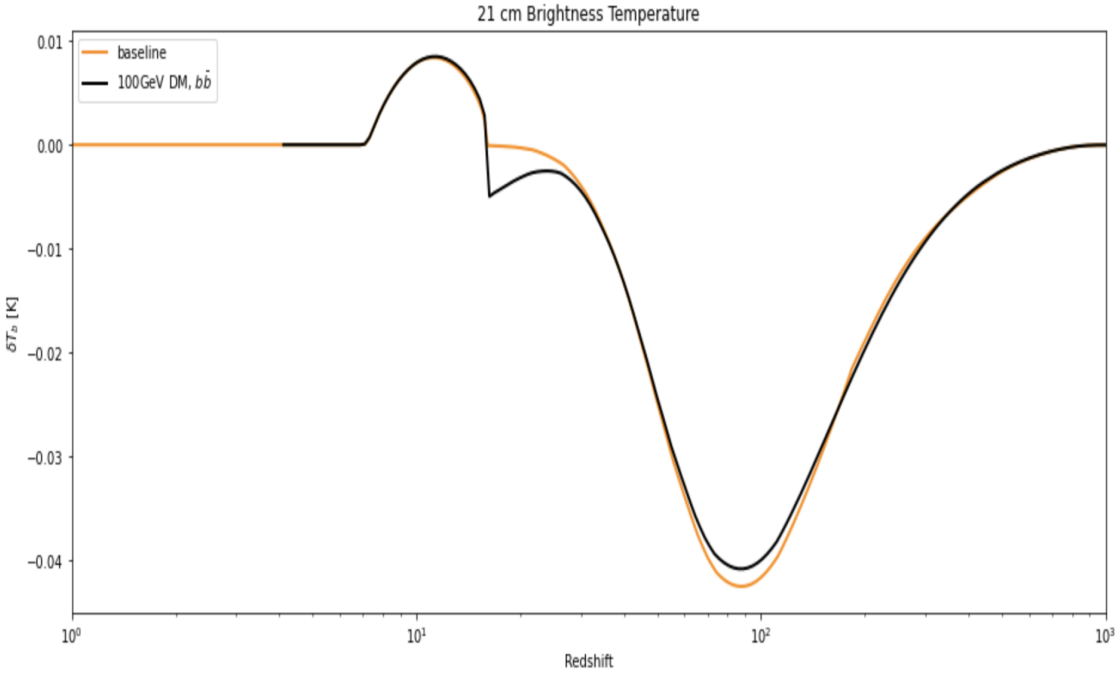


Figure 4.1: The global 21 cm brightness temperature for the baseline (black) case compared to the 100 GeV DM with $\langle\sigma v\rangle = 3 \times 10^{-26}$ cm^3 s^{-1} (orange)

The evolution of the 21 cm brightness temperature for 100 GeV WIMP with annihilation cross section $\langle\sigma v\rangle = 3 \times 10^{-26}$ cm^3 s^{-1} and the baseline is plotted in Figure 4.1. Before we move on further, we have to stress that our model looks different from [7] because we haven't considered any astrophysical sources of Lyman-α photons such as stars and AGNs at redshift z $\sim$ 30. These would strengthen the Lyman alpha coupling around redshift z $\sim$ 30 and cause the dip in the 21 cm spectrum. We are mostly interested in the effects of DM, as in the example case of ref.[9] which also does not include these sources, as can be seen from Figure 3.6. Now looking at z $\sim$ 100, during the Dark Ages, we see that there is a reduction in the absorption trough for the DM case compared to the baseline because DM is heating the neutral hydrogen at this period and this causes a little bit of emission. It is worth noting that in ref.[9], the various DM models they use reduce this trough quite substantially compared to ours, this is due to the updated efficiency function F_c that is provided by *DarkHistory*. When we look to z $\sim$ 30, we notice that instead of heating and reducing the absorption trough as seen in ref.[86], we are inducing an absorption feature in the case of DM, albeit very small. This means that had we included

the sources of Lyman-α, the trough at that redshift would have slightly deepened, which could indicate that DM activity could potentially contribute to the explanation of the large depth observed by EDGES. As can be seen, there is a sharp edge in the absorption feature. We try to explain this as well as the physics underlying the global signal in the plots below.

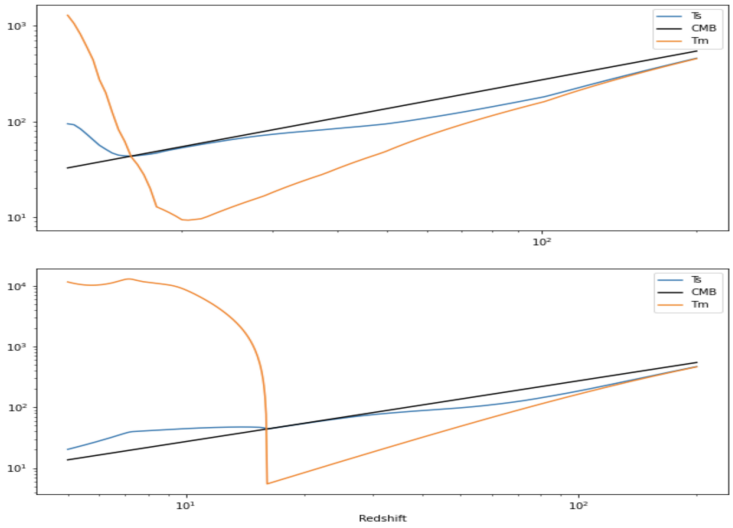


Figure 4.2: Spin temperature and the matter temperature plot from ref.[11] (Top) and the same plots for our *Darkhistory* case (bottom). The orange plot is the matter temperature, blue is the spin temperature and the black one is the CMB.

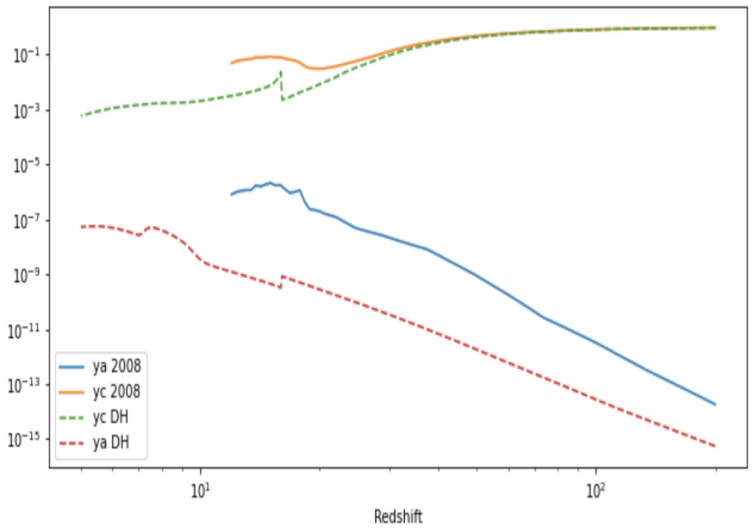


Figure 4.3: Coupling coefficients from ref.[11] compared to the *Darkhistory* ones. The solid orange and blue are the collisional coupling (yc) and the Lyman-α coupling (ya) for ref.[11] respectively and the dashed green and red are the collisional coupling and the Lyman-α coupling for *Darkhistory*.

First, we see that the sharp features in our brightness temperature plot coincides exactly with that in the matter temperature Tm history from DarkHistory according to Figure 4.2. Hence,

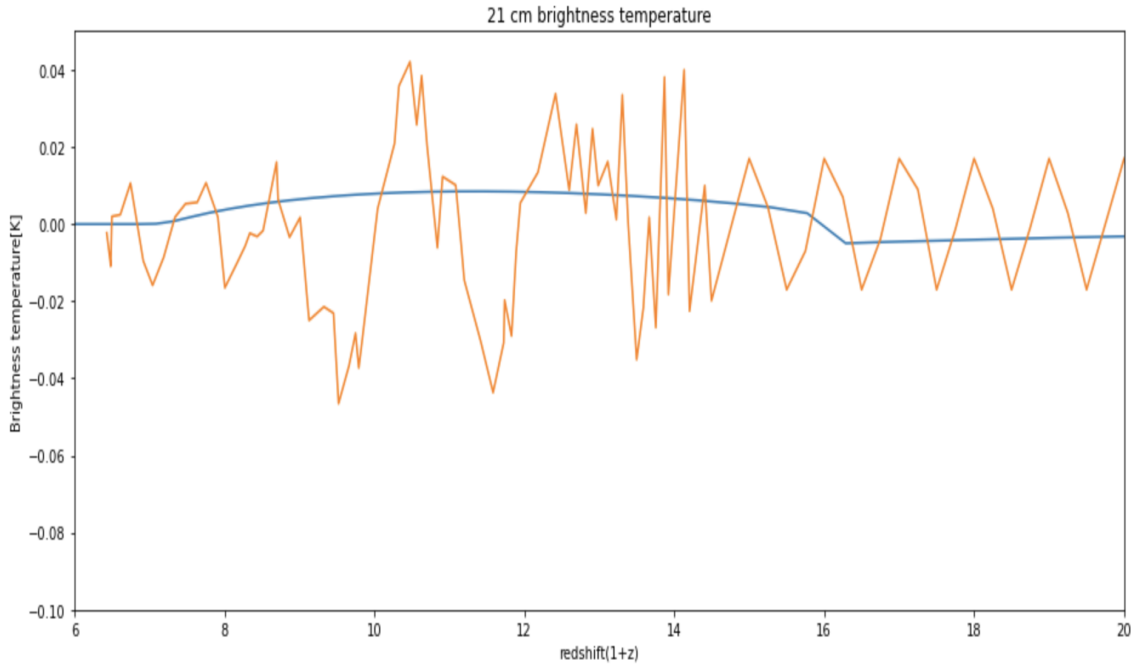


Figure 4.4: Brightness temperature for the 100 GeV DM case (blue) sensitivity against the EDGES noise (orange) with 6 hour integration time from ref.[12].

all our sharp features are consequences of DarkHistory. Secondly, we see that yc becomes weak (substantially smaller than 1, the magnitude of the CMB coupling) after z $\leq$ 100. In the absence of strong yc or ya the Ts will align to T_{CMB}. Since yc cannot be strong in this regime it must mean we are missing contributions to ya, which, if stronger, would push Ts away from T_{CMB} towards the lower Tm value and produce our z $\sim$ 20 dip. Before we can proceed to the interferometers, it is important to compare these results with the EDGES noise. We show this in Figure 4.4. The graph shows how our results fare against the rms noise from EDGES with a 6 hour integration time [12]. The EDGES plot show the residuals of the integrated spectrum to a five-term polynomial fit with a weighted rms of 17 mK. We observe that at this current form, our results show a rather bad sensitivity, this is due to the fact that we omitted the trough at z $\sim$ 20. However, we have to point out that the noise will drop off with a factor of $\sqrt{6\text{hrs}/t_{\text{int}}}$, so a longer observation time might make EDGES more effective, for example, a 1000 hour observation time will reduce the noise by more than a factor of 10. If we include the astrophysical sources at this redshift we will be able to observe the trough outside the noise. Again, it is worth stressing that for our particular study, we wanted to observe the effects of DM without any interruption from the other sources. We will include the astrophysical sources in future work, our focus is rather on the limits that can be produced by interferometers.

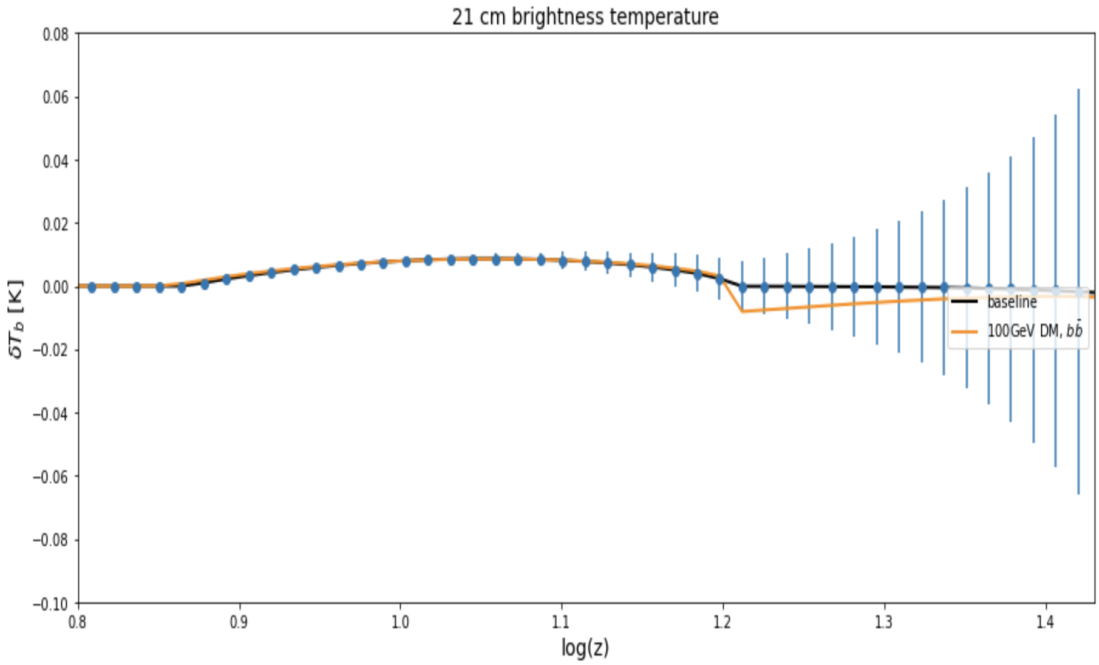


Figure 4.5: The global 21 cm brightness temperature for the baseline (black) case compared to the 100 GeV DM with $\langle \sigma v \rangle = 4 \times 10^{-26}$ cm^3 s^{-1} (orange) with HERA noise (blue)

.

We have mentioned that the 21 cm signal is affected by the energy injection and it is sensitive to the mass and the annihilation cross section, it is now appropriate to analyze how these can be detected. For HERA observations, assuming that Equation 3.63 holds for interferometers, the effective collecting area is $A_{eff} = 10^5$ m^2, the integration time is 1000 hours. The smallest annihilation cross section that is larger than the total noise for HERA for the DM mass $m_\chi =$ 100 GeV is $\langle \sigma v \rangle = 4 \times 10^{-26}$ cm^3 s^{-1} for 1σ sensitivity. The error bars increase with higher redshifts, which makes sense since the foreground contamination will be added to the ionosphere effects. However, the fact that all these foreground signals are smooth spectrum sources and the spectrum of the EoR is expected to be rough allows us to try and isolate the signal. It is worth noting that HERA will not be making observations beyond z $\sim$ 13, This is also the reason why the error bars increase substantially after that. This results shows how powerful interferometers could be for the observation of the global signal. We saw that for single-element experiments like EDGES, we had a bad sensitivity but this is not the case here.

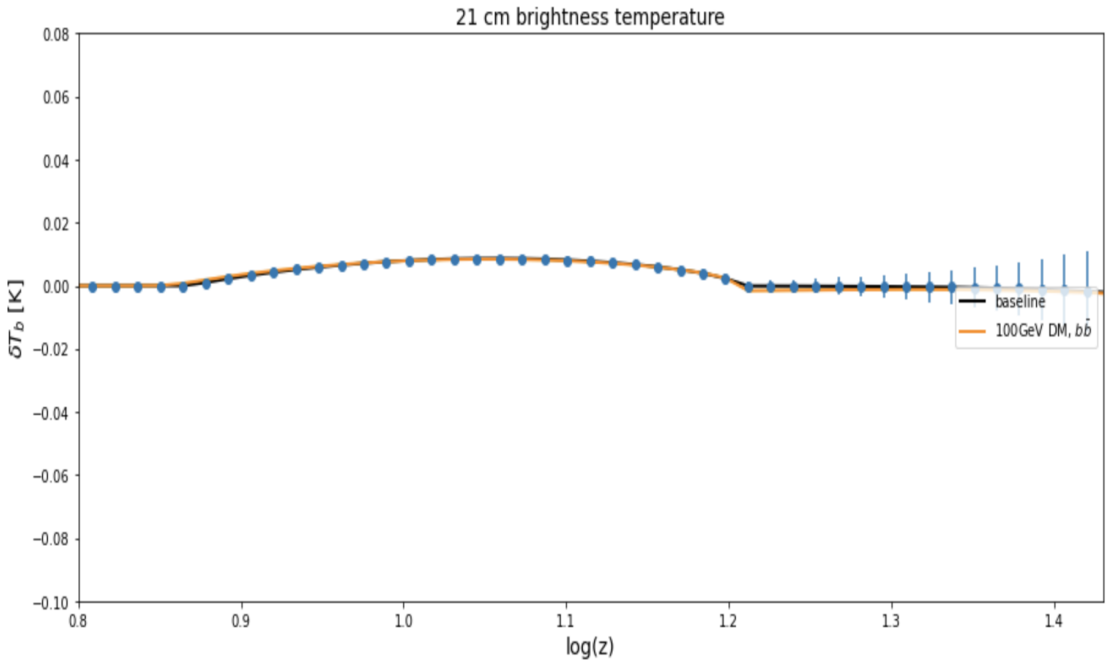


Figure 4.6: The global 21 cm brightness temperature for the baseline (black) case compared to the 100 GeV DM with $\langle\sigma v\rangle = 9 \times 10^{-27}$ cm^3 s^{-1} (orange) with SKA noise (blue)

For the SKA, the noise is much smaller than that of HERA because the effective collective area is one order of magnitude larger at $A_{eff} = 10^6$ m^2 for the same integration time of 1000 hours. The minimum annihilation cross section that the SKA will detect for $m_\chi = 100$ GeV is $\langle\sigma v\rangle = 9 \times 10^{-27}$ cm^3 s^{-1} for 1σ. This is much smaller than the minimum annihilation cross section that HERA can detect, this proves the power of the instrument as a probe to measure the effect of dark matter in reionization. The SKA is capable of probing the Universe well beyong z $\sim$ 13 up to a redshift of 27 and it will be able to provide clear details of the ionization and thermal histories going back to the cosmic dawn. And if necessary techniques are applied so as to measure the global 21 cm signal, we can see that it could be the most useful probe of the EoR. Let us make a comparison between a range of dark matter masses and annihilation cross sections that can be detected by HERA and the SKA to get a full scope.

4.1.2 HERA vs SKA constraints

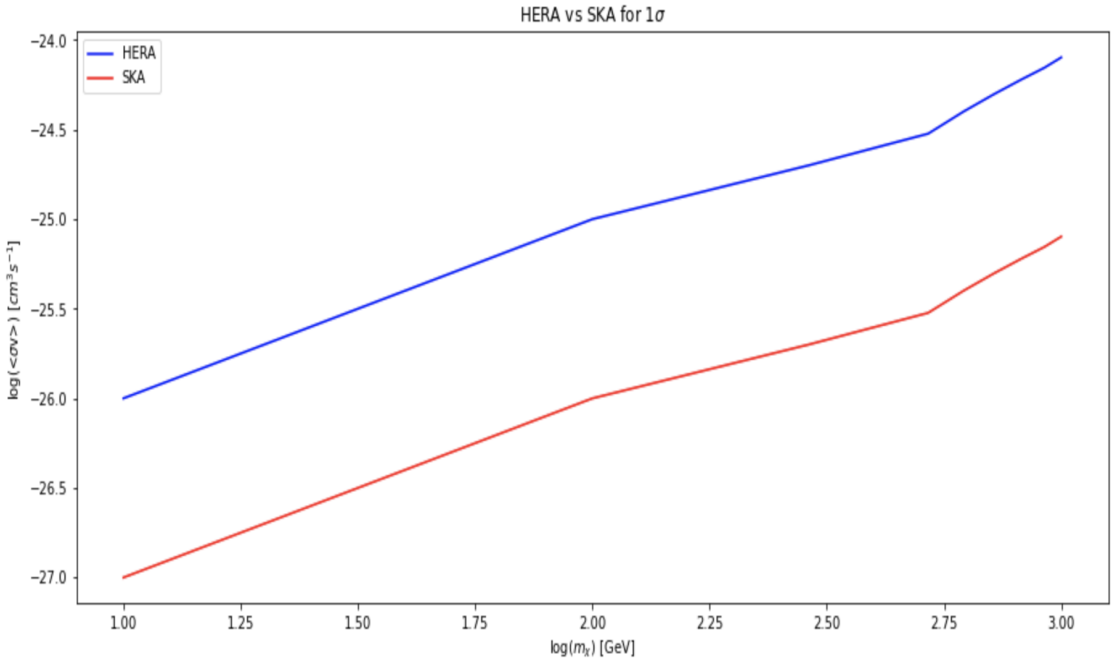


Figure 4.7: Sensitivity constraints on the DM annihilation cross section for DM annihilating into $b\bar{b}$ final state for 1σ c.l with HERA and SKA after 1000 hours of integration time. The blue line represents the HERA constraints and the red line represents the SKA constraints.

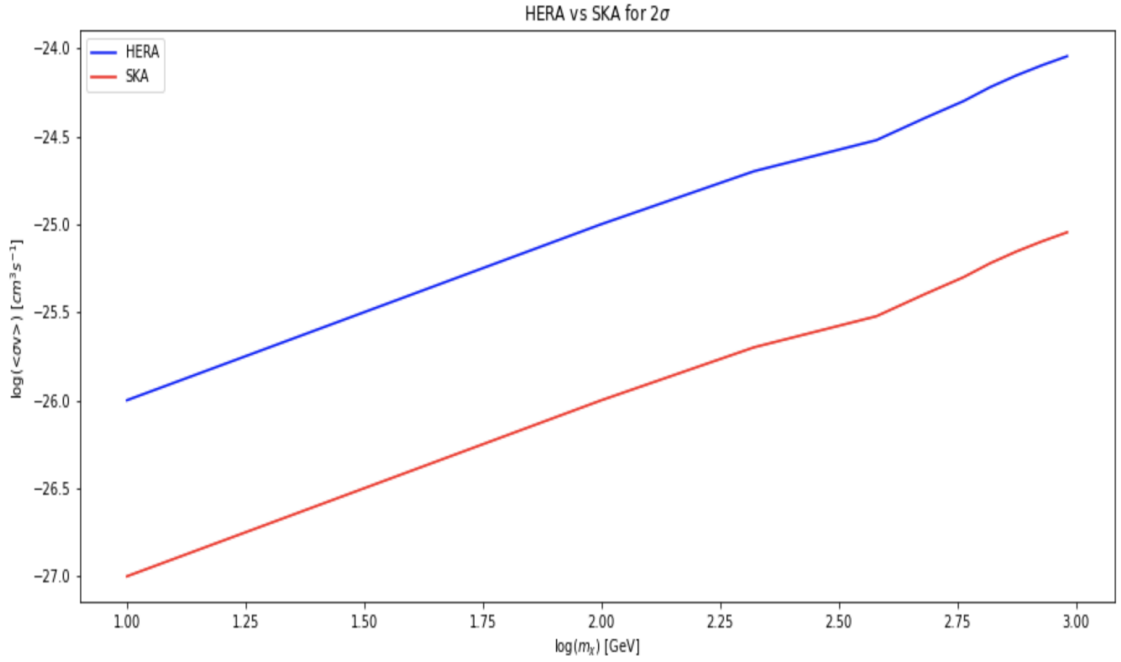


Figure 4.8: Sensitivity constraints on the DM annihilation cross section for DM annihilating into $b\bar{b}$ final state for 2σ c.l with HERA and SKA after 1000 hours of integration time. The blue line represents the HERA constraints and the red line represents the SKA constraints.

In Figure 4.7 and Figure 4.8 we plot our constraints on the DM annihilation cross section, for the HERA measurements (blue) and for the SKA (red) for 1σ c.l and 2σ c.l respectively. As expected, the SKA is the most constraining instrument by at least one order of magnitude for every dark matter mass. The annihilation cross section for the SKA at a mass of 100 - 200 GeV remains constant for the two plots, this is around the value of the thermal relic abundance i.e 10^{-26} cm^3 s^{-1}. From this, it appears that HERA shows more promise for low mass models, being able to exclude the relic cross section for masses $\leq$ 100 GeV but the SKA can reach masses $\leq$ 1000 GeV. The SKA, apart from being bigger than HERA in terms of the effective collecting area, it is also capable of detecting and characterizing ionized structures and HI brightness temperature fluctuations on 5-300 arcmin scales over the epoch of reionization and cosmic dawn redshift ranges z = 6 - 27 to about 1 mK brightness temperature levels. From this, it is easier to derive the state, chemistry and thermal history of the IGM as well as any changes induced by the exotic energy injections.

The results were also compared to other similar experiments, as seen in Figure 4.9 and Figure 4.10. The first figure from [13] uses a range of boost factor models from low to high, with the data described in the code from Ref.[128]. Figure 4.10 on the other hand, shows the upper limits from Ref.[14] and Ref.[15], which are from gamma-ray observations and are often thought to be the benchmark in indirect detection of DM. The first figure, Figure 4.9 shows how our constraints on the DM annihilation cross section performs against constraints from [13] for the current measurement uncertainty of $\Delta\tau = 0.012$, this is better than Planck's current measurement of 0.066 [17]. The upper and lower limits are depicted by the black dotted lines for each annihilation channel. Our constraints are less competitive with the ones from [13] for high mass DM particles, in their study a high boost factor model different to ours was adopted. In their model, the total optical depth is enhanced significantly from 0.059 to 0.068 at z $\sim$ 10-50. Our reionization model allows for better constraints at lower masses, this is because their model was chosen to have a slightly lower optical depth relative to the mean measured value. It is also worth noting that their model does not does not lead to very efficient reionization since high energy electrons and photons do not interact significantly with the IGM due to their reionization model [129]. This is different for our case because we use the updated efficiency functions as well as the updated heating parameters. Figure 4.10 shows the observed limit from a combination of 15 dSphs analysis (solid black line) and the solid red line represents the spectroscopically measured J-factors with an uncertainty of 0.6 dex. From the analysis, it is worth noting that

our SKA constraints are competing with the compared plots, especially at low masses. The derived upper limit that lies above the median expectation for masses below $\sim$ 70 GeV while for our constraints it is $\sim$ 100 GeV.

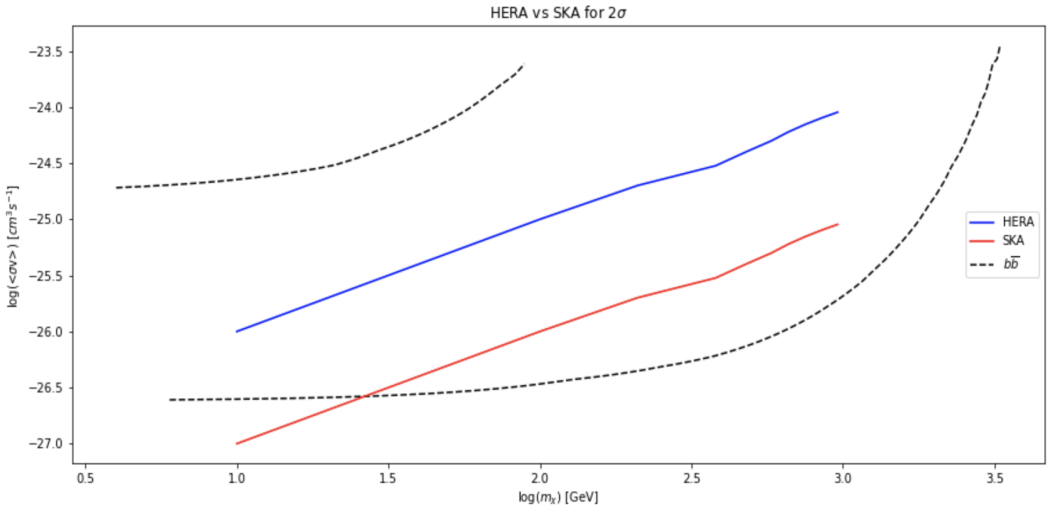


Figure 4.9: Sensitivity constraints on DM annihilation cross section for DM annihilating into $b\bar{b}$ final state for 2σ c.l with HERA and SKA after 1000 hours of integration time compared to the constraint on the DM annihilation cross section for $b\bar{b}$ final states from Ref.[13]. The blue line represents the HERA constraints and the red line represents the SKA constraints. The black dotted lines represents the constraints of DM annihialtion cross section corresponding to the current optical depth measurements of $\Delta\tau = 0.012$.

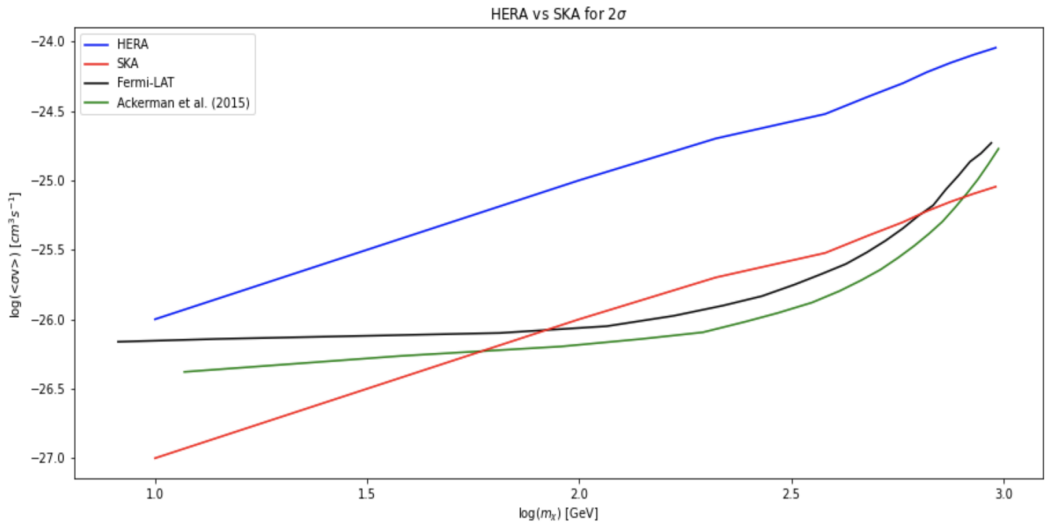


Figure 4.10: Sensitivity constraints on DM annihilation cross section for DM annihilating into $b\bar{b}$ final state with HERA and SKA for 1000 hours of integration time compared to the upper limits on the DM annihilation cross section from Ref.[14] (solid black line) and Ref.[15] (solid red line) for $b\bar{b}$ channel at 95% confidence interval.

4.2 $\tau^+\tau^-$ annihilation channel

4.2.1 Global 21 cm signal

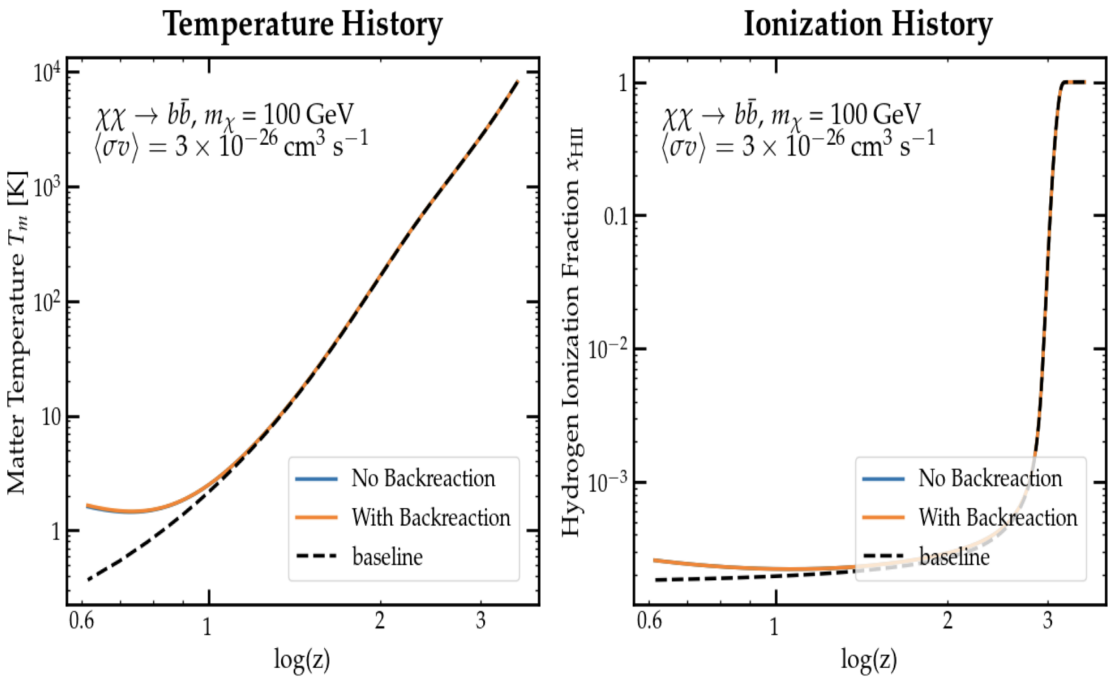


Figure 4.11: The computed matter temperature T_m and hydrogen ionization fraction $x_{H_{II}}$ (right) in the presence of 100 GeV WIMP DM particle annihilation into $\tau^+\tau^-$ with cross section of 3 $\times 10^{-26}$ cm^3 s^{-1}.

.

Figure 4.11 shows the matter temperature and the hydrogen ionization fraction for a DM particle with mass $m_\chi = 100$ GeV undergoing an s-wave annihilation with a cross section of $\langle\sigma v\rangle = 3 \times 10^{-26}$ cm^3 s^{-1} with (blue) and without (orange) backreaction. The effects of backreaction are even smaller for this particlular channel. We note that T_m and $x_{H_{II}}$ for the DM are significantly smaller than the case of $b\bar{b}$ and the impact of structure formation is delayed. $T_m \sim 2$ K for $\tau^+\tau^-$ whereas it was ≥ 10 K for the $b\bar{b}$ case. We also see that $x_{H_{II}} \sim 10^{-3}$ for the $b\bar{b}$ and now it is much less than that. This is due to the fact that τ is a heavier particle which affects the dark matter mass. This increases the the IGM temperature significantly less relative to the case of $b\bar{b}$. This gives us a brief indication of how the global 21 cm signal will be affected.

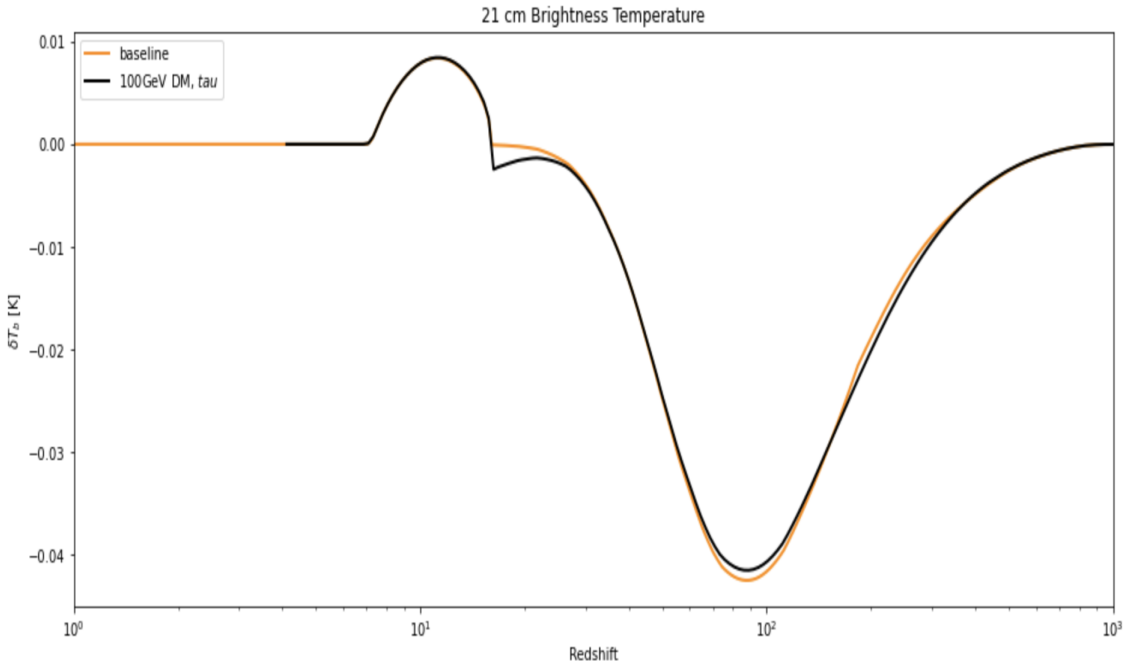


Figure 4.12: The global 21 cm brightness temperature for the baseline (black) case compared to the 100 GeV DM with $\langle\sigma v\rangle = 3 \times 10^{-26}$ cm^3 s^{-1} (orange).

Figure 4.12 shows the evolution of the 21 cm signal for a DM particle with mass $m_\chi = 100$ GV with a cross section of $\langle\sigma v\rangle = 3 \times 10^{-26}$ cm^3 s^{-1} annihilating through the $\tau^+\tau^-$ channel. Firstly, looking at the large dip at z $\sim$ 100 we notice that the difference is smaller than that of the b$\bar{b}$ channel, this suggests that DM does not heat up the gas as much from this channel. This behaviour extends to the absorption feature at z $\sim$ 30 which shows a slightly smaller difference compared to Figure 4.1. The efficiency functions seems to have been nullified more for this channel and but there are still imprints of DM nonetheless. We also see a very sharp edge for this particular example but we have already explained that this is a consequence of DarkHistory. We chose not to include a sensitivity plot against the leading EoR experiment EDGES, this is because the plot looks almost identical to Figure 4.4 but we still come to similar conclusions - The omission of the Lyman-α sources makes our sensitivity bad but this will be improved by future work. We mainly focus on the work on interferometers.

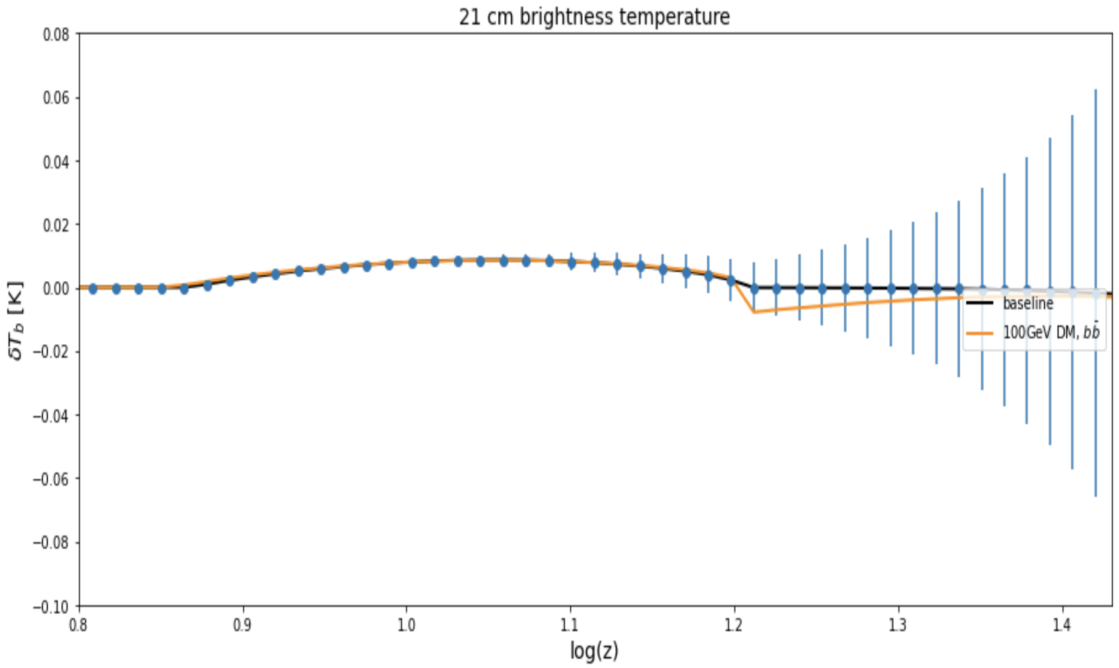


Figure 4.13: The global 21 cm brightness temperature for the baseline (black) case compared to the 100 GeV DM with $\langle \sigma v \rangle = 1 \times 10^{-25}$ cm^3 s^{-1} (orange) with HERA noise (blue).

The analysis from HERA with integration time of 1000 hours indicates that the smallest annihilation cross section that can be detected for DM mass $m_\chi = 100$ GeV is $\langle \sigma v \rangle = 1 \times 10^{-25}$ cm^3 s^{-1} for 1σ as can be seen in Figure 4.13. This is much larger than the one found for the $b\bar{b}$ channel because of the heavier nature of the τ particle which would need a larger cross section to be detected. This observation also suffers from the same limitations as in the $b\bar{b}$ case for the reasons mentioned.

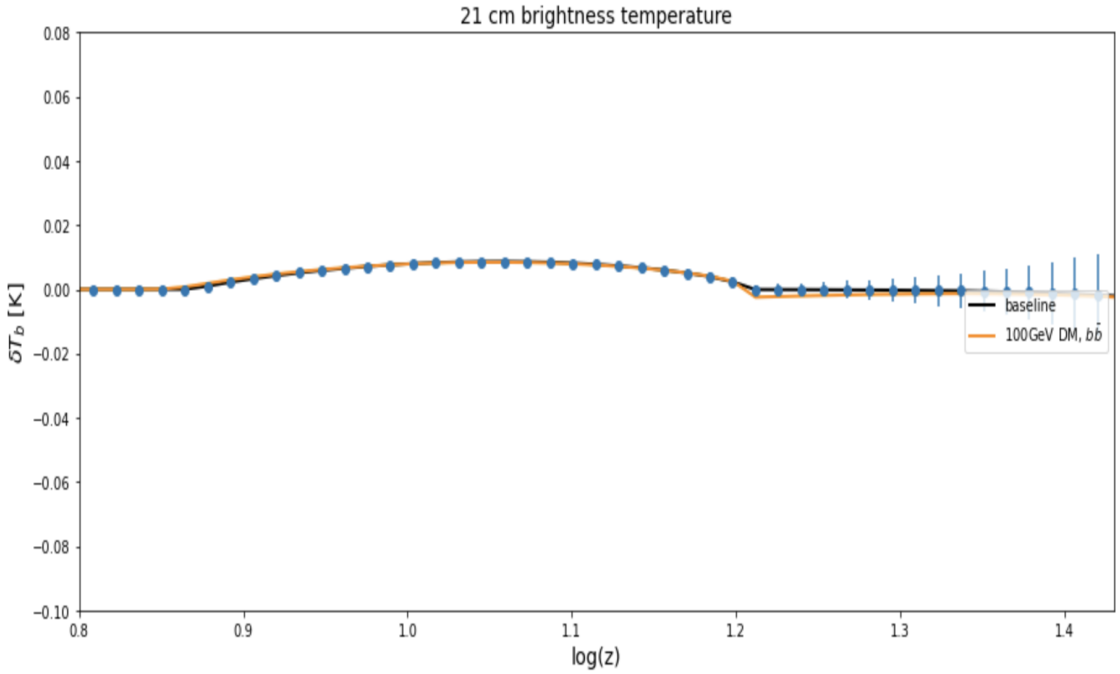


Figure 4.14: The global 21 cm brightness temperature for the baseline (black) case compared to the 100 GeV DM with $\langle\sigma v\rangle = 1 \times 10^{-26}$ cm^3 s^{-1} (orange) with SKA noise (blue).

The SKA noise, which is much smaller than that of HERA can detect the minimum annihilation cross section of $\langle\sigma v\rangle = 1\times10^{-26}$ cm^3 s^{-1} for the same DM mass of m$_\chi = 100$ GeV for integration time of 1000 hours and 1σ c.l. This value is bigger than that of $b\bar{b}$ as expected by now because of the nature of the two annihilation channels. This allows us to constrain the different annihilation channels for the respective DM masses for both HERA and the SKA and compare it to similar work.

Figure 4.15 and Figure 4.16 shows the constraints on the DM annihilation cross section for the $\tau^+\tau^-$ channel for HERA (blue) and SKA (red) 1σ and 2σ respectively. We note that there is an order of magnitude difference between the two instruments as expected. The HERA constraints remain below the relic abundance cross section of $\langle\sigma v\rangle = 3 \times 10^{-26}$ cm^3 s^{-1} up until m$_\chi$ = 300 for 1σ, however this is not true for 2σ since it exceeds that limit at very low masses. This indicates that HERA could be used to detect all the mass ranges below that and the SKA could be used to detect high mass DM particles. Looking at the comparisons with [13] in Figure 4.17 we see that for the $\tau^+\tau^-$ channel our constraints are competitive at high mass range, especially for the SKA. For Figure 4.18 we note that our constraints are less competitive, with the Fermi-LAT derived upper limits being above the median expectation for masses below $\sim$ 70 GeV. This is due to the low-significance excess mentioned in Ref.[14].

4.2.2 HERA vs SKA constraints

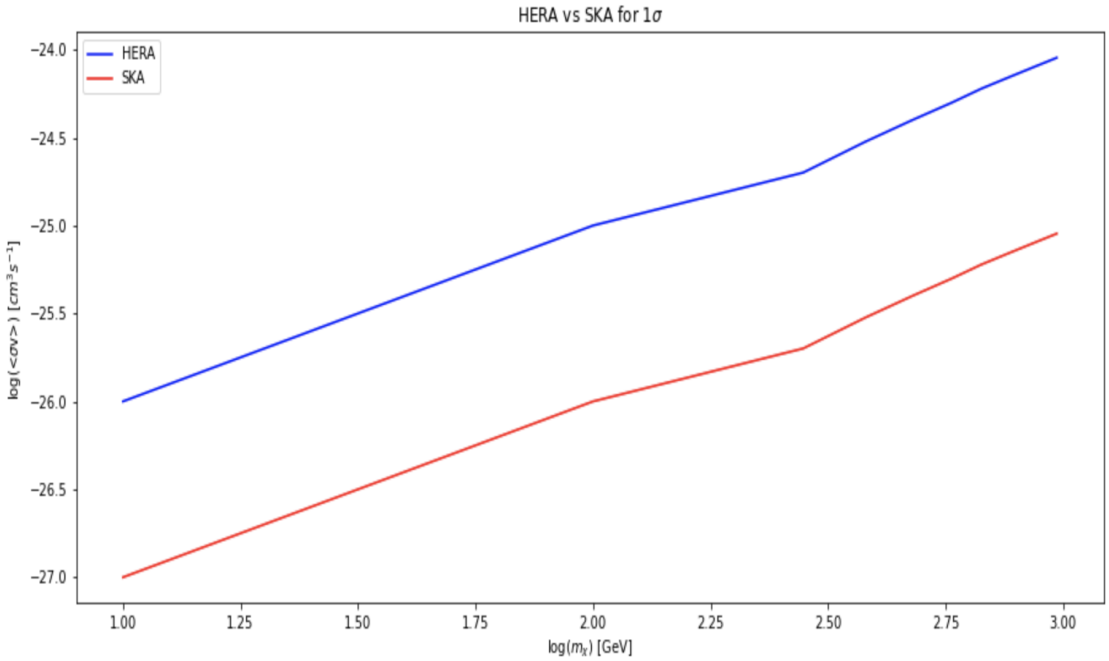


Figure 4.15: Sensitivity constraints on the DM annihilation cross section for DM annihilating into $\tau^+\tau^-$ final state for 1σ c.l with HERA and SKA after 1000 hours of integration time. The blue line represents the HERA constraints and the red line represents the SKA constraints.

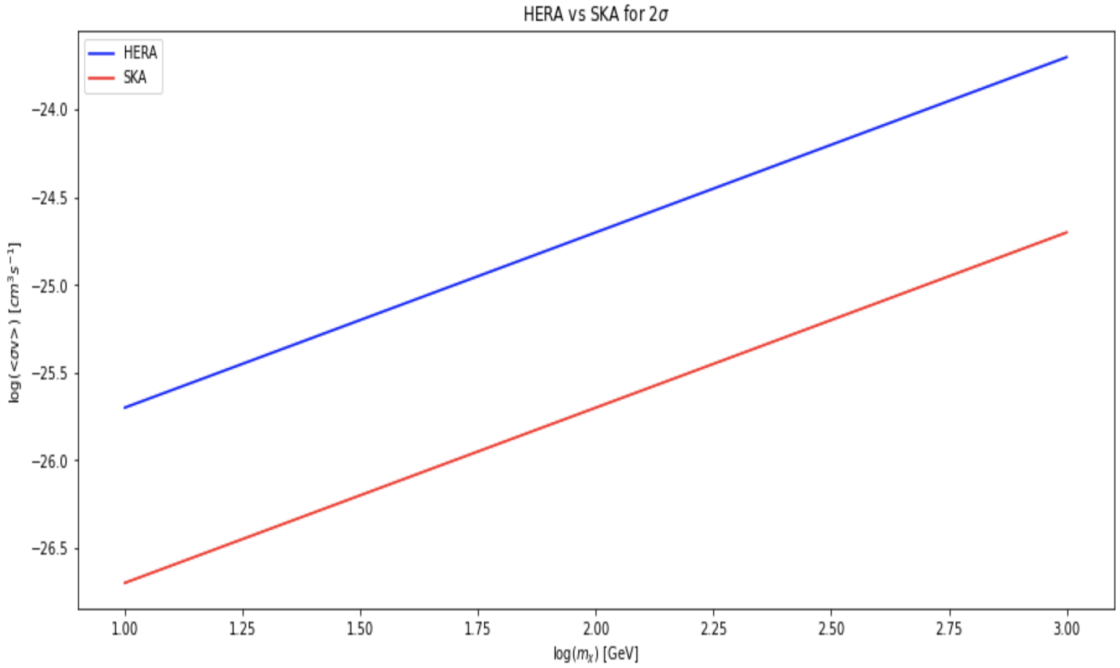


Figure 4.16: Sensitivity constraints on the DM annihilation cross section for DM annihilating into $\tau^+\tau^-$ final state for 2σ c.l with HERA and SKA after 1000 hours of integration time. The blue line represents the HERA constraints and the red line represents the SKA constraints.

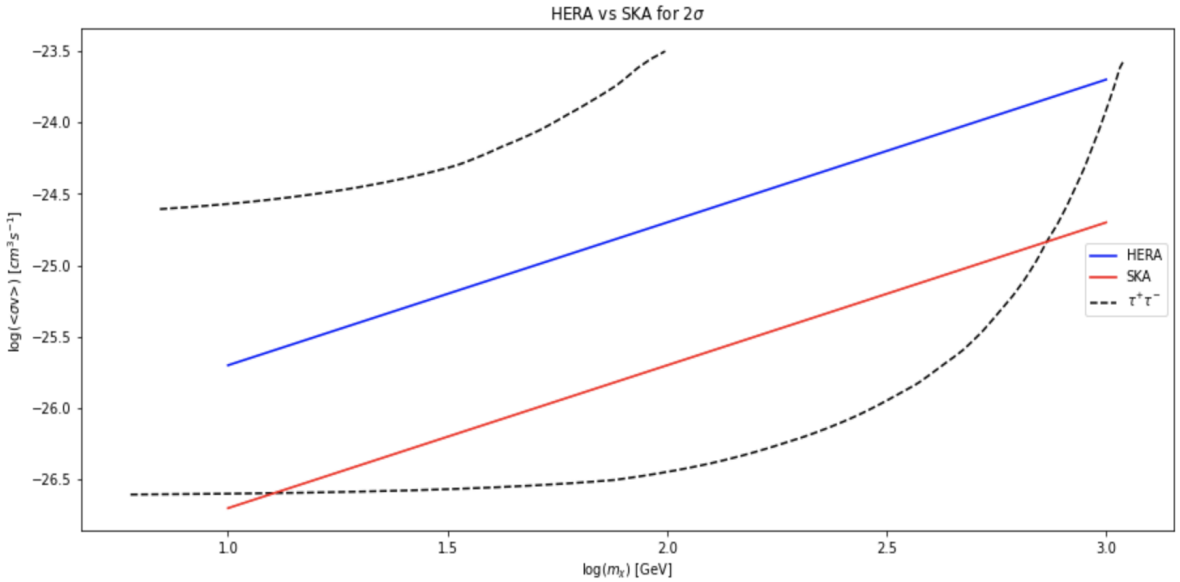


Figure 4.17: Sensitivity constraints on DM annihilation cross section for DM annihilating into $b\bar{b}$ final state for 2σ c.l with HERA and SKA after 1000 hours of integration time compared to the constraint on the DM annihilation cross section for $\tau^+\tau^-$ final states from Ref.[13]. The blue line represents the HERA constraints and the red line represents the SKA constraints. The black dotted lines represents the constraints on the annihilation cross section corresponding to the current optical depth measurements of $\Delta\tau = 0.012$.

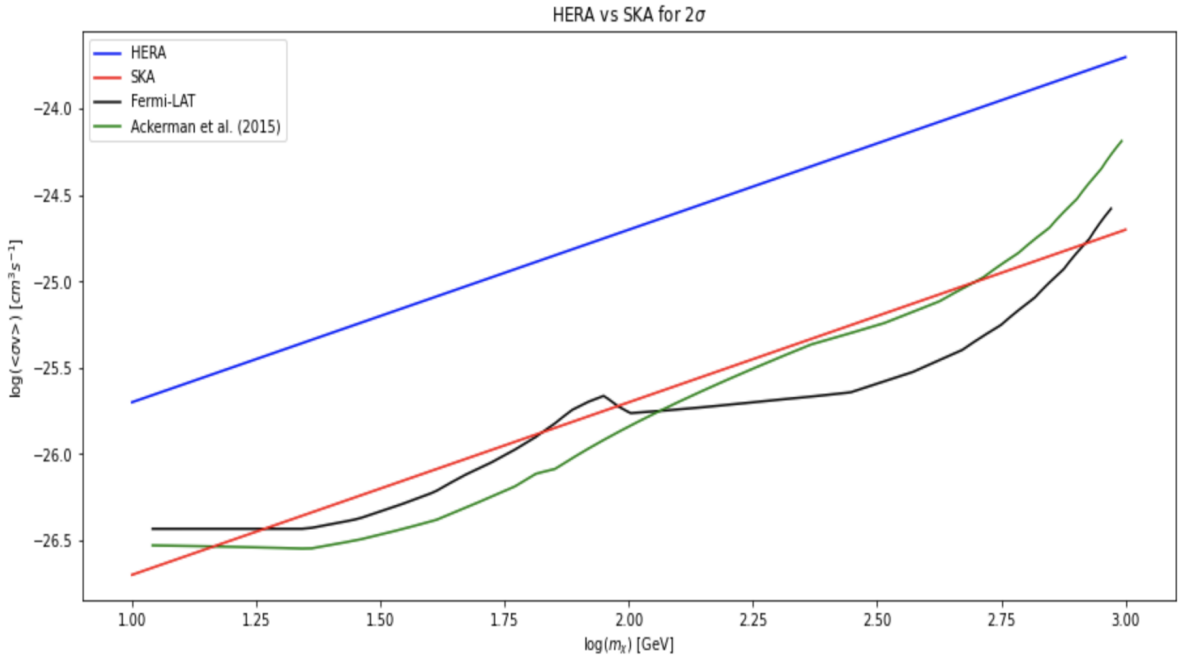


Figure 4.18: Sensitivity constraints on DM annihilation cross section for DM annihilating into $b\bar{b}$ final state with HERA and SKA for 1000 hours of integration time compared to the upper limits on the DM annihilation cross section from Ref.[14] (solid black line) and Ref.[15] (solid red line) for $b\bar{b}$ channel at 95% confidence interval.

4.3 Discussion

We have calculated predictions for the effects of DM annihilation on the evolution of the cosmological HI 21 cm signal. We noticed that our work produces quite interesting plots compared to other similar experiments, especially when it comes to the differences in the updated efficiency functions and data from DarkHistory. We were able to show that the updated functions as well as the matter temperature and ionization histories provide plots that are comparable to the baseline model from the global 21 cm spectrum. With the DarkHistory efficiency functions the trough at z $\sim$ 100 is less impacted by exotic energy injections from WIMPs, as can be seen in comparison to [9, 86]. Their heating effects were widely exaggerated mostly because their efficiency functions were based on assumptions that did not bear further scrutiny. Ref.[31] showed that their assumptions were flawed and proved that the deposition function can be orders of magnitude less efficient.

At higher redshifts (z $\geq$ 50), the IGM is dense enough that the spin temperature is coupled to the matter temperature because of collisions. The additional heat provided by DM annihilation during the collisional decoupling causes the slight deviation at z $\sim$ 100 as seen in the 21 cm brightness temperature plots. The impact of the DM annihilation becomes significantly enhanced when structure formation begins at z $\sim$ 40, which increases the local DM density. This is the the reason for the absorption signal observed at z $\sim$ 30. The effects of DM annihilation in our work is mild compared to previous work from [9, 112, 37] since a self-consistent model like ours takes into account the fact that the function from Equation 3.61 must be included in the integration of the transfer functions during the calculation as well as the ability of *DarkHistory* to solve simultaneously for the evolution of the temperature and ionization, this gives us a better approximation. It is worth noting that if DM annihilations contribute to the Lyman-α pumping and heating that occur during the release of the radiation from the first stars then the signal would show more gradual evolution during this absorption as pointed out by Ref.[87].

The global optical depth, τ, receives contributions from high energy objects in the Universe such as stars, quasars and potentially annihilating DM. We have plotted our constraints against that of [13] in order to get an idea of how well they perform against state-of-the-art calculations. However, given that the EoR is currently not properly constrained, it is hard to come up

with concrete conclusions to say whether our constraints are better since there are uncertainties about the use of different DM halo profiles, concentrations and other factors. It is also important to note that we use different treatment in the calculation of the energy deposition into the IGM by the products from the DM annihilation in halos. The authors use approximations from some earlier work with outdated reionization models from [128, 130] whereas we use the Puchwein model from [127]. Future measurements of the Universe's optical depth are expected to be more accurate coupled with the improvements of the 21 cm observations, this will allow us to properly constrain the DM mass and annihilation cross section.

This will be possible once HERA and the SKA is fully functional. As we have demonstrated in the HERA and SKA plots, the future 21 cm instruments hold a great potential to constrain properties of DM. We have noticed that measurements with 1000 hours of integration time for both instruments produce quite optimistic constraints against current telescopes including EDGES [131], PAPER [132] and the MWA [133] but more importantly our results are competitive with CMB constraints and Fermi-LAT. The authors of Ref. [134] have mentioned that for specific types of foreground avoidance approaches, several design optimizations allow HERA to achieve sensitivities comparable to the SKA and much higher than current instruments. This gives us confidence in our claim that we can use HERA for measurements of low mass DM particles, despite its modest collecting area. However, it remains clear that the SKA is the best observational probe to detect sub 10 mK signal in the global 21 cm spectrum, which would allow us to be able to better constrain the nature of DM especially WIMPs.

Chapter 5

Conclusion

In this work we presented an argument for the use of a comprehensive approach of investigating the effect of dark matter in the epoch of reinization using the redshifted 21 cm HI line. The nature of DM has been elusive for many years and this approach gives us another way to study the properties of DM. The EoR had been largely untested, so observations of the 21 cm line opens a new window into the properties of the Universe during the first billion years. In Chapter 2 we gave a brief overview of what DM is from a historical sense and went on to provide detailed explanations of the nature of DM as well as techniques of detecting it whether via direct and indirect detection methods. In Chapter 3 we laid out our groundwork by providing necessary description of the EoR and the 21 cm physics. This gave us an equation for the brightness temperature which is essential for this work. We also introduced *DarkHistory* as the main way of doing our analysis, through this we detailed exactly how our calculations work. We then showed that it might be possible in the near future to use interferometers as probes of the global 21 cm signal, if that is the case then the next generation of telescopes i.e HERA and the SKA will have the ability to make observations of the high redshift Universe via the global signal. This allows us to leverage the advantages of interferometers including their capabilities of avoiding noise and calibration issues that otherwise plagues single-element experiments. In Chapter 4 we outlined detailed observations and analysis of the global 21 cm brightness temperature from our two chosen DM annihilation channels.

We have also provided the analysis for the HERA and SKA observations for different masses and annihilation channels. We found that in general the noise levels for HERA was greater

than that of the SKA, this is due to that fact that the effective collecting area for HERA was a magnitude smaller. This allows for the SKA to have better constraints overall. It is also worth noting that HERA has limitations because it will not make observations beyond z $\sim$ 13 whilst the SKA can go farther than that. Constraints for DM annihilation cross section were provided for both HERA and SKA for 1σ and 2σ detections. The SKA being the most powerful instrument has the more competitive constraints over HERA, however we did note that HERA shows more promise for low mass models considering its low cost compared to the SKA. The ability to make observations of DM in EoR allows us to constrain even the global optical depth τ of the Universe. We have seen that with the data getting even better in the future, our constraints could better that of current experiments focusing on the optical depth. Furthermore, we note that our constraints are competitive against Fermi-LAT, which is the benchmark for indirect DM detection. This gives us a lot of confidence with our model. Therefore, we have demonstrated the power of future experiments in the radio regime of the spectrum to constrain DM in the EoR. As far we can tell, this is the first time an analysis like this has been performed to test out the capabilities of interferometers in constraining DM in the EoR. This particular approach of using the 21 cm spectrum is exciting because it has the capability to probe the high redshift Universe and make detailed maps of EoR and beyond.

5.1 Challenges and future work

We have shown that the EoR is a great probe of exotic energy injection, however this requires precise modelling of energy deposition. Previous work was rather exagerated and with the use of *DarkHistory* we were able to correct some of these. We did note however, that our models depicted sharp features as a result of the DarkHistory package and some of its functions and data. We will aim to correct this in future work. Further investigation is required in terms of understanding the use of interferometers, especially when it comes to the sensitivity as well as modeling the noise for the case of the measurements of the global signal. We have also tried to compare our results to sigle dish experiments but more work needs to be done, this includes finally adding all the Lyman-α sources to get a complete picture.

Bibliography

[1] Douglas Clowe, Maruša Bradač, Anthony H Gonzalez, Maxim Markevitch, Scott W Randall, Christine Jones, and Dennis Zaritsky. A direct empirical proof of the existence of dark matter. *The Astrophysical Journal Letters*, 648(2):L109, 2006.

[2] M Markevitch. Esa special publication 604, the x-ray universe 2005 ed a. *Wilson (Paris: ESA)*, 723, 2006.

[3] A Del Popolo, JAS Lima, Júlio C Fabris, and Davi C Rodrigues. A unified solution to the small scale problems of the λcdm model. *Journal of Cosmology and Astroparticle Physics*, 2014(04):021, 2014.

[4] Albert M Sirunyan, Armen Tumasyan, Wolfgang Adam, Federico Ambrogi, Ece Asilar, Thomas Bergauer, Johannes Brandstetter, Erica Brondolin, Marko Dragicevic, Janos Erö, et al. Search for supersymmetry in events with at least one photon, missing transverse momentum, and large transverse event activity in proton-proton collisions. *Journal of High Energy Physics*, 2017(12):142, 2017.

[5] Masanori Iye. National astronomical observatory of japan. *arXiv preprint arXiv:0908.0369*, 2009.

[6] Jonathan R Pritchard and Steven R Furlanetto. Descending from on high: Lyman-series cascades and spin-kinetic temperature coupling in the 21-cm line. *Monthly Notices of the Royal Astronomical Society*, 367(3):1057–1066, 2006.

[7] Jonathan R Pritchard and Abraham Loeb. 21 cm cosmology in the 21st century. *Reports on Progress in Physics*, 75(8):086901, 2012.

[8] Hongwan Liu, Tracy R Slatyer, and Jesús Zavala. Contributions to cosmic reionization from dark matter annihilation and decay. *Physical Review D*, 94(6):063507, 2016.

[9] Marcos Valdes, A Ferrara, M Mapelli, and E Ripamonti. Constraining dark matter through 21-cm observations. *Monthly Notices of the Royal Astronomical Society*, 377(1):245–252, 2007.

[10] Hongwan Liu, Gregory W Ridgway, and Tracy R Slatyer. Darkhistory: A code package for calculating modified cosmic ionization and thermal histories with dark matter and other exotic energy injections. *arXiv preprint arXiv:1904.09296*, 2019.

[11] Jonathan R Pritchard and Abraham Loeb. Evolution of the 21 cm signal throughout cosmic history. *Physical review D*, 78(10):103511, 2008.

[12] Raul A Monsalve, Alan EE Rogers, Judd D Bowman, and Thomas J Mozdzen. Results from edges high-band. i. constraints on phenomenological models for the global 21 cm signal. *The Astrophysical Journal*, 847(1):64, 2017.

[13] Alexander A Kaurov, Dan Hooper, and Nickolay Y Gnedin. The effects of dark matter annihilation on cosmic reionization. *The Astrophysical Journal*, 833(2):162, 2016.

[14] Andrea Albert, Brandon Anderson, Keith Bechtol, Alex Drlica-Wagner, Manuel Meyer, Miguel Sánchez-Conde, L Strigari, M Wood, TMC Abbott, Filipe B Abdalla, et al. Searching for dark matter annihilation in recently discovered milky way satellites with fermi-lat. *The Astrophysical Journal*, 834(2):110, 2017.

[15] Markus Ackermann, Marco Ajello, WB Atwood, Luca Baldini, Guido Barbiellini, D Bastieri, K Bechtol, R Bellazzini, RD Blandford, ED Bloom, et al. Constraints on the galactic halo dark matter from fermi-lat diffuse measurements. *The Astrophysical Journal*, 761(2):91, 2012.

[16] CS Frenk, N Katz, and CG Lacey. Apj 633, 791 zwicky f., 1933. *Helvetica Physica Acta*, 6(110):1961–1968, 2005.

[17] Peter AR Ade, N Aghanim, M Arnaud, Mark Ashdown, J Aumont, C Baccigalupi, AJ Banday, RB Barreiro, JG Bartlett, N Bartolo, et al. Planck 2015 results-xiii. cosmological parameters. *Astronomy & Astrophysics*, 594:A13, 2016.

[18] GR Blumenthal, SM Faber, JR Primack, and MJ Rees. Erratum: Formation of galaxies and large-scale structure with cold dark matter. *Nature*, 313(5997):72–72, 1985.

[19] Douglas Clowe, Anthony Gonzalez, and Maxim Markevitch. Weak-lensing mass reconstruction of the interacting cluster 1e 0657–558: Direct evidence for the existence of dark matter. *The Astrophysical Journal*, 604(2):596, 2004.

[20] David N Schramm and Michael S Turner. Big-bang nucleosynthesis enters the precision era. *Reviews of Modern Physics*, 70(1):303, 1998.

[21] Jaan Einasto, Ants Kaasik, and Enn Saar. Dynamic evidence on massive coronas of galaxies. *Nature*, 250(5464):309–310, 1974.

[22] Mordehai Milgrom. A modification of the newtonian dynamics as a possible alternative to the hidden mass hypothesis. *The Astrophysical Journal*, 270:365–370, 1983.

[23] Gerard Jungman, Marc Kamionkowski, and Kim Griest. Supersymmetric dark matter. *Physics Reports*, 267(5-6):195–373, 1996.

[24] Gianfranco Bertone and Dan Hooper. History of dark matter. *Reviews of Modern Physics*, 90(4):045002, 2018.

[25] IV Moskalenko and AW Strong. Production and propagation of cosmic-ray positrons and electrons. *The Astrophysical Journal*, 493(2):694, 1998.

[26] Kevork N Abazajian. Sterile neutrino/dark fermion dark matter: Searches in the x-ray sky, the nuclear physics laboratory and in galaxy formation. In *Illuminating Dark Matter*, pages 1–8. Springer, 2019.

[27] JW Moffat and VT Toth. Modified gravity: Cosmology without dark matter or einstein's cosmological constant. *arXiv preprint arXiv:0710.0364*, 2007.

[28] Leanne D Duffy and Karl Van Bibber. Axions as dark matter particles. *New Journal of Physics*, 11(10):105008, 2009.

[29] Geraldine Servant and Tim MP Tait. Is the lightest kaluza–klein particle a viable dark matter candidate? *Nuclear Physics B*, 650(1-2):391–419, 2003.

[30] Mitsuru Kakizaki, Shigeki Matsumoto, Yoshio Sato, and Masato Senami. Significant effects of second kaluza-klein particles on dark matter physics. *Physical Review D*, 71(12):123522, 2005.

[31] Tracy R Slatyer. Indirect dark matter signatures in the cosmic dark ages. i. generalizing the bound on s-wave dark matter annihilation from planck results. *Physical Review D*, 93(2):023527, 2016.

[32] M Aguilar, Giovanni Alberti, B Alpat, A Alvino, G Ambrosi, K Andeen, H Anderhub, L Arruda, P Azzarello, A Bachlechner, et al. First result from the alpha magnetic spectrometer on the international space station: precision measurement of the positron fraction in primary cosmic rays of 0.5–350 gev. *Physical Review Letters*, 110(14):141102, 2013.

[33] Oscar Adriani, GC Barbarino, GA Bazilevskaya, R Bellotti, Mirko Boezio, EA Bogomolov, L Bonechi, M Bongi, Valter Bonvicini, S Bottai, et al. An anomalous positron abundance in cosmic rays with energies 1.5–100 gev. *Nature*, 458(7238):607–609, 2009.

[34] Dan Hooper and Tim Linden. Origin of the gamma rays from the galactic center. *Physical Review D*, 84(12):123005, 2011.

[35] Chris Gordon and Oscar Macias. Dark matter and pulsar model constraints from galactic center fermi-lat gamma-ray observations. *Physical Review D*, 88(8):083521, 2013.

[36] Kevork N Abazajian and Manoj Kaplinghat. Detection of a gamma-ray source in the galactic center consistent with extended emission from dark matter annihilation and concentrated astrophysical emission. *Physical Review D*, 86(8):083511, 2012.

[37] Steven R Furlanetto, S Peng Oh, and Frank H Briggs. Cosmology at low frequencies: The 21 cm transition and the high-redshift universe. *Physics reports*, 433(4-6):181–301, 2006.

[38] Abraham Loeb and Steven R Furlanetto. *The first galaxies in the universe*, volume 21. Princeton University Press, 2013.

[39] Saleem Zaroubi, Rajat M Thomas, Naoshi Sugiyama, and Joseph Silk. Heating of the intergalactic medium by primordial miniquasars. *Monthly Notices of the Royal Astronomical Society*, 375(4):1269–1279, 2007.

[40] Vera C Rubin and W Kent Ford Jr. Rotation of the andromeda nebula from a spectroscopic survey of emission regions. *The Astrophysical Journal*, 159:379, 1970.

[41] Albert Einstein. Die grundlage der allgemeinen relativitätstheorie. In *Das Relativitätsprinzip*, pages 81–124. Springer, 1923.

[42] Richard Massey, Thomas Kitching, and Johan Richard. The dark matter of gravitational lensing. *Reports on Progress in Physics*, 73(8):086901, 2010.

[43] Robert M Wald. General relativity(book). *Chicago, University of Chicago Press, 1984, 504 p*, 1984.

[44] E Komatsu et al. The astrophysical journal supplement. *Volume*, 180:330–376.

[45] Katherine Freese. Status of dark matter in the universe. *International Journal of Modern Physics D*, 26(06):1730012, 2017.

[46] John Gribbin. Dark-matter and the universe. *Science, Inside Science*, 19, 1994.

[47] Subir Sarkar. Big bang nucleosynthesis and physics beyond the standard model. *Reports on Progress in Physics*, 59(12):1493, 1996.

[48] Volker Springel, Carlos S Frenk, and Simon DM White. The large-scale structure of the universe. *Nature*, 440(7088):1137–1144, 2006.

[49] Shaun Cole, Will J Percival, John A Peacock, Peder Norberg, Carlton M Baugh, Carlos S Frenk, Ivan Baldry, Joss Bland-Hawthorn, Terry Bridges, Russell Cannon, et al. The 2df galaxy redshift survey: power-spectrum analysis of the final data set and cosmological implications. *Monthly Notices of the Royal Astronomical Society*, 362(2):505–534, 2005.

[50] Max Tegmark, Michael A Strauss, Michael R Blanton, Kevork Abazajian, Scott Dodelson, Havard Sandvik, Xiaomin Wang, David H Weinberg, Idit Zehavi, Neta A Bahcall, et al. Cosmological parameters from sdss and wmap. *Physical review D*, 69(10):103501, 2004.

[51] Marek Kowalski, David Rubin, Greg Aldering, RJ Agostinho, A Amadon, R Amanullah, C Balland, K Barbary, G Blanc, PJ Challis, et al. Improved cosmological constraints from new, old, and combined supernova data sets. *The Astrophysical Journal*, 686(2):749, 2008.

[52] Barbara Ryden. *Introduction to cosmology*. Cambridge University Press, 2017.

[53] Charles Alcock, RA Allsman, David R Alves, TS Axelrod, Andrew C Becker, DP Bennett, Kem H Cook, N Dalal, Andrew John Drake, KC Freeman, et al. The macho project: microlensing results from 5.7 years of large magellanic cloud observations. *The Astrophysical Journal*, 542(1):281, 2000.

[54] Markus Kuster, Georg Raffelt, and Berta Beltrán. *Axions: Theory, cosmology, and experimental searches*, volume 741. Springer, 2007.

[55] John Preskill, Mark B Wise, and Frank Wilczek. Cosmology of the invisible axion. *Physics Letters B*, 120(1-3):127–132, 1983.

[56] Lars Bergström. Non-baryonic dark matter: observational evidence and detection methods. *Reports on Progress in Physics*, 63(5):793, 2000.

[57] Julio F Navarro. The structure of cold dark matter halos. In *Symposium-international astronomical union*, volume 171, pages 255–258. Cambridge University Press, 1996.

[58] Andrea V Macciò, Aaron A Dutton, and Frank C Van Den Bosch. Concentration, spin and shape of dark matter haloes as a function of the cosmological model: Wmap 1, wmap 3 and wmap 5 results. *Monthly Notices of the Royal Astronomical Society*, 391(4):1940–1954, 2008.

[59] Mark Vogelsberger and Jesus Zavala. Direct detection of self-interacting dark matter. *Monthly Notices of the Royal Astronomical Society*, 430(3):1722–1735, 2013.

[60] Louis E Strigari, James S Bullock, Manoj Kaplinghat, Joshua D Simon, Marla Geha, Beth Willman, and Matthew G Walker. A common mass scale for satellite galaxies of the milky way. *Nature*, 454(7208):1096–1097, 2008.

[61] Jaan Einasto, Enn Saar, Ants Kaasik, and Arthur D Chernin. Missing mass around galaxies: morphological evidence. *Nature*, 252(5479):111–113, 1974.

[62] Andreas Burkert. The structure of dark matter halos in dwarf galaxies. *The Astrophysical Journal Letters*, 447(1):L25, 1995.

[63] Matthew G Walker and Jorge Penarrubia. A method for measuring (slopes of) the mass profiles of dwarf spheroidal galaxies. *The Astrophysical Journal*, 742(1):20, 2011.

[64] NC Amorisco, A Agnello, and NW Evans. The core size of the fornax dwarf spheroidal. *Monthly Notices of the Royal Astronomical Society: Letters*, 429(1):L89–L93, 2013.

[65] Mark W Goodman and Edward Witten. Detectability of certain dark-matter candidates. *Physical Review D*, 31(12):3059, 1985.

[66] JD Lewin and PF Smith. Review of mathematics, numerical factors, and corrections for dark matter experiments based on elastic nuclear recoil. Technical report, SCAN-9603159, 1996.

[67] R Bernabei, P Belli, F Cappella, R Cerulli, CJ Dai, A dAngelo, HL He, A Incicchitti, HH Kuang, JM Ma, et al. First results from dama/libra and the combined results with dama/nai. *The European Physical Journal C*, 56(3):333, 2008.

[68] Craig E Aalseth, Phillip Spencer Barbeau, J Colaresi, JI Collar, J Diaz Leon, James E Fast, NE Fields, Todd W Hossbach, Andrea Knecht, Marek S Kos, et al. Cogent: A search for low-mass dark matter using p-type point contact germanium detectors. *Physical Review D*, 88(1):012002, 2013.

[69] Laura Baudis, Adam Brown, Chiara Capelli, Michelle Galloway, Shingo Kazama, A Kish, Shayne Reichard, J Wulf, XENON Collaboration, et al. Dark matter search results from a one ton-year exposure of xenon1t. *Physical Review Letters*, 121(11):111302, 2018.

[70] M Aaboud et al. Search for squarks and gluinos in events with an isolated lepton, jets, and missing transverse momentum at. *PHYSICAL REVIEW D Phys Rev D*, 96:112010, 2017.

[71] Kamakshya Prasad Modak, Debasish Majumdar, and Subhendu Rakshit. A possible explanation of low energy γ-ray excess from galactic centre and fermi bubble by a dark matter model with two real scalars. *Journal of Cosmology and Astroparticle Physics*, 2015(03):011, 2015.

[72] Jan Conrad. Indirect detection of wimp dark matter: a compact review. *arXiv preprint arXiv:1411.1925*, 2014.

[73] Torsten Bringmann, Michele Doro, and Mattia Fornasa. Dark matter signals from draco and willman 1: Prospects for magic ii and cta. *Journal of Cosmology and Astroparticle Physics*, 2009(01):016, 2009.

[74] Meng Su, Tracy R Slatyer, and Douglas P Finkbeiner. Giant gamma-ray bubbles from fermi-lat: active galactic nucleus activity or bipolar galactic wind? *The Astrophysical Journal*, 724(2):1044, 2010.

[75] Jurgen Knödlseder, V Lonjou, Pierre Jean, M Allain, P Mandrou, J-P Roques, GK Skinner, G Vedrenne, Peter von Ballmoos, G Weidenspointner, et al. Early spi/integral constraints on the morphology of the 511 kev line emission in the 4th galactic quadrant. *Astronomy & Astrophysics*, 411(1):L457–L460, 2003.

[76] Max Ludwig Ahnen, S Ansoldi, LA Antonelli, P Antoranz, A Babic, B Banerjee, P Bangale, U Barres de Almeida, JA Barrio, J Becerra Gonzalez, et al. Limits to dark matter annihilation cross-section from a combined analysis of magic and fermi-lat observations of dwarf satellite galaxies. *arXiv preprint arXiv:1601.06590*, 2016.

[77] C Boehm, TA Ensslin, and J Silk. Can annihilating dark matter be lighter than a few gevs? *Journal of Physics G: Nuclear and Particle Physics*, 30(3):279, 2004.

[78] C Boehm and Pierre Fayet. Scalar dark matter candidates. *Nuclear Physics B*, 683(1-2):219–263, 2004.

[79] Junji Hisano, Shigeki Matsumoto, Mihoko M Nojiri, and Osamu Saito. Nonperturbative effect on dark matter annihilation and gamma ray signature from the galactic center. *Physical Review D*, 71(6):063528, 2005.

[80] Nima Arkani-Hamed, Douglas P Finkbeiner, Tracy R Slatyer, and Neal Weiner. A theory of dark matter. *Physical Review D*, 79(1):015014, 2009.

[81] Maxim Pospelov and Adam Ritz. Astrophysical signatures of secluded dark matter. *Physics Letters B*, 671(3):391–397, 2009.

[82] R Cowsik, B Burch, and T Madziwa-Nussinov. The origin of the spectral intensities of cosmic-ray positrons. *The Astrophysical Journal*, 786(2):124, 2014.

[83] R Cowsik and B Burch. Positron fraction in cosmic rays and models of cosmic-ray propagation. *Physical Review D*, 82(2):023009, 2010.

[84] VL Ginzburg. Gamma radiation of magellanic clouds and metagalactic origin of cosmic rays. *Nature Physical Science*, 239(88):8–9, 1972.

[85] Javier Rico. Gamma ray dark matter searches in milky way satellites a comparative review of data analysis methods and current results. *Galaxies*, 8(1):25, 2020.

[86] Marcos Valdés, Carmelo Evoli, Andrei Mesinger, Andrea Ferrara, and Naoki Yoshida. The nature of dark matter from the global high-redshift h i 21 cm signal. *Monthly Notices of the Royal Astronomical Society*, 429(2):1705–1716, 2013.

[87] Carmelo Evoli, Andrei Mesinger, and Andrea Ferrara. Unveiling the nature of dark matter with high redshift 21 cm line experiments. *Journal of Cosmology and Astroparticle Physics*, 2014(11):024, 2014.

[88] L Lopez-Honorez, O Mena, Á Moliné, S Palomares-Ruiz, and AC Vincent. The 21 cm signal and the interplay between dark matter annihilations and astrophysical processes j. cosmol. *Astropart. Phys*, 8(004):1603–06795, 2016.

[89] Xiaohui Fan, Michael A Strauss, Robert H Becker, Richard L White, James E Gunn, Gillian R Knapp, Gordon T Richards, Donald P Schneider, J Brinkmann, and Masataka Fukugita. Constraining the evolution of the ionizing background and the epoch of reionization with z 6 quasars. ii. a sample of 19 quasars. *The Astronomical Journal*, 132(1):117, 2006.

[90] Ian D McGreer, Andrei Mesinger, and Valentina D'Odorico. Model-independent evidence in favour of an end to reionization by z6. *Monthly Notices of the Royal Astronomical Society*, 447(1):499–505, 2015.

[91] Steven Furlanetto, Chris L Carilli, Jordan Mirocha, James Aguirre, Yacine Ali-Haimoud, Marcelo Alvarez, Adam Beardsley, George Becker, Judd D Bowman, Patrick Breysse, et al. Astro2020 science white paper: Insights into the epoch of reionization with the highly-redshifted 21-cm line. *arXiv preprint arXiv:1903.06204*, 2019.

[92] P Schellart, A Nelles, S Buitink, A Corstanje, JE Enriquez, H Falcke, W Frieswijk, JR Hörandel, A Horneffer, CW James, et al. Detecting cosmic rays with the lofar radio telescope. *Astronomy & Astrophysics*, 560:A98, 2013.

[93] Randall Wayth, Timothy Colegate, Marcin Sokolowski, Adrian Sutinjo, and Daniel Ung. Advanced, efficient primary beam modeling for the murchison widefield array radio telescope. In *2016 International Conference on Electromagnetics in Advanced Applications (ICEAA)*, pages 431–434. IEEE, 2016.

[94] Donald C Backer, James Aguirre, Judd D Bowman, Richard Bradley, Frank Briggs, Chris L Carilli, Steven R Furlanetto, Lincoln J Greenhill, Jacqueline N Hewitt, Colin

Lonsdale10, et al. Hera.hydrogen epoch of reionization arrays. *White paper submitted to US ASTRO2010 Decadal Review. Reionization. org*, 2009.

[95] David J Griffiths and Darrell F Schroeter. *Introduction to quantum mechanics*. Cambridge University Press, 2018.

[96] George B Rybicki and Alan P Lightman. *Radiative processes in astrophysics*. John Wiley & Sons, 2008.

[97] B Zygelman. Hyperfine level-changing collisions of hydrogen atoms and tomography of the dark age universe. *The Astrophysical Journal*, 622(2):1356, 2005.

[98] Steven R Furlanetto. The global 21-centimeter background from high redshifts. *Monthly Notices of the Royal Astronomical Society*, 371(2):867–878, 2006.

[99] Steven R Furlanetto and Michael R Furlanetto. Spin exchange rates in proton–hydrogen collisions. *Monthly Notices of the Royal Astronomical Society*, 379(1):130–134, 2007.

[100] AC Allison and A Dalgarno. Spin change in collisions of hydrogen atoms. *The Astrophysical Journal*, 158:423, 1969.

[101] A Meiksin. Detecting the epoch of first light in 21-cm radiation. In *Perspectives on Radio Astronomy: Science with Large Antenna Arrays*, page 37, 2000.

[102] Christopher M Hirata. Wouthuysen-field coupling strength and application to high-redshift 21-cm radiation. *Monthly Notices of the Royal Astronomical Society*, 367(1):259–274, 2006.

[103] Smadar Naoz and Rennan Barkana. Growth of linear perturbations before the era of the first galaxies. *Monthly Notices of the Royal Astronomical Society*, 362(3):1047–1053, 2005.

[104] Sara Seager, Dimitar D Sasselov, and Douglas Scott. A new calculation of the recombination epoch. *The Astrophysical Journal Letters*, 523(1):L1, 1999.

[105] Steven R Furlanetto and Jonathan R Pritchard. The scattering of lyman-series photons in the intergalactic medium. *Monthly Notices of the Royal Astronomical Society*, 372(3):1093–1103, 2006.

[106] Aparna Venkatesan, Mark L Giroux, and J Michael Shull. Heating and ionization of the intergalactic medium by an early x-ray background. *The Astrophysical Journal*, 563(1):1, 2001.

[107] S Peng Oh. Reionization by hard photons. i. x-rays from the first star clusters. *The Astrophysical Journal*, 553(2):499, 2001.

[108] X Chen. J. miralda-escud e. *Astrophys. J*, 602:1, 2004.

[109] J Michael Shull and Michael E van Steenberg. X-ray secondary heating and ionization in quasar emission-line clouds. *The Astrophysical Journal*, 298:268–274, 1985.

[110] Sara Seager, Dimitar D Sasselov, and Douglas Scott. How exactly did the universe become neutral? *The Astrophysical Journal Supplement Series*, 128(2):407, 2000.

[111] Jens Chluba, Daniela Paoletti, Fabio Finelli, and Jose-Alberto Rubino-Martin. Effect of primordial magnetic fields on the ionization history. *Monthly Notices of the Royal Astronomical Society*, 451(2):2244–2250, 2015.

[112] Marcos Valdes, Carmelo Evoli, and Andrea Ferrara. Particle energy cascade in the intergalactic medium. *Monthly Notices of the Royal Astronomical Society*, 404(3):1569–1582, 2010.

[113] Silvia Galli, Tracy R Slatyer, Marcos Valdes, and Fabio Iocco. Systematic uncertainties in constraining dark matter annihilation from the cosmic microwave background. *Physical Review D*, 88(6):063502, 2013.

[114] Judd D Bowman, Alan EE Rogers, Raul A Monsalve, Thomas J Mozdzen, and Nivedita Mahesh. An absorption profile centred at 78 megahertz in the sky-averaged spectrum. *Nature*, 555(7694):67–70, 2018.

[115] Morgan E Presley, Adrian Liu, and Aaron R Parsons. Measuring the cosmological 21 cm monopole with an interferometer. *The Astrophysical Journal*, 809(1):18, 2015.

[116] Tejaswi Venumadhav, Tzu-Ching Chang, Olivier Doré, and Christopher M Hirata. A practical theorem on using interferometry to measure the global 21 cm signal. *The Astrophysical Journal*, 826(2):116, 2016.

[117] Anastasia Fialkov, Rennan Barkana, and Matt Jarvis. Extracting the global signal from 21-cm fluctuations: the multitracer approach. *Monthly Notices of the Royal Astronomical Society*, 491(3):3108–3119, 2020.

[118] HK Vedantham, LVE Koopmans, AG De Bruyn, SJ Wijnholds, M Brentjens, FB Abdalla, KMB Asad, GIANNI Bernardi, S Bus, E Chapman, et al. Lunar occultation of the diffuse

radio sky: Lofar measurements between 35 and 80 mhz. *Monthly Notices of the Royal Astronomical Society*, 450(3):2291–2305, 2015.

[119] Rennan Barkana. Possible interaction between baryons and dark-matter particles revealed by the first stars. *Nature*, 555(7694):71–74, 2018.

[120] Ely D Kovetz, Vivian Poulin, Vera Gluscevic, Kimberly K Boddy, Rennan Barkana, and Marc Kamionkowski. Tighter limits on dark matter explanations of the anomalous edges 21 cm signal. *Physical Review D*, 98(10):103529, 2018.

[121] A Ewall-Wice, T-C Chang, J Lazio, O Doré, M Seiffert, and RA Monsalve. Modeling the radio background from the first black holes at cosmic dawn: implications for the 21 cm absorption amplitude. *The Astrophysical Journal*, 868(1):63, 2018.

[122] Saurabh Singh, Ravi Subrahmanyan, N Udaya Shankar, and A Raghunathan. On the detection of global 21-cm signal from reionization using interferometers. *The Astrophysical Journal*, 815(2):88, 2015.

[123] Gianni Bernardi. Measurements of the global 21-cm signal from the cosmic dawn. *Proceedings of the International Astronomical Union*, 12(S333):98–101, 2017.

[124] Gregory Paciga, Joshua G Albert, Kevin Bandura, Tzu-Ching Chang, Yashwant Gupta, Christopher Hirata, Julia Odegova, Ue-Li Pen, Jeffrey B Peterson, Jayanta Roy, et al. A simulation-calibrated limit on the h i power spectrum from the gmrt epoch of reionization experiment. *Monthly Notices of the Royal Astronomical Society*, 433(1):639–647, 2013.

[125] Nivedita Mahesh, Ravi Subrahmanyan, N Udaya Shankar, and Agaram Raghunathan. A resistive wideband space beam splitter. *arXiv preprint arXiv:1406.2585*, 2014.

[126] B McKinley, GIANNI Bernardi, CM Trott, JLB Line, RB Wayth, AR Offringa, B Pindor, CH Jordan, Marcin Sokolowski, SJ Tingay, et al. Measuring the global 21-cm signal with the mwa-i: improved measurements of the galactic synchrotron background using lunar occultation. *Monthly Notices of the Royal Astronomical Society*, 481(4):5034–5045, 2018.

[127] Ewald Puchwein, Francesco Haardt, Martin G Haehnelt, and Piero Madau. Consistent modelling of the meta-galactic uv background and the thermal/ionization history of the intergalactic medium. *Monthly Notices of the Royal Astronomical Society*, 485(1):47–68, 2019.

[128] Alexander A Kaurov and Nickolay Y Gnedin. Cosmic reionization on computers. iii. the clumping factor. *The Astrophysical Journal*, 810(2):154, 2015.

[129] Nickolay Y Gnedin and Alexander A Kaurov. Cosmic reionization on computers. ii. reionization history and its back-reaction on early galaxies. *The Astrophysical Journal*, 793(1):30, 2014.

[130] Leonid Chuzhoy. Impact of dark matter annihilation on the high-redshift intergalactic medium. *The Astrophysical Journal Letters*, 679(2):L65, 2008.

[131] Daniel T Cumberbatch, Massimiliano Lattanzi, and Joseph Silk. Signatures of clumpy dark matter in the global 21 cm background signal. *Physical Review D*, 82(10):103508, 2010.

[132] Aaron R Parsons, Donald C Backer, Griffin S Foster, Melvyn CH Wright, Richard F Bradley, Nicole E Gugliucci, Chaitali R Parashare, Erin E Benoit, James E Aguirre, Daniel C Jacobs, et al. The precision array for probing the epoch of re-ionization: Eight station results. *The Astronomical Journal*, 139(4):1468, 2010.

[133] Steven John Tingay, Robert Goeke, Judd D Bowman, David Emrich, Stephen M Ord, Daniel A Mitchell, Miguel F Morales, Tom Booler, Brian Crosse, Randall B Wayth, et al. The murchison widefield array: The square kilometre array precursor at low radio frequencies. *Publications of the Astronomical Society of Australia*, 30, 2013.

[134] David R DeBoer, Aaron R Parsons, James E Aguirre, Paul Alexander, Zaki S Ali, Adam P Beardsley, Gianni Bernardi, Judd D Bowman, Richard F Bradley, Chris L Carilli, et al. Hydrogen epoch of reionization array (hera). *Publications of the Astronomical Society of the Pacific*, 129(974):045001, 2017.